

Nonlinear synchrony dynamics of neuronal bursters.

Submitted by

Abul Kalam al Azad

to the University of Exeter as a thesis for the degree of Doctor of Philosophy in Applied Mathematics, February 2010.

This thesis is available for Library use on the understanding that it is copyright material and that no quotation from the thesis may be published without proper acknowledgement.

I certify that all material in this thesis which is not my own work has been identified and that no material is included for which a degree has previously been conferred upon me.

.....
Abul Kalam al Azad

Abstract

We study the appearance of a novel phenomenon for coupled identical bursters: synchronized bursts where there are changes of spike synchrony within each burst. The examples we study are for normal form elliptic bursters where there is a periodic slow passage through a Bautin (codimension two degenerate Andronov-Hopf) bifurcation. This burster has a subcritical Andronov-Hopf bifurcation at the onset of repetitive spiking while the end of burst occurs via a fold limit cycle bifurcation. We study synchronization behavior of two Bautin-type elliptic bursters for a linear direct coupling scheme as well as demonstrating its presence in an approximation of gap-junction and synaptic coupling. We also find similar behaviour in system consisted of three and four Bautin-type elliptic bursters. We note that higher order terms in the normal form that do not affect the behavior of a single burster can be responsible for changes in synchrony pattern; more precisely, we find within-burst synchrony changes associated with a turning point in the spontaneous spiking frequency (frequency transition). We also find multiple synchrony changes in similar system by incorporating multiple frequency transitions. To explain the phenomenon we considered a burst-synchronized constrained model and a bifurcation analysis of the this reduced model shows the existence of the observed within-burst synchrony states.

Within-burst synchrony change is also found in the system of mutually delay-coupled two Bautin-type elliptic bursters with a constant delay. The similar phenomenon is shown to exist in the mutually-coupled conductance-based Morris-Lecar neuronal system with an additional slow variable generating elliptic bursting.

We also find within-burst synchrony change in linearly coupled FitzHugh-Rinzel

elliptic bursting system where the synchrony change occurs via a period doubling bifurcation. A bifurcation analysis of a burst-synchronized constrained system identifies the periodic doubling bifurcation in this case.

We show emergence of spontaneous burst synchrony cluster in the system of three Hindmarsh-Rose square-wave bursters with nonlinear coupling. The system is found to change between the available cluster states depending on the stimulus. Lyapunov exponents of the burst synchrony states are computed from the corresponding variational system to probe the stability of the states. Numerical simulation also shows existence of burst synchrony cluster in the larger network of such system.

Acknowledgements

I would like to thank all of those who made my PhD achievable and enjoyable. First of all, I would like to thank my supervisor Peter Ashwin for his continued support and guidance throughout my PhD. His expertise, sincerity and encouragement over the last three years have profusely benefited both my intellect and character. I would also like to thank my second supervisor Stuart Towley who extended his sincere support whenever I sought his help.

I am grateful to my mother and my family for their love, affection and understanding during my degree and especially during the period of writing up; their unconditional support helped me a lot to focus on my writing up.

I truly appreciate the support of my colleagues at the Mathematics Research Institute; special thanks to Gabor Orosz, Erzgraber Hartmut, Sebastian Wieczorek, Matthew Turner and Renato Vitolo for their help and good gestures on innumerable occasions. I would like to say thanks to my friends for encouragement, company and countless good times I had had with them, special thanks to Carlos Martinez and Jonathan Moore for patiently proof reading my manuscript. I would also like to acknowledge the help and support of Professor Tassilo Keupper and Svitlana Popovych of Mathematical Institute of University of Cologne for their hospitality and very fruitful discussions on my research during my stay in Cologne, Germany. Finally, I would like to thank University of Exeter for awarding me Exeter Research Scholarships to pursue the PhD degree.

Contents

| | |
|---|-----------|
| Acknowledgements | 3 |
| Contents | 4 |
| List of Figures | 9 |
| List of Tables | 21 |
| 1 Introduction to neuronal bursters | 22 |
| 1.1 Ionic mechanism of bursting | 23 |
| 1.2 Mathematical mechanism | 25 |
| 1.2.1 The Plant model | 26 |
| 1.2.2 The Chay-Keizer model | 28 |
| 1.3 Mathematical properties and analysis of bursting models | 30 |
| 1.3.1 Hysteresis loop | 31 |
| 1.3.2 Geometric singular perturbation method | 32 |
| 1.4 Rinzel's classification of bursting oscillations | 37 |
| 1.4.1 Square wave bursting | 38 |
| 1.4.2 Parabolic bursting | 39 |
| 1.4.3 Elliptic bursting | 40 |
| 1.5 Outline of thesis | 42 |
| 2 Burst dynamics | 44 |
| 2.1 Topological classification | 44 |
| 2.2 Minimal bursting models | 51 |

| | | |
|----------|---|------------|
| 2.2.1 | Canonical models for bursters | 52 |
| 2.2.2 | Normal form | 55 |
| 2.2.3 | Topological normal forms for bifurcations | 56 |
| 2.3 | The Bautin bifurcation | 57 |
| 2.3.1 | Bautin elliptic burster | 58 |
| 2.4 | Delayed bursting: slow passage effect | 67 |
| 3 | Coupled neuronal bursters | 69 |
| 3.1 | The leech heart interneuron model | 69 |
| 3.2 | Synchronization of coupled bursters | 74 |
| 3.2.1 | Burst synchronization | 74 |
| 3.3 | Spike synchronization | 77 |
| 3.4 | Coupled Bautin bursters | 79 |
| 3.5 | The model for coupled Bautin bursters | 80 |
| 3.5.1 | Burst and spike synchronization for two coupled bursters . . | 84 |
| 4 | Analysis of within-burst synchrony changes | 88 |
| 4.1 | A burst-synchronized constrained model | 88 |
| 4.1.1 | Two coupled bursters in polar coordinates | 89 |
| 4.1.2 | Stability analysis of the burst constrained system | 90 |
| 4.1.3 | Synchrony bifurcations of the fast subsystem | 94 |
| 4.2 | Understanding within-burst synchrony changes from the constrained system | 100 |
| 4.2.1 | Effects of noise on within-burst synchrony changes | 100 |
| 4.2.2 | Examples with biologically-motivated coupling | 102 |
| 5 | Within-burst cascade of synchrony changes | 105 |
| 5.1 | The model | 105 |
| 5.1.1 | Single compartment elliptic burster | 106 |
| 5.1.2 | Model for coupled elliptic bursters | 106 |
| 5.2 | Cascades with two synchrony changes | 107 |
| 5.2.1 | Simulation of two within-burst synchrony changes | 107 |

| | | |
|----------|--|------------|
| 5.2.2 | The burst-synchronized constrained model | 110 |
| 5.2.3 | Synchrony bifurcation of the fast subsystem | 111 |
| 5.2.4 | Stability analysis of the burst-synchronized constrained system | 114 |
| 5.2.5 | Case $\kappa_1 = 0$ | 114 |
| 5.2.6 | Case $\kappa_1 \neq 0$ | 116 |
| 5.3 | Cascades with multiple synchrony changes | 116 |
| 5.3.1 | Two coupled bursters | 117 |
| 5.3.2 | Cascades with varying number of synchrony changes | 119 |
| 5.3.3 | Bifurcation of the fast subsystem with cascades | 120 |
| 5.4 | Further cascades of synchrony changes | 121 |
| 5.5 | Synchrony changes with more general Ω | 123 |
| 6 | Within-burst synchrony changes in higher dimensions | 126 |
| 6.1 | Three-coupled elliptic bursters system | 126 |
| 6.2 | Synchrony bifurcation for fast subsystem of three-Bautin burster system | 129 |
| 6.3 | Four-coupled Bautin elliptic burster system | 136 |
| 7 | Delay induced within-burst synchrony changes | 139 |
| 7.1 | Basics of delay differential equations | 140 |
| 7.2 | Mutually delay-coupled Bautin bursters | 142 |
| 7.2.1 | Within-burst synchrony changes via delay coupling | 143 |
| 7.2.2 | Within-burst cascade of synchrony changes via delay coupling | 144 |
| 7.3 | Conductance-based bursting model | 145 |
| 7.3.1 | Mutually delay-coupled conductance-based bursting model . | 147 |
| 7.3.2 | Within-burst synchrony changes in conductance-based model | 148 |
| 7.4 | Discussion | 150 |
| 8 | Within-burst period doubling | 152 |
| 8.1 | FitzHugh-Rinzel elliptic burster model | 152 |
| 8.2 | Coupled FitzHugh-Rinzel System | 155 |
| 8.2.1 | Within-burst bifurcation in two coupled FHR bursters . . . | 155 |

| | | |
|-----------|---|------------|
| 8.2.2 | Bifurcation analysis of the fast subsystem of two coupled FHR burster | 157 |
| 9 | Synchrony properties of the Hindmarsh-Rose neurons | 159 |
| 9.1 | The Hindmarsh-Rose model | 160 |
| 9.2 | Coupling Hindmarsh-Rose bursters | 163 |
| 9.3 | Burst synchrony clusters in 3-coupled HMR burster | 164 |
| 9.4 | Example of burst cluster in larger network of Hindmarsh-Rose bursters and discussion | 167 |
| 10 | Conclusion | 171 |
| 10.1 | Summary of thesis | 171 |
| 10.2 | Biological implication | 173 |
| 10.3 | Future research | 174 |

List of Figures

| | | |
|-----|--|----|
| 1.1 | Neuronal bursting examples (from [56]). | 23 |
| 1.2 | Hysteresis loop generating bursting rhythm governed by the system (1.1). The broken arrows show trajectory of the dynamics. The solid arrows show the direction of the vector field. | 31 |
| 1.3 | Schematic bifurcation diagram for the Chay-Keizer model depicting the z -shaped fast subsystem in cV -plane. Stable and unstable steady state solutions are shown with solid and dash-dotted lines, respectively. The bold solid lines show the maxima and minima of the periodic branch. . . | 36 |
| 1.4 | Examples of types of bursting oscillations (from [93]): (top) square- wave bursting, (middle) elliptic bursting and (bottom) parabolic bursting. Here the vertical axis shows the voltage of the oscillations. | 37 |
| 2.1 | Bifurcations at the onset and offset of bursting oscillations. | 45 |
| 2.2 | Topological classification of generic fast-slow bursters having two-dimensional fast (spiking) subsystem (from [56]). | 48 |
| 2.3 | The elliptic bursting pattern generated by the system (2.13). The time series plots the real part of z (solid line) and the corresponding slow variable u (broken line). The parameters are $a = 0.8$, $\omega = 3$ and $\eta = 0.1$. . . | 59 |
| 2.4 | The parabolic shape of the function $y = u + \beta x - x^2$. The intercept, u , on the y -axis and the tangent, β , at $x = 0$ are also shown. | 62 |

| | | |
|-----|---|----|
| 2.5 | The dynamics of the equilibria governed by (2.15) and (2.16) as u is changed from negative to positive while keeping β constant and positive. In the panels (a) and (b), y against $x = r^2$ is shown, while in (c) and (d), $r' = ry$ is shown against r^2 | 63 |
| 2.6 | The dynamics of the equilibria governed by (2.15) and (2.16) as β is changed from $\beta > \beta_{crit}$ (a.c) to $\beta < \beta_{crit}$. In the panel (a) and (b), dynamics of xy are shown, and in (c) and (d) the corresponding phasespaces are displayed. | 64 |
| 2.7 | The curve of $\beta = \sqrt{4u}$ (FLC) in $u\beta$ -plane. This curve shows the locality of the fold (saddle-node) bifurcation of limit cycles in the co-dimension plane. Sub- and supercritical Andronov-Hopf bifurcation and Bautin bifurcation are shown. | 66 |
| 3.1 | The leech nervous system with 21 ganglia (from [64]). | 70 |
| 3.2 | Sketch of the leech heartbeat rhythm-generating network. | 71 |
| 3.3 | (A) shows a simultaneous intracellular recordings of the elemental oscillator consisting of left and right heart interneuron indicated by (L,3) and (R,3), respectively, in ganglion 3. (B) shows extracellular recordings from three left heart interneurons indicated as (L,2), (L,3) and (L,4); Note that the cells (L,3) and (L,4) fire approximately inphase and both of these cells fire approximately antiphase with cell (L,2) (from [74, 80]). | 71 |
| 3.4 | A half-centre oscillator. The filled circles at the end of the links indicate inhibitory connection. | 73 |
| 3.5 | Distinguishing burst and spike synchronization in two coupled FitzHugh-Rinzel bursters (8.2). In both cases the system is burst synchronized, but (left) the excitatory coupling renders inphase spikes and (right) inhibitory gives antiphase spikes. | 74 |
| 3.6 | Example of (middle) transition of spikes from inphase synchronization to asynchronization towards the end of the burst in coupled Morris-Lecar square-wave bursters with an additional slow variable (from [59]). | 78 |

- 3.7 Schematic bifurcation diagram for z for the fast subsystem of (3.8) on varying u . SFP denotes the stable fixed point, UFP unstable fixed point, SPO stable periodic orbit and UPO unstable periodic orbit. It is clearly seen that at $u = 0$, the system undergoes subcritical Andronov-Hopf bifurcation, while saddle node bifurcation of limit cycles occur at $u = -1$ 82
- 3.8 Dynamics of a single compartment Bautin Burster governed by (3.8) and (3.11). In panel (a), the timeseries of $Re(z)$ is shown with solid line and the corresponding slow variable, u , with dashed line. The parameters for the simulation are $\omega = 3$, $a = 0.8$, $\eta = 0.1$, $\sigma = 4$, and $r_m = 1.35$. The arrows in (d) indicates the direction of change of the slow variable, u 83
- 3.9 Within-burst synchrony change from stable inphase to stable antiphase states for two coupled bursters. The dashed box shows the activity pattern of one burst and the burst repeats periodically and within-burst synchrony change repeats during each burst. This result is obtained from simulation of (3.4), (3.5) and (3.6) for $n = 2$, and parameters $\kappa_1 = 0.001$, $\kappa_2 = 0.2$, $\sigma = 3$, $\eta = 0.005$, $r_m = 1.35$, $\omega = 0.01$. Noise of amplitude 10^{-5} was added to the fast subsystem. In this figure, the two coupled bursters are burst synchronized and the spikes become inphase at the beginning of the burst, but changes to antiphase near the middle of the burst. The inset in the topmost panel shows the region of the transition. Note that the initial transient and sudden change in the synchrony pattern along the burst profile are observable from d_{12} , where $d_{12} = 0$ indicates inphase synchronization. 85
- 3.10 Within-burst synchrony change from stable antiphase to stable inphase states. The governing system and details as in figure 3.9 except $\kappa_2 = -0.2$. The inset in the topmost panel shows the transition in detail. In the last panel, the bump in d_{12} signifies the antiphase synchronization of the spikes within the synchronized burst. The corresponding slowly changing variables, u_1 and u_2 , are shown in the middle panel with solid and dotted lines, respectively. 87

- 4.1 Bifurcation of the fast dynamics for the coupled constrained system (4.3), plotting R_d^2 against u (see (4.6)) and parameters as in figure 3.9. The branches P_{in} and P_{anti} are the inphase and antiphase periodic branches of the system. The steady state branch is denoted by SS. Solid and dashed parts of the branches denote the stable and unstable solutions, respectively. u_{in} and u_{anti} are bifurcations giving loss of stability of the inphase and antiphase periodic orbits respectively, while u_H is the Andronov-Hopf bifurcation of SS. The dashed loop indicates how the slow dynamics generates periodic bursts. Note the switching of the trajectory from inphase to antiphase along the periodic branches implies a within-burst synchrony change. 91
- 4.2 Bifurcation diagram of ϕ against u for the burst-synchronized constrained system (4.3), where u is a parameter that slowly decreases during each burst as shown by the arrow. The parameters are $\omega = 3$, $\sigma = 3$, $r_m = 1.35$, and different κ_1 and κ_2 as indicated in the panels from (a) to (d). Note (a) corresponds to the parameters in figure 3.9 and 4.1 and (c) to that in figure 3.10. The solid lines represent stable solutions, while the unstable solutions are shown with dash-dotted lines. 95
- 4.3 Two parameter bifurcation diagram of σ against u for the fast subsystem of (4.3). The other parameters are fixed at $\kappa_1 = 0.001$, $\kappa_2 = 0.2$, and $r_m = 1.35$. There are stable inphase oscillations in region b,c, and stable antiphase oscillations in region a,b. 96
- 4.4 Two parameter bifurcation diagram of r_m against u , for system and parameters as in figure 4.3 and $\sigma = 3$. There are stable inphase oscillations in the region b,c, and stable antiphase oscillations in the region a,b. . . . 97
- 4.5 Bifurcation diagram of κ_1 against u for system and parameters as in figure 4.2(a,b) with $\kappa_2 = 0.2$. There are stable inphase oscillations in the region b,c, and antiphase in the region a,b. 97

- 4.6 Two parameter bifurcation diagram of κ_1 against u for system and parameters as in figure 4.2(c,d) $\kappa_2 = -0.2$. There are stable antiphase oscillations in the region a,b, and inphase in the region b,c. 98
- 4.7 Two parameter bifurcation diagram of κ_2 against u for system and parameters as in figure 4.2(a,b) with $\kappa_1 = 0.001$. There are stable inphase oscillations in the region b,c, and antiphase in the region a,b. 99
- 4.8 Bifurcation diagram as in figure 4.7 but $\kappa_1 = -0.001$. There are stable inphase oscillations in the region b,c, and antiphase in the region a,b. . . 99
- 4.9 Noise dependent bifurcation delays both at onset of burst from Andronov-Hopf bifurcation point at u_H and within-burst synchrony change at u_{in} for two coupled bursters (3.4, 3.5, 3.6). The trajectories for the four indicated amplitudes of added noise with same initial conditions and parameters as in figure 3.9 with $u = \frac{u_1+u_2}{2}$ are superimposed on the bifurcation diagram 4.1. The dashed arrows show the direction of trajectory during a periodic bursts. Note the delays reduce with increasing noise amplitude; this is a typical slow passage effect. 101
- 4.10 Within-burst synchrony change from stable inphase to stable antiphase states for two coupled bursters governed by the system (3.4, 3.5) and ‘gap-junction’ coupling (4.22). This pattern repeats during each burst. The parameters are $\sigma = 5$, $\kappa_1 = -0.001$, $\kappa_2 = 0.2$, $r_m = 1.35$, $\omega = 0.001$ and $\eta = 0.005$. A low amplitude noise of order 10^{-6} is added to the components of the fast subsystem. 103
- 4.11 Within-burst synchrony change from stable inphase to stable antiphase states for two coupled bursters governed by the system (3.4, 3.5) and ‘nonlinear synaptic’ coupling (4.23). This pattern repeats during each burst. The parameters are $\sigma = 5$, $\kappa_1 = -0.001$, $\kappa_2 = 0.2$, $r_m = 1.35$, $\omega = 0.003$ and $\eta = 0.005$ 103

- 5.1 Within-burst cascade of synchrony changes from stable antiphase to stable inphase to again stable antiphase states for two coupled elliptic bursters. Activity pattern of one burst (shown in box) has been blown up in (a); within-burst cascade of synchrony changes repeats during each burst and the burst repeats periodically (b). Note that the two coupled bursters are burst synchronized (b) and the spikes become antiphase at the beginning of the burst, then changes to inphase around the middle and again changes to antiphase towards the end of the burst (a). These transitions are also observable from d_{12} (c). These within-burst synchrony changes are characterized by two transitions described by (5.8). 108
- 5.2 Within-burst cascade of synchrony changes from stable inphase to stable antiphase and back to stable inphase states. The governing system and details are as in Figure 5.1 except for $\kappa_1 = 0.008$, $\kappa_2 = -0.1$ 109
- 5.3 Bifurcation diagram of ϕ against u for the burst-synchronized constrained system (5.12), where u is a parameter that slowly decreases during each burst. The parameters are $\sigma = 8$, $r_p = 1.2$, $r_q = 1.4$, $\kappa_1 = -0.008$ and $\kappa_2 = 0.1$. The solid lines represent stable solutions, while the unstable solutions are shown with dash-dotted lines. The arrow, running from right to left, shows the direction of the change of u during the active phase of the burst. Note this bifurcation diagram agrees with the synchrony changes observed in Figure 5.1. 112
- 5.4 Bifurcation diagram of ϕ against u for the burst-synchronized constrained system (5.12) with parameters $\sigma = 8$, $r_p = 1.2$, $r_q = 1.4$, $\kappa_1 = 0.008$ and $\kappa_2 = -0.1$. The solid lines represent stable solutions, while the unstable solutions are shown with dash-dotted lines. The arrow, running from right to left, shows the direction of the change of u . Note this bifurcation diagram agrees with the synchrony changes observed in Figure 5.2. . . . 113

- 5.5 Simulation of the system (5.21) showing two examples with different coupling parameters of within-burst cascade of synchrony changes. Only one burst in each example has been amplified for better observation. The burst pattern repeats with time. Each of these simulations has been obtained after a run of 10^6 steps to get rid of all transients. Note the cascade changes from inphase to antiphase spikes along the burst profile as depicted by d_{12} (thick line) and the spike activities, x_1 and x_2 , of the two bursters shown with solid and dashed lines, respectively. Note the different order in which the synchrony patterns change from inphase to antiphase and vice versa in (a) and (b). 118
- 5.6 Simulation of the system (5.21) for different k . Note the increasing number of synchrony changes in the within-burst cascades of synchrony changes as k is increased from (a) to (c). Only one burst is chosen for better depiction, and the pattern repeats with time. The time series of corresponding d_{12} is superimposed in bold line; $d_{12} = 0$ indicates inphase spikes while $d_{12} \neq 0$ indicates antiphase. 119
- 5.7 Bifurcation diagram of ϕ against u for the burst-synchronized constrained system (5.22), where u is a parameter that slowly decreases during each burst (shown with arrow). The parameters are $\kappa_1 = 0.001$, $\kappa_2 = 0.1$, $\omega = 10^{-6}$, $\sigma = 7$, $\eta = 0.005$, and $k = 13$. The solid lines represent stable solutions, while the unstable solutions are shown with dash-dotted lines. Indeed this bifurcation diagram agrees with the cascades of synchrony changes observed in Figure 5.5(a). 120
- 5.8 Simulation of the system two coupled Bautin elliptic bursters governed by the system (5.6) and (5.7) but with Ω for each burster defined by (5.23). The activity patterns for different values of k are shown. Note the increasing number of synchrony changes as k is increased from (a) to (d). Only one burst is shown and the pattern repeats each burst. The superimposed solid line indicates corresponding time series of d_{12} 122

- 6.1 Within-burst synchrony changes in three Bautin elliptic bursters governed by (6.2). Here within-burst synchrony changes from stable inphase to stable antiphase. The dashed box shows the activity pattern of one burst, the burst repeats periodically and the within-burst synchrony change appears during each burst. The parameters of the simulation are $\omega = 0.1$, $r_m = 1.35$, $\sigma = 5$, $\kappa_1 = 0.001$, $\kappa_2 = 0.2$. Noise of amplitude 10^{-5} was added to the fast subsystem of each burster. In the figure, the three bursters are burst synchronized (middle) and the spikes in the bursts are inphase at the beginning of the burst but change to antiphase near the middle of the burst. The activities, x_1 , x_2 , x_3 , of the three different bursters are shown in solid, dashed and dotted lines, respectively. The inset shows the region of transition. The bottom panel shows the corresponding pattern of d_{12} , d_{13} and d_{23} implying spike synchrony behaviour. 128
- 6.2 Another example of within-burst synchrony changes for three-Bautin elliptic bursters. The parameters and details of this simulation are same as those of Figure 6.1 except $\kappa_1 = -0.001$, $\kappa_2 = -0.2$. For this different coupling we can see the spikes are antiphase to each other at the beginning but changes to inphase past the frequency transition point at $r_m = 1.35$ along the burst profile. 129
- 6.3 Bifurcation diagram of ϕ_{12} (defined in (6.5)) against u for three coupled bursters. The parameters are $\kappa_1 = 0.001$, $\kappa_2 = 0.2$, $\sigma = 5$ and $r_m = 1.35$. Here, S(U)FP=stable (unstable) fixed point, S(U)P=stable (unstable) period and HB=Andronov-Hopf bifurcation point. u_{in} and u_{anti} , the inphase and antiphase bifurcation points, respectively, are shown with arrows. The big arrow on top shows the direction of change of u . The branches C1 and C2 are unstable solutions where spikes from two bursters are synchronized while those from the third are not. The solid (dash-dotted) lines represent (unstable) stable solutions. 130

- 6.4 The phase-space dynamics in the $\phi_{12}\phi_{13}$ -space of branches C1 and C2 of bifurcation diagram 6.3. The (un)filled circles indicate (un)stable nodes in the phase-space (after [6]). 133
- 6.5 Global bifurcation of the three-bautin burster system. One dynamically invariant triangle is shown. The local behaviour near inphase solution (one of the vertices) is shown in figure 6.3. The middle triangle shows the dynamics at the bifurcation point (figure 6.3(b)) and the right triangle shows the emergent periodic orbit via global connection [6]. 134
- 6.6 Within-burst synchrony changes for four-coupled Bautin elliptic burster system. The governing system for the simulation is same as Figures 6.1 and 6.2. The parameters of the simulation: $\kappa_1 = 0.001$, $\kappa_2 = 0.2$, $\sigma = 5$, $\eta = 0.005$, $r_m = 1.35$, $\omega = 0.0001$. Noise of amplitude of order 10^{-5} was added to all fast subsystems. Bottom panel shows the activities, x_j , of the four bursters; the four bursters are burst synchronized. The insets (a)-(c) show different blown-up sections of the spiking patterns inside the synchronized bursts. It is clear the spikes start off inphase (a) then change in region (b) to an asynchronous pattern (c). 136
- 6.7 The timeseries of d_{ij} (6.3) for four-coupled elliptic burster system. The d_{ij} 's correspond to the single snap of the synchronized burst of the four cells shown in Figure 6.6. Here the spikes start off inphase (zero d_{ij} 's) but changes to asynchronous patterns with each other. Note the bumps are irregular in the profile (nonzero d_{ij} 's) which indicate some drift of asynchronous patterns between the spikes of two bursters. 137
- 7.1 Sketch of the time evolution of a trajectory in phase space for delay differential equation (from [36]). 140
- 7.2 Cartoon of two mutually delay-coupled burster cells. 142
- 7.3 Within burst synchrony changes in the system of two mutually delay-coupled system governed by (7.5) and (7.6) for $j = 1, 2$. The parameters are $\varepsilon = 0.05$, $\omega = 0.001$, $\sigma = 3$, $\tau = 2$, $r_m = 1.35$ and $\eta = 0.004$. Low amplitude noise of order 10^{-6} is added to the fast subsystem of each system. 143

| | | |
|-----|--|-----|
| 7.4 | Within burst cascades of synchrony changes in the system of two mutually delay-coupled system governed by (7.5) and (7.7) with (a) $k = 2$ and (b) $k = 4$. The other parameters are $\varepsilon = 0.05$, $\omega = 0.001$, $\sigma = 3$, $\tau = 1$, and $\eta = 0.002$. Low amplitude noise of order 10^{-6} is added to the fast subsystems of the bursters. | 145 |
| 7.5 | Elliptic bursting pattern generated by the system 7.8, 7.9. The parameters are $g_{ca} = 4.4$, $g_k = 8$, $g_l = 2$, $v_k = -84$, $v_l = -60$, $v_{ca} = 120$, $I = 120$, $g_{kca} = 0.75$, $\Phi = 1.2$, $\varepsilon = 0.04$, and $\mu = 0.016667$ | 146 |
| 7.6 | Cartoon of two mutually delay-coupled bursters of the conductance-based system. | 147 |
| 7.7 | Within-burst synchrony changes in two coupled elliptic bursters governed by conductance-based system (7.10) and (7.11) for $n = 2$. In (a), the top panel shows a blown-up bursting activity patterns for two cells superimposed to show synchronization behaviour while the middle panel shows the section of superimposed bursting patterns generated by the two coupled bursters. The bottom panel shows time series of the corresponding slow variables. It is obvious that the bursters are burst synchronized while the spikes undergo within-burst synchrony changes – the spikes are antiphase at the beginning of the burst but change inphase towards the end. In (b), time series of d_{12} (7.12) corresponding to the synchronized burst shown in the top panel of (a) showing the synchrony change. | 149 |
| 8.1 | Bursting pattern generated by the FHR model (8.1). The parameters for the simulation are $I = 0.3125$, $a = 0.7$, $b = 0.8$, $d = 1$, $\delta = 0.08$, $\mu = 0.0001$, and in (a) $c = -0.775$ and (b) $c = -0.9$. The corresponding slow variable, y , is shown at the bottom of each panel. | 153 |
| 8.2 | Bifurcation diagram of the FHR system (8.1). The periodic trajectory is superimposed to show the dynamics of the system as the slow variable, y , varies. The parameters are $I = 0.3125$, $a = 0.7$, $b = 0.8$, $c = -0.9$, $d = 1$, $\delta = 0.08$, and $\mu = 0.0001$ | 153 |

8.3 Within-burst synchrony change in a pair of FHR burster governed by (8.2) with $n = 2$. In (a), the bottom panel shows the bursting activity pattern from both FHR neurons and the top shows the details of the fast spiking within a single burst activity from both cells. The bursters generate synchronized bursts but the spikes are inphase at the beginning and then get asynchronized via a period doubling bifurcation. (b) shows the timeseries of d_{12} corresponding to the burst in the top panel of (a). The parameters are $I = 0.3125$, $a = 0.7$, $b = 0.8$, $c = -0.775$, $d = 1$, $\delta = 0.08$, $\kappa_1 = 0.001$, $\kappa_2 = 0.2$ and $\mu = 0.00002$. A low amplitude noise of order 10^{-7} is added to the components of the fast subsystem. 156

8.4 Bifurcation diagram of the fast subsystem obtained by continuation of periodic branch of v_1 for the burst-synchronized constraint $y_1 = y_2 = y$. The parameters are same the as in Figure 8.3. Here only the upper or maxima of the periodic branch is shown. The stable periodic solutions are shown by solid line while the unstable solutions are shown by dashed line. Note the diagram for periodic branch of v_2 will be same because of symmetry. The corresponding periodic trajectories of fast variables v_1 (thin solid line) and v_2 (thin dashed line) of the full system (8.2) are superimposed to show the spike synchrony change, with $y = \frac{y_1+y_2}{2}$. Here the synchrony change occurs via a period doubling bifurcation (PD). Other bifurcation points are shown by BP. Note the bifurcation delay in the dynamics indicated by the arrow. 157

9.1 The bursting pattern generated by Hindmarsh-Rose system (9.1). The burst patterns are shown in (a) and the corresponding slow variable z is in (b). The parameters are $a = 1$, $b = 3$, $c = 1$, $d = 5$, $I = 2$, $x_0 = -1.6$, $r = 0.001$ and $s = 4$ 160

9.2 The 3D phase space structure of Hindmarsh-Rose system (9.1) in the bursting region. Details are as in Figure 9.1. 160

- 9.3 The bifurcation diagram of the Hindmarsh-Rose system (9.1). The bursting trajectory is superimposed on the bifurcation diagram to show the bursting solutions in the phase space. The stable steady state (SSS) solutions are shown with thin solid line while unstable steady state (USS) solutions are shown by dash-dotted line. SP indicates the stable periodic branch of the solution. The solid arrow shows the direction of the bursting trajectory in the phase space. Note the bifurcation delay at the onset and offset of the burst indicated by the broken arrows. F and H indicate the ‘fold’ and homoclinic bifurcations, respectively. 162
- 9.4 Array diagrams demonstrating (2, 1) (top) and (1, 2) (bottom) burst synchrony cluster states governed by the Hindmarsh-Rose system (9.3) and (9.4) for two different initial conditions with $m = 3$ and $n = 3$, $I = 3.0$ and $\kappa_p = \kappa = -0.001$ where $p = 1, \dots, m$. The initial conditions for three cells: (top) (0.1, 0, 0), (0.15, 0, 0), (0.2, 0, 0) and (bottom) (-0.1, 0, 0), (0.15, 0, 0), (0.2, 0, 0). See text for details. 165
- 9.5 Changing of the burst synchrony cluster states with input for three-HMR neurons governed by the system (9.3) and (9.4) with $n = 3$. The initial conditions in all cases are (0.1, 0, 0), (0.15, 0, 0) and (0.2, 0, 0). The input current I has been increased from (a)-(i), keeping the range of the input in the bursting regime: (a) $I = 1.8$, (b) $I = 1.9$, (c) $I = 2.0$, (d) $I = 2.2$, (e) $I = 2.7$, (f) $I = 2.9$, (g) $I = 3.0$, (h) $I = 3.1$, and (i) $I = 3.2$ 166
- 9.6 Spike synchrony properties in burst synchrony clusters of the three-coupled HMR system (9.3) and (9.4) with $n = 3$ with different input current I : (a) $I = 1.9$, (b) $I = 2.5$, (c) $I = 3.0$, (d) $I = 3.1$. The small boxes enclose spikes from synchronized bursts to signify spike synchrony patterns. Note in (a) the spikes are not exactly synchronized as in the other cases illustrated in (b), (c), and (d). (a) and (c) show (2, 1) burst synchrony cluster while full burst synchrony pattern can be seen in (b) and (d). 168
- 9.7 The array diagram showing spontaneous burst synchrony cluster in eight-HMR burster system. See text for details. 169

List of Tables

- 4.1 Comparison of the bifurcation points, r_{in} , r_{anti} , u_{in} and u_{anti} , obtained from simulations of system (4.3) and those from equations (4.18, 4.19, 4.20, 4.21) for $\kappa_1 = 0$, $\kappa_2 = 0.2$, $\sigma = 3$ and $r_m = 1.35$. . . 98
- 4.2 Comparison of the bifurcation points as in table 4.1 except $\kappa_2 = -0.2$. 99

Chapter 1

Introduction to neuronal bursters

During neuronal bursting, the slow currents drive the fast subsystem through bifurcations of equilibria and limit cycles which generate an activity pattern consisted of a relatively slow rhythmic alternation between an active phase of rapid spiking and a quiescent phase without spiking. Bursting is a multiple time scale phenomenon. To understand the dynamics of bursting, it is assumed that the fast and slow currents of the bursting cells have different time scales. Bursting is exhibited by a wide range of nerve and endocrine cells, including pancreatic β -cells [8, 20, 21, 11], respiratory pacemaker neurons in the pre-Botzinger complex [16], dopaminergic neurons of the mammalian midbrain [2], thalamic relay cells [72, 25], stomatogastric ganglion neurons in lobster [47], Aplysia abdominal ganglion neuron R15 [39, 63, 71, 86, 112], some mesencephalic V neurons in brainstem, and pyramidal neurons in the neocortex [113]. It is known that respiratory neurons in pre-Botzinger complex fire rhythmic bursts that controls animal respiration cycle and pancreatic β -cells fire rhythmic bursts that control the secretion of insulin. Moreover, many investigators have found and studied cases of intrinsic bursters like cat primary visual cortical neurons [79], cortical neuron in anesthetized cat [117], thalamic reticular neuron [111], cat thalamocortical neuron [72] and trigeminal interneuron from rat brain stem [76]. Besides, many spiking neurons can exhibit bursting if manipulated pharmacologically. If stimulated with a long pulse of DC current, mostly pyramidal neurons in layer 5 fire an initial burst

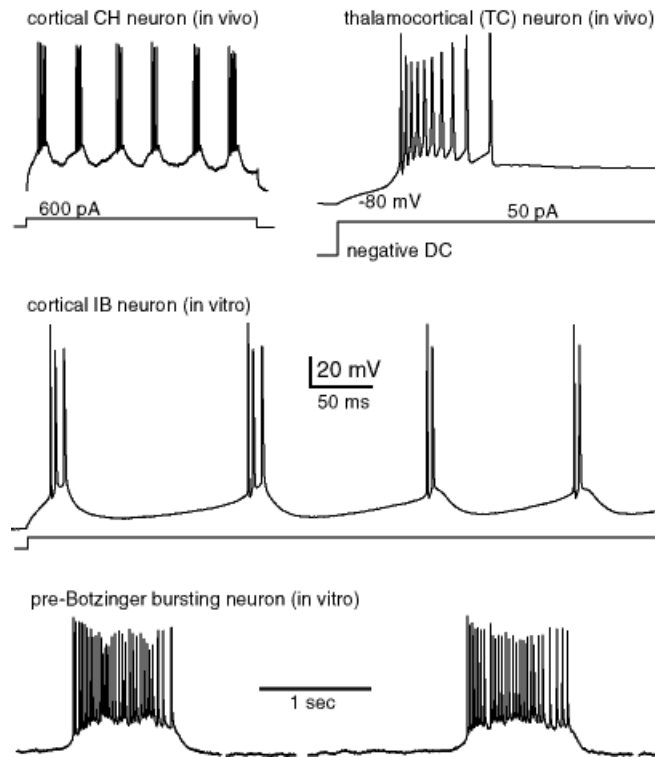


Figure 1.1: Neuronal bursting examples (from [56]).

of spikes followed by shorter bursts, and then tonic spikes [22]. Purkinji cells in cerebellar slices fire tonically but when synaptic input is blocked they can switch to bursting [123]. Thalamocortical neurons can fire bursts if inhibited and then released from inhibition [72]. Some pyramidal neurons in CA1 region of hippocampus fire high frequency bursts in response to injected pulses of current [113]. Some cortical interneurons show bursting in response to pulses of DC current [69].

1.1 Ionic mechanism of bursting

Bursting patterns are generated by a cooperative biophysical mechanism involving ionic conductances. What modulates the fast repetitive spiking once it is initiated is the slow intrinsic membrane currents. Typically, the slow currents build up during continuous spiking, hyperpolarize the cell and result in the termination of the spike train. While the cell is quiescent, the currents slowly decay, the cell recovers, and it is ready to fire another burst. So, generation of bursting involves two stages:

first to do with the initiation of sustained spiking and secondly the termination of the sustained spiking temporarily until the next burst. Biophysically, to stop the burst, spiking activity should either activate an outward current, e.g., persistent K^+ current, or inactivate an inward current, e.g., transient Ca^{2+} current. Such action can be either voltage-gated or Ca^{2+} -gated. Hence, there are at least four different ionic mechanisms of modulation of fast spiking by slow currents to produce bursting [56]. They are discussed in brief below:

- Voltage-gated slow activation of an outward K^+ current. An example of such current is M-current. Repetitive spiking slowly activates the outward current, which eventually terminates the spiking activity. While at rest, the outward current slowly deactivates, thus initiates another burst. As documented in vitro, neocortical pyramidal neurons exhibiting chattering activity have voltage-gated K^+ M-current [121] and a slow dynamics of a voltage-gated K^+ current is also seen in pre-Botzinger complex [16].
- Voltage-gated inactivation of inward Ca^{2+} transient T-current or inactivation of the h-current. Repetitive spiking slowly inactivates the inward current, and makes the neuron stop spiking eventually. While at rest, the inward current slowly deinactivates and depolarizes the membrane potential to initiate a new burst. Examples of this mechanism is found in the thalamic relay neurons [25, 72] and thalamic reticular neurons [26].
- Ca^{2+} -gated slow activation of the outward Ca^{2+} -dependent K^+ current. Calcium entry and build up during repetitive spiking slowly activate the outward current and as a result the neuron stops spiking. Then the intracellular Ca^{2+} ions are removed, the Ca^{2+} -gated outward current deactivates, and the neuron is ready to fire a new burst. Neurons in hippocampal CA3 [118], subiculum bursters [108], midbrain dopaminergic neurons [2], and anterior bursters in lobster stomatogastric ganglion [47] have Ca^{2+} -gated K^+ currents.
- Ca^{2+} -gated slow inactivation of inward high threshold Ca^{2+} currents, such as L-current. Entry of calcium during repetitive spiking leads to slow inactiva-

tion of Ca^{2+} -channels. As a result, neuron cannot sustain repetitive spiking. During quiescent state, the intracellular Ca^{2+} ion are removed, and the neuron is ready to start a new burst. Aplysia abdominal ganglion R15 neurons have an L-current [39, 63, 71, 86, 112], Moreover, midbrain dopaminergic neurons [2] and anterior bursting neurons in lobster stomatogastric ganglion [47] both contain Ca^{2+} -gated L-currents.

In addition, bursting can result from the somatic-dendritic interplay. Somatic spikes excites the dendritic tree resulting in a delayed spike which in return evokes another somatic spike, which results in another dendritic spike, and so forth. The burst stops when a somatic spikes falls into the refractory period of the dendritic spike failing to evoke dendritic response [29].

1.2 Mathematical mechanism

Most mathematical models of bursters may be written in the multiple time scale form as

$$\left. \begin{aligned} \dot{x} &= f(x, u) \\ \dot{u} &= \eta g(x, u), \end{aligned} \right\} \quad (1.1)$$

where vector $x \in \mathbb{R}^p$ describes fast variables responsible for spiking. It includes the membrane potential, activation and inactivation gating variables for fast currents, and so on. The dot implies differentiation with respect to time t . The vector $u \in \mathbb{R}^q$ describes relatively slow variables that modulate fast spiking. It includes gating variables of slow K^+ current, an intracellular concentration of Ca^{2+} ions, etc. The small parameter η represents the ratio of time scales between fast spiking and slow modulation. Typically, it is assumed that $\eta \ll 1$, and f and g in the system (1.1) are typical Hodgkin-Huxley-type functions describing the kinetics of the currents involved in the biophysical dynamics.

Mathematically, to transform a biophysical neuronal model capable of sustained spiking train into a finite burst of spikes, it suffices to add a slow resonant current or gating variable describing inactivation of an inward current or activation of an outward current that modulates the spiking via a slow negative feedback. As

realistic neuronal examples of the system (1.1) we briefly review two early models of bursters based on the ionic conductances in the cell.

1.2.1 The Plant model

The Plant model [84, 85, 86, 87] is one of the first conductance-based mathematical models developed to explain the mechanism underlying bursting oscillations observed in the membrane potential of the R15 pacemaker neuron from the abdominal ganglion of the mollusk *Aplysia* [39, 63, 71, 112]. The model involves sodium and calcium currents with instantaneous activation, a passive leak current and a Ca^{2+} -activated outward K current. The current balanced form of the Plant model may be written as

$$\left. \begin{aligned} C_m \dot{V} = & -g_I m_\infty^3(V) h(V - V_I) - g_T x(V - V_I) - g_K n^4(V - V_K) \\ & + g_{K[Ca]} \frac{[Ca]}{0.5 + [Ca]} (V - V_K) - g_L (V - V_L), \end{aligned} \right\} \quad (1.2)$$

where V is the membrane potential (mV), t is the time (ms), C_m is the membrane capacitance (fF), g_i 's are maximum ion conductances ($mmho/cm^2$), V_i 's are Nernst reversal potentials (mV), $m_\infty(V)$ is the instantaneous activation function for fast inward current, x and n are dimensionless activation variables, h is a dimensionless inactivation variable, and $[Ca]$ is the dimensionless intracellular concentration.

The equations for the activation and inactivation variables are

$$\left. \begin{aligned} \dot{h} &= \frac{h_\infty(V) - h}{\tau_h(V)} \\ \dot{n} &= \frac{n_\infty(V) - n}{\tau_n(V)} \\ \dot{x} &= \frac{x_\infty(V) - x}{\tau_x(V)}, \end{aligned} \right\} \quad (1.3)$$

here τ_i 's are the relaxation times with $i = h, n, x$, and the equation for the intracellular calcium concentration is

$$[\dot{Ca}] = \rho (K_c x (V_{Ca} - V) - [Ca]). \quad (1.4)$$

The steady state activation and inactivation functions are

$$\left. \begin{aligned} \omega_{\infty}(V) &= \frac{\alpha_{\omega}(V)}{\alpha_{\omega}(V) + \beta_{\omega}(V)} && \text{for } \omega = m, h, n \\ \tau_{\infty}(V) &= \frac{12.5}{\alpha_{\omega}(V) + \beta_{\omega}(V)} && \text{for } \omega = h, n \\ x_{\infty}(V) &= \frac{1}{\exp(-0.15(V + 50)) + 1}, \end{aligned} \right\} \quad (1.5)$$

with

$$\left. \begin{aligned} \alpha_m(V) &= 0.1 \frac{50 - V_s}{\exp((50 - V_s)/10) - 1} \\ \beta_m(V) &= 4 \exp((25 - V_s)/18) \\ \alpha_h(V) &= 0.007 \exp((25 - V_s)/20) \\ \beta_h(V) &= \frac{1}{\exp((55 - V_s)/10) + 1} \\ \alpha_n(V) &= 0.01 \frac{55 - V_s}{\exp((55 - V_s)/10) - 1} \\ \beta_n(V) &= 0.125 \exp((45 - V_s)/80) \\ V_s &= \frac{127}{105}V + \frac{8265}{105}. \end{aligned} \right\} \quad (1.6)$$

The parameters are $C_m = 1\mu F/cm^2$, $g_I = 4.0mmho/cm^2$, $g_T = 0.01mmho/cm^2$, $g_L = 0.003mmho/cm^2$, $V_I = 30mV$, $V_K = -75mV$, $V_L = -40mV$, $V_{Ca} = 140mV$, $\rho = 0.0003ms^{-1}$, $K_c = 0.0085mV^{-1}$, and $\tau_x = 235ms$. Plant obtained from simulation of the model bursting pattern as observed in the Aplysia R15 cell. Electrophysiologically, the bursting is generated by the interplay of the fast inward sodium and calcium currents with instantaneous activation. The second and fourth ion currents in the equation (1.2) operate on much slower time scales. Here the second current is an inward current with slow activation, and the fourth current is an outward current carried by potassium ions, sensitive to slow buildup of intracellular calcium ions. One experimental observation was that when poison tetrodotoxin of the puffer fish is applied to membrane of the R15 cell, the burst action potentials disappear and an underlying slow periodic membrane oscillation emerges. In the Plant balance equation (1.2), the second current is the tetrodotoxin-resistant inward current with slow activation. The model can produce the slow oscillations in the membrane in the presence of tetrodotoxin with $g_I = 0$.

1.2.2 The Chay-Keizer model

The Chay-Keizer model [21, 8, 20, 11] is one of the earliest bursting models developed to explain the bursting mechanism of the insulin secreting pancreatic β -cell. This model is based on the idea of negative feedback by cytosolic Ca^{2+} as a driving mechanism for bursting for pancreatic β -cells. The cytosolic Ca^{2+} , according to the Chay-Keizer model, acts on a Ca^{2+} -activated K^+ channel. The Ca^{2+} feedback hypothesis has emerged successful since then in many areas of cellular Ca^{2+} mechanism including sequestration and release by the endoplasmic reticulum, and exotic effects on metabolism, including mitochondrial respiration and glycolytic oscillations [23]. We present a modification of the Morris-Lecar model [73] incorporating the cytosolic Ca^{2+} dynamics in the spirit of the Chay-Keizer model discussed by Richard Bertram and Arthur Sherman in [23]. The balance equation of the pancreatic β -cell may be written as

$$C_m \dot{V} = - (I_{Ca} + I_K + I_{K(Ca)} + I_{K(ATP)}), \quad (1.7)$$

where C_m is the membrane capacitance of the cell, V is membrane potential, I_{Ca} is an inward Ca^{2+} current, I_K is an outward K^+ current of the delayed rectifier type, $I_{K(Ca)}$ is a Ca^{2+} -activated K^+ current and $I_{K(ATP)}$ is an adenosine triphosphate (ATP)-sensitive K^+ current. The dynamics of the activation variables, n , for I_K is given by

$$\dot{n} = \lambda \frac{(n_\infty(V) - n)}{\tau_n}, \quad (1.8)$$

where $n_\infty(V)$ is the I_K activation equilibrium function, τ_n is the activation time constant, and λ is a parameter which may be used to speed up or slow down time scale of the variable n .

The Chay-Keizer model is based on the hypothesis of Atwater [8] that bursting in the β -cell is due to the slow rise and fall of the cytosolic Ca^{2+} concentration, c , acting on $K(Ca)$ (Ca^{2+} -activated K) channels. Increasing c increases the outward $K(Ca)$ current. The dynamics of the cytosolic Ca^{2+} concentration, c , is expressed in the following differential equation

$$\dot{c} = -f_{cyt}(\alpha I_{Ca} + K_{pmca}c), \quad (1.9)$$

where f_{cyt} is the fraction of cytosolic Ca^{2+} that is not bound to buffers, the term in the parenthesis, $-(\alpha I_{Ca} + K_{pmca}c)$, describes the Ca^{2+} flux across the plasma membrane where parameter α converts current to flux, and K_{pmca} indicates the pump rate. The Ca^{2+} influx is through Ca^{2+} channels and the efflux is through Ca^{2+} pumps (Ca^{2+} APTases). The additional equations of the system are

$$\left. \begin{aligned} I_{Ca} &= g_{Ca}m_{\infty}(V)(V - V_{Ca}) \\ I_K &= g_Kn(V - V_K) \\ I_{K(Ca)} &= g_{K(Ca)}\frac{c^3}{c^3 + K_D^3}(V - V_K) \\ I_{K(ATP)} &= g_{K(ATP)}(V - V_K) \\ m_{\infty}(V) &= (1 + \exp((v_m - V)/s_m))^{-1} \\ n_{\infty}(V) &= (1 + \exp((v_n - V)/s_n))^{-1} \end{aligned} \right\} \quad (1.10)$$

This three variable (V, n, c) -model is able to reproduce the bursting activity of the pancreatic β -cell. The parameters are $g_{Ca} = 1000pS$, $g_K = 2700pS$, $g_{K(Ca)} = 400pS$, $g_{K(ATP)} = 180pS$ ($1S(Siemens) = 1mho$), $V_{Ca} = 25mV$, $V_K = -75mV$, $C_m = 5300fF$, $\lambda = 1$, $\tau_m = 20ms$, $K_D = 0.4\mu M$, $v_n = -16mV$, $v_m = -20mV$, $s_n = 2mV$, $s_m = 12mV$, and $f_{cyt} = 0.00025$. Obviously, as f_{cyt} is very small, the dynamics of the cytosolic Ca^{2+} concentration is very slow in comparison to that of V and n . This interplay of the slow-fast dynamics of the governing variables of the system generates bursting. The concentration, c , rises during the active or oscillatory phase, Ca^{2+} channels are mostly open to help accumulation of Ca^{2+} in the cell. Because of the very large effective time scale c rises very slowly. The rise in c activates $K(Ca)$ current. Eventually, c rises to a large enough value to terminate the active phase of spiking. Now that the system has entered the silent or steady state phase, the Ca^{2+} channels close. As a result, hyperpolarizing $K(Ca)$ current is shut off. Eventually the cell again returns to spiking active phase and thus activity pattern results in bursting.

1.3 Mathematical properties and analysis of bursting models

It may be observed from above discussion of the mathematical models for bursting of Aplysia R15 cell and pancreatic β -cell that the system of equations generating bursting is higher dimensional and the dynamics involve multiple time scale properties. The phase space of the bursting models is at least three-dimensional. The fast subsystem oscillates between stable periodic (spiking) state and stable steady (quiescent) state as the slow subsystem varies in bursting. This implies the existence of hysteresis loop in the periodic bursting or a bistability of spiking and resting states. Multiscale and multidimensionality make the bursting models very challenging to analyze mathematically even for a single compartment system. The task gets harder or even impossible in case of coupled bursters system, only numerical simulation may be carried out to study such system.

Typically, bursting is viewed within the context of system with multiple time scale from perspective of singular perturbation theory. Most work has focused on the ‘slow motion’ of the system during quiescent and active portion of the bursting cycle. During these epochs, the system state is described by attractors that evolve on the slow time scale. The transition between quiescent and active states can be classified by bifurcations of the fast subsystem. Among the very first attempts to understand the mathematical mechanism underlying bursting, Rinzel and Lee [92] decomposed the Plant model into a fast and a slow subsystem based on the singular limit of an infinite separation of time scales, the slow variables of the system remain fixed on the fast time scale and become parameters in the fast subsystem. Moreover, using singular perturbation method, Rinzel and Lee [92] showed that the mechanism underlying bursting models for R15 differs from the mechanism in models of bursting for the pancreatic β -cells. This analytical observation is an impetus for a description of formal classification schemes of bursters and reduction to simpler models. In what follows in this chapter, we discuss the hysteresis loop of bursts and the bifurcation scenarios of the fast subsystem that emerge from a

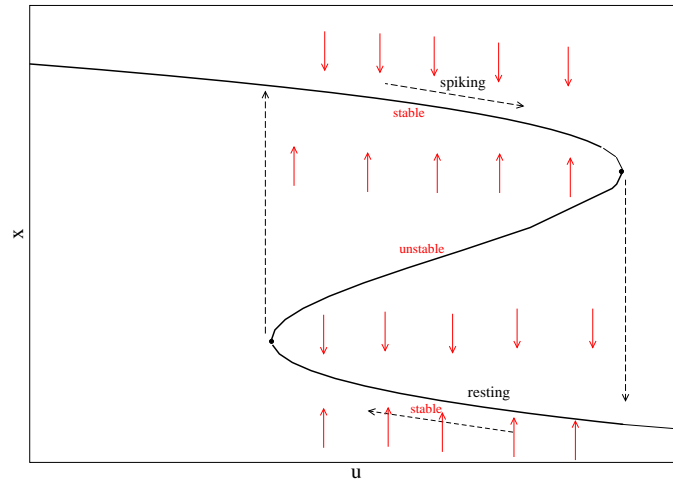


Figure 1.2: Hysteresis loop generating bursting rhythm governed by the system (1.1). The broken arrows show trajectory of the dynamics. The solid arrows show the direction of the vector field.

singular perturbation analysis. This eventually leads our review to the topological classification scheme and reduced canonical modeling of the bursters.

1.3.1 Hysteresis loop

Sustained bursting activity of the multiple time scale system (1.1) corresponds to periodic activity of the slow subsystem. There could be two fundamentally different ways the slow subsystem oscillates depending on the dimension or number of the slow variable. If the slow variable is one-dimensional, then there must be co-existence of the equilibrium and limit cycle attractors of the fast subsystem, that is, there is a bistability of resting and spiking states. So the slow variable oscillates via a hysteresis loop. Let us consider system (1.1) with $p = 1$ and $q = 1$, we note that when the fast variable x is in spiking state, the slow variable, governed by the equation $\dot{u} = \eta g(x, u)$, is pushed toward the quiescence or resting state, and spiking abruptly stops which corresponds to a bifurcation of the fast subsystem (see Figure 1.2). Again, when the fast variable is quiescent, the slow variable is pushed toward the spiking state and after a while spiking abruptly starts via a bifurcation of the fast subsystem. Such a hysteresis loop bursting can also occur where the slow variable is multidimensional. In this case, the vector field pushes

the slow variable, u , outside the top (spiking) area, whereas the vector field on the bottom (resting) area pushes u outside the resting area. As a result, the slow variable visits the spiking and resting areas periodically, and the model generates bursting.

Another interesting phenomenon corresponding to hysteresis is burst excitability [59, 56]: a neuron with quiescent excitable dynamics responds to perturbations by generating not a single spike but bursting. An example of this is the neurons in the hippocampus which produce bursting in response to a brief stimuli [113].

1.3.2 Geometric singular perturbation method

Models for bursting involve variables that evolve on different time scales. The existence of different time scales naturally leads to models containing small parameters. Geometric singular perturbation theory [103, 93] provides a powerful technique for analyzing these models. The theory gives a systematic way to reduce systems with parameters to lower dimensional reduced systems that are more easily analyzable. In this section, to begin with, we illustrate how this method works with a simple example and later discuss more complicated models.

In the system (1.1) (we consider $p = q = 1$ for clarity) η is the small, singular perturbation parameter. We assume that x -nullcline governed by $f(x, u) = 0$ is a cubic shaped curve and the u -nullcline governed by $g(x, u) = 0$ is a monotone increasing curve that intersects the cubic at a single fixed point that lies along the middle branch of the z -shaped cubic at a single fixed point lies along the middle branch of the z -shaped cubic nullcline (see Figure 1.2). We also need to assume $\dot{x} > 0 (< 0)$ right (left) the cubic x -nullcline and $\dot{u} > 0 (< 0)$ left (right) the u -nullcline. Using the Poincare-Bendixson theorem, one can prove that system (1.1) has a limit cycle for all η sufficiently small [93]. Moreover, the limit cycle approaches a singular limit cycle as $\eta \rightarrow 0$. The bottom branch of the cubic nullcline that corresponds to the quiescent phase of an action potential. Another singular solution lies along the upper branch of the cubic nullcline that corresponds to the active phase of the action potential. The jump up to the active phase occurs

at the left knee of the cubic and the jump down to the quiescent phase occurs at the right knee of the cubic.

The system (1.1) is referred to as a singular perturbation problem because the structure of (1.1) with $\eta > 0$ is very different than the structure of solutions of (1.1) with $\eta = 0$. If we set $\eta = 0$, then (1.1) reduces to the ‘fast subsystem’

$$\left. \begin{aligned} \dot{x} &= f(x, u) \\ \dot{u} &= 0. \end{aligned} \right\} \quad (1.11)$$

Note u is a constant along every solution of (1.11); that is every trajectory is vertical in xu -space. The fixed point set is the entire cubic shaped curve, $f(x, y) = 0$. This is very different from (1.1) with $\eta > 0$ in which there is only one fixed point and u is not a constant along all other solutions. The reduced system (1.11) gives a good approximation of solutions away from the cubic x -nullcline. In particular, it determines the evolution of the jump up and jump down portions of the singular solution governed by $\dot{x} = f(x, u)$, which correspond to the onset and offset of spikes, respectively. The first equation of the reduced system (1.11) is called the ‘fast subsystem’. In order to determine the behaviour of solutions near the cubic nullcline, that is, during the active and quiescent phases, we introduce the slow time scale $\tau = \eta t$. In terms of this slow time scale, the system (1.11) transform to

$$\left. \begin{aligned} \eta x' &= f(x, u) \\ u' &= g(x, u), \end{aligned} \right\} \quad (1.12)$$

where $' = d/d\tau$. Now by setting $\eta = 0$, we obtain the reduced system

$$\left. \begin{aligned} 0 &= f(x, u) \\ u' &= g(x, u). \end{aligned} \right\} \quad (1.13)$$

The first equation in the system (1.13) implies that its solution lies along the cubic nullcline. The second equation in (1.13) determines the evolution of the solution along the nullcline. Note if we write the active (top) and quiescent (bottom) branches of the z -shaped nullcline (Figure 1.2) as $x = F_a(u)$ and $x = F_q(u)$, respectively, then the second equation in (1.13) may be written as

$$u' = g(F_i(u), u), \quad (1.14)$$

where $i = a, q$.

Note each piece of the singular solution is determined by a single, differential equation. The active and quiescent phases correspond to the solution of (1.14). This equation is called ‘slow subsystem’. Thus, using the existence of small parameters, singular periodic solution are constructed. Each piece of the singular solution satisfies a reduced system of equations (1.11) and (1.13). Thus, geometric singular perturbation method reduces higher dimensional dynamical systems with multiple time scales or small parameters to low dimensional fast subsystem and slow subsystem. This decomposition of the dynamics into fast and slow counterparts is also known as dissection method in theoretical neuroscience.

To analyze bursters in the spirit of geometric singular perturbation method, it is assumed that $\eta = 0$ in the burster model governed by the system like (1.1), so that the fast and slow systems can be treated separately. This dissection method for neuronal bursting was pioneered by Rinzel [89, 92]. His study showed that many important aspects of bursting behaviour can be understood via phase portrait analysis of the fast subsystem, $\dot{x} = f(x, u)$, with $x \in \mathbb{R}^p$, treating $u \in \mathbb{R}^q$ as a vector of slowly changing bifurcation parameters. The fast subsystem can be resting (but excitable), bistable, or spiking depending on the value of u , bursting occurs when u visits the spiking and quiescent areas periodically. Now we will dwell briefly on the dissection of the Plant model and Chay-Keizer model for pancreatic β -cell to understand the dynamical mechanism underlying bursting.

Dissection of the Plant model

Rinzel and Lee [92] analyzed the Plant model (1.2)–(1.6) by decomposing it into a fast and slow subsystem based on the separation of time scales on which the ion currents operate. As we saw, the fast subsystem of the Plant model consists of the equations for membrane potential V , and (in)activation variables h and n , and the slow subsystem consists of the equations for the activation variable x and the intracellular calcium concentration $[Ca]$. In the geometric singular perturbation approach, the slow variable x is held constant and the other slow variable $[Ca]$

used as the bifurcation parameter. By varying $[Ca]$ slowly, the key feature of the fast subsystem of the Plant model obtained is that its bifurcation diagram contains a branch of steady states corresponding to the quiescent periods between bursts and a branch of periodic solutions corresponding to the action potentials within bursts. These two branches are connected via a saddle-node on invariant circle (SNIC) bifurcation. Bursting is obtained from an oscillation in the slow system that periodically moves the $[Ca]$ back and forth across the SNIC bifurcation, from the branch of steady states to the branch of periodic solutions, and vice versa. An interesting feature of the model observed from the dissection is that since the transition between the active and quiescent phases of bursting involves passing through a SNIC bifurcation, which is associated with a limit cycle with infinite period, the spike frequency is low at the beginning of the burst, then increases, and then decreases again towards the end of the burst. This successful dissection of the Plant model by Rinzel and Lee contributed to a deep understanding of the mechanism underlying bursting dynamics and popularization of the geometric perturbation method in the analysis of neuronal bursters.

Dissection of the Chay-Keizer model

The Chay-Keizer model (1.7)–(1.10) describes the bursting dynamics of the pancreatic β -cells. The fast subsystem of the model consists of equations (1.7) and (1.8), with fast variables V and n . The calcium concentration, c , is the single slow variable. In the singular perturbation limit, c , is treated as a parameter of the fast subsystem. In the cV -phase plane, the bifurcation diagram of the fast subsystem is z -shaped (see Figure 1.3). This is called the slow manifold or z -curve on which V and n are at steady state. The c -nullcline has the property $\dot{c} < 0$ below and $\dot{c} > 0$ above. There are three branches of z -shaped V -nullcline: the lower branch corresponds to the stable steady state of the fast subsystem which joins to the middle branch of unstable saddle point at the knee of the z -curve via a saddle-node (SN) bifurcation. The middle saddle point branch ends at a second SN bifurcation with the third and upper branch of the V -nullcline of unstable equilibria. The

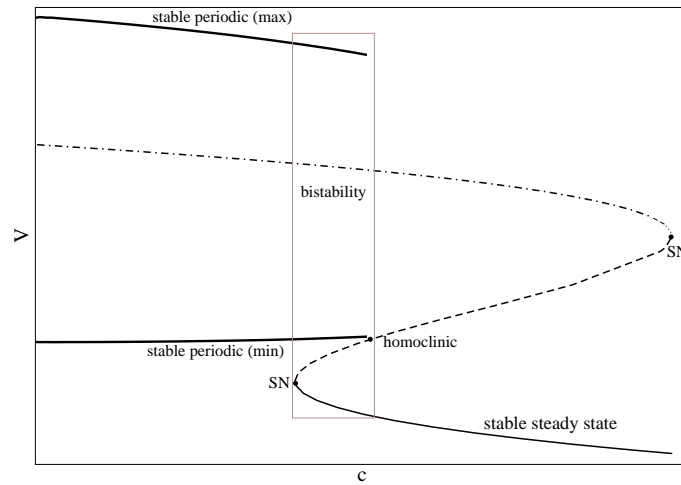


Figure 1.3: Schematic bifurcation diagram for the Chay-Keizer model depicting the z -shaped fast subsystem in cV -plane. Stable and unstable steady state solutions are shown with solid and dash-dotted lines, respectively. The bold solid lines show the maxima and minima of the periodic branch.

branch of upper unstable equilibria continues for lower values of c , and eventually goes through a supercritical Andronov-Hopf bifurcation. Beyond this the branch is stable. A branch of stable periodic solutions emerges from the Andronov-Hopf bifurcation. Each of these periodic solutions represents a continuous train of action potentials. The periodic branch terminates at a homoclinic bifurcation, where the limit cycle connects the saddle point forming an infinite-period homoclinic orbit. A bistability occurs for all values of c between the first SN and the homoclinic bifurcation shown by the box in Figure 1.3. The bistability of the fast subsystem is apparently a crucial feature of bursting in general, without it there would be no bursting. During the quiescent phase, the burst trajectory rides along the bottom branch of the z -shaped V -nullcline traveling to the left since it is below the c -nullcline ($\dot{c} < 0$). When the trajectory reaches the SN bifurcation it moves to the periodic branch, since the limit cycle is now the only remaining attractor. At this point the trajectory travels rightward since it is above the c -nullcline and $\dot{c} > 0$. The active phase ends when the trajectory reaches the homoclinic bifurcation. This completes one cycle of bursting. Thus, slow-fast dissection of the model unravels the underlying mechanism of bursting.

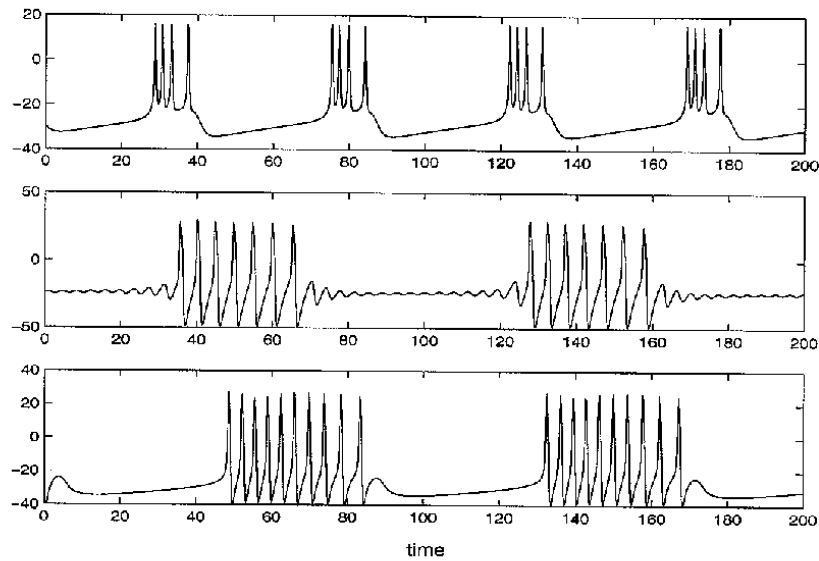


Figure 1.4: Examples of types of bursting oscillations (from [93]): (top) square-wave bursting, (middle) elliptic bursting and (bottom) parabolic bursting. Here the vertical axis shows the voltage of the oscillations.

1.4 Rinzel's classification of bursting oscillations

Dissection of the Plant model for *Aplysia* R15 cell and the Chay-Keizer model for pancreatic β -cell shows quite clearly that the bursting dynamics of two systems are qualitatively very different. The dissection method to analyze the bursting models culminated into different classification schemes of bursters by many investigators such as Rinzel [92], Bertram et al. [11], de Vries [24], Izhikevich [56, 58, 59], and Golubitsky [40]. In this section we review three classes of bursting oscillations proposed by Rinzel in [92]: square-wave bursting, elliptic bursting and parabolic bursting. This classification is based on the qualitative properties of burst activity like voltage amplitude profile and interspike frequency. Each class of bursting is governed by a system of the form (1.1) and different classes of bursting oscillations follow from geometric assumptions concerning the set of fixed points and periodic solutions of the fast subsystem. Some assumptions can usually be verified for a specific system by using numerical software [93].

1.4.1 Square wave bursting

Square-wave bursting is exhibited by pancreatic β -cells and the Chay-Keizer model can reproduce this burst pattern for electric activity. This oscillatory pattern is referred to as square-wave bursting due to the ‘box-shaped’ amplitude profile for the voltage or action potential. There are some phenomenological, polynomial models like Hindmarsh-Rose [50, 48, 49, 100], Pernarowski [83] and G. de Vries et al. [24] models. It is also ubiquitous in many systems like Alexander-Cai [1], Wang [120, 119] and Chay-Cook [11] models. Moreover, square-wave bursting also arises in recent models for respiratory CPG (central pattern generator) neurons and models for pattern generation based on synaptic depression [93]. Mathematically, square-wave bursting requires three-dimensional systems and in the discussion of the Chay-Keizer model we observe the square-wave bursting arises from the system containing two-dimensional (V, n) fast subsystem (1.7,1.8) and one-dimensional (c) slow subsystem (1.9). Besides, square-wave bursting can also be generated by system with two slow variables. Analysis of models with two slow variables which exhibit this type of bursting is discussed in [104]. Typically, the dynamical mechanism underlying square-wave bursting is that the rest state disappears via fold bifurcation, and the periodic spiking disappears via saddle-homoclinic orbit bifurcation. A crucial ingredient for square-wave bursting is bistability as there is a coexistence of attractors. This allows for a hysteresis loop between a lower branch of stable fixed points and upper branch of stable limit cycles. Terman [93] studied the dynamical aspects of fold and homoclinic bifurcations of square-wave bursting comprehensively and showed that this burster could have a Smale horseshoe structure leading to chaotic dynamics. Rinzel and Ermentrout [91] give the following system of equations which generate square-wave bursting:

$$\left. \begin{aligned} \dot{v} &= -(g_{ca}m_{\infty}(v)(v - v_{ca}) + g_k w(v - v_k)) \\ &\quad g_l(v - v_l) + g_{kca}z(y)(v - v_k) + I \\ \dot{w} &= 20\Phi(w_{\infty}(v) - w) / \tau(v) \\ \dot{y} &= 20\varepsilon(-\mu g_{ca}m_{\infty}(v)(v - v_{ca}) - y), \end{aligned} \right\} \quad (1.15)$$

where $g_{ca} = 4$, $g_k = 8$, $g_l = 2$, $v_k = -84$, $v_l = -60$, $v_{ca} = 120$, $I = 45$, $g_{kca} = 0.25$, $\Phi = 0.23$, $\varepsilon = 0.005$, and $\mu = 0.02$. In addition, the nonlinear functions are

$$\left. \begin{aligned} m_\infty(v) &= 0.5 (1 + \tanh((v + 1.2)/18)) \\ w_\infty(v) &= 0.5 (1 + \tanh((v - 12)/17.8)) \\ z(y) &= y/(1 + y) \\ \tau(v) &= \cosh((v - 12)/34.8). \end{aligned} \right\} \quad (1.16)$$

1.4.2 Parabolic bursting

Parabolic bursting is found in the Aplysia R15 neuron [39, 63, 71, 112] and its mathematical model is due to Plant reviewed earlier. The bifurcation signature of this type of bursting is that the transition from quiescent state to repetitive spiking and back occurs via a saddle-node on invariant circle (SNIC) bifurcation. Since SNIC bifurcation is associated with a limit cycle of infinite period, the interspike interval is longer at both the beginning and end of each burst; typically, the frequency of emerging and terminating spiking may be shown to behave as $\sqrt{\lambda}$, where λ is the distance to the bifurcation [93]. It accounts for the parabolic shape of the interspike period of fast oscillations which is the motivation behind the name parabolic bursting. Unlike square-wave bursting, parabolic bursting can be achieved in a system with at least two slow variables and it does not arise from a hysteresis phenomenon. Regarding the mathematical structure of parabolic bursters note the Plant model for Aplysia R15 neuron contains three-dimensional (Vhn)-fast subsystem and two-dimensional $x[Ca]$ -slow subsystem. Rigorous results related to parabolic bursting are given by Kopell and Ermentrout in [35], C. Soto-Trevin et al. in [107] and Hoppensteadt and Izhikevich in [51]. The following equations [91], produce parabolic bursting:

$$\left. \begin{aligned} \dot{v} &= -(i_{ca}(v) + i_k(v) + i_l(v) + i_{kca}(v, c) + i_{cas}(v, s)) + I \\ \dot{w} &= \Phi (w_\infty(v) - w) / \tau_w(v) \\ \dot{c} &= \varepsilon (-\mu g_{ca} m_\infty(v)(v - v_{ca}) - c) \\ \dot{s} &= \varepsilon (s_\infty(v) - s) / \tau_s, \end{aligned} \right\} \quad (1.17)$$

with

$$\left. \begin{aligned} i_{ca}(v) &= g_{ca}m_{\infty}(v)(v - v_{ca}) \\ i_k(v) &= g_k w(v - v_k) \\ i_l(v) &= g_l(v - v_l) \\ i_{kca}(v, c) &= g_{kca}z(c)(v - v_k) \\ i_{cas}(v, s) &= g_{cas}s(v - v_{ca}), \end{aligned} \right\} \quad (1.18)$$

and the nonlinear functions are given by

$$\left. \begin{aligned} m_{\infty}(v) &= 0.5(1 + \tanh((v + 1.2)/18)) \\ w_{\infty}(v) &= 0.5(1 + \tanh((v - 12)/17)) \\ \tau_{\infty} &= \cosh((v - 12)/34) \\ z(c) &= c/(1 + c) \\ s_{\text{inf}} &= 0.5(1 + \tanh((v - 12)/24)). \end{aligned} \right\} \quad (1.19)$$

The constants are $g_{ca} = 4$, $g_k = 8$, $g_l = 2$, $v_k = -84$, $v_l = -60$, $v_{ca} = 120$, $I = 65$, $g_{kca} = 1$, $\Phi = 1.333$, $\varepsilon = 0.002$, $\mu = 0.025$, $\tau_s = 0.05$, and $g_{cas} = 1$.

1.4.3 Elliptic bursting

Elliptic bursting is the last of the three basic types of bursting oscillations identified by Rinzel in [92]. It is referred to as ‘elliptic’ in the literature because the profile of oscillation of the membrane potential resembles an ellipse. Elliptic bursting arises in the models for thalamic neurons [27], rodent trigeminal neurons [76], and 40 Hz oscillations [120]. It is also exhibited by the FitzHugh-Rinzel [38, 90, 61, 53, 56, 61, 59, 89], Rush-Rinzel [94], Chay-Cook [11], Wu-Baer [124], and Pernarowski polynomial [83] models. Both square-wave and elliptic bursting depend on bistability and hysteresis because there is a coexistence of resting and spiking states and such bursting usually occurs via a hysteresis loop with only one slow variable. An important difference between these two types of bursting is how the active phase terminates. Square-wave bursting ends at a homoclinic bifurcation, therefore the period of oscillations increases at the end of each burst. Whereas in elliptic bursting the quiescent state loses stability via subcritical

Andronov-Hopf bifurcation, and the periodic limit cycle attractor corresponding to the active state disappears via a saddle-node of periodic orbits or fold limit cycle bifurcation. Hoppensteadt and Izhikevich [51] showed that elliptic bursting is also possible even if the branch of periodic orbits of fast subsystem originate at a supercritical Andronov-Hopf bifurcation. A prominent feature of elliptic bursting shares with systems of fast-slow oscillations involving Andronov-Hopf bifurcation is that the transition from resting (quiescent) state to active (spiking) state does not occur immediately at the moment the resting state becomes unstable. The fast subsystem remains at the unstable equilibrium for quite some time before it jumps rather abruptly to a spiking state. This delayed transition is known as the slow passage effect. In Section 2.4 we discuss briefly the slow passage effect with its implications in bursting. To end the discussion of elliptic bursting, we reproduce the following system of equations which produce elliptic bursting [91]:

$$\left. \begin{aligned} \dot{v} &= -(g_{ca}m_{\infty}(v)(v - v_{ca}) + g_k w(v - v_k)) \\ g_l(v - v_l) + g_{kca}z(y)(v - v_k) + I \\ \dot{w} &= \Phi(w_{\infty}(v) - w) / \tau(v) \\ \dot{y} &= \varepsilon(-\mu g_{ca}m_{\infty}(v)(v - v_{ca}) - y), \end{aligned} \right\} \quad (1.20)$$

with

$$\left. \begin{aligned} m_{\infty}(v) &= 0.5(1 + \tanh((v + 1.2)/18)) \\ w_{\infty}(v) &= 0.5(1 + \tanh((v - 2)/30)) \\ z(y) &= y/(1 + y) \\ \tau(v) &= \cosh((v - 2)/60), \end{aligned} \right\} \quad (1.21)$$

where $g_{ca} = 4.4$, $g_k = 8$, $g_l = 2$, $v_k = -84$, $v_l = -60$, $v_{ca} = 120$, $I = 120$, $g_{kca} = 0.75$, $\Phi = 1.2$, $\varepsilon = 0.04$, and $\mu = 0.016667$.

Note this classification scheme is neither exhaustive nor completely accurate. The naming of classes of bursters depending on the profile of oscillations can get very confusing and subjective. Also labeling the types by numbers as proposed in [11] may prove daunting as well. Yet these preliminary and basic classification schemes make way to more general classification scheme. One such attempt is topological classification we discuss in the following chapter. This classification

schemes takes into account the unique bifurcation features underlying the individual bursting mechanism and the insights from this even leads to the development of minimal models to help treat bursting more analytically.

1.5 Outline of thesis

In this section we briefly summarize the framework of the thesis. The biological examples of bursting neurons are already discussed in this chapter. We also discussed the mathematical properties and models to describe the bursting behaviour of neurons. A classification scheme based on the bursting profile was also presented. In Chapter 2 we discuss a more general classification scheme based on the distinctive dynamical properties of neuronal bursting. This classification is important as this led to the development of the minimal or reduced models for bursting. After some basic discussion on the minimal models we introduce the Bautin elliptic burster model. Our study in thesis is primarily based around the Bautin elliptic burster model with some critical generalizations. We continue our review of bursting neurons to Chapter 3 extending the discussion to coupled bursting systems. In this chapter we discuss a biological example of bursting network related to the rhythmogenesis of the leech heartbeat. After we discuss the synchronization dynamics particular to the bursting systems along with the underlying mechanisms. This discussion is necessary for understanding the peculiarities of coupled bursting systems especially the synchrony changes involving the fast dynamics. Then we present a modified model of a Bautin elliptic burster and present some simulation results demonstrating the synchrony changes in the fast dynamics for two coupled Bautin bursters.

A detailed investigation of the reported phenomenon ‘within-burst synchrony changes’ is carried out in Chapter 4, where the full system for two coupled Bautin bursters with direct linear coupling is reduced to a system of a burst-synchronized constrained model and bifurcation analysis is performed to capture the phenomenon. A theoretical analysis is also carried out to support the observations. Effects of low amplitude noise added to the fast subsystem are also studied. After this, we

consider some examples of more general biologically-motivated coupling producing similar effect in the two coupled bursters.

A cascade of synchrony changes is produced within a synchronized burst for a two coupled Bautin bursters with various modifications to the Bautin burster model in Chapter 5. Bifurcation analysis for such systems is also carried out for corresponding reduced burst-synchronized constrained models. In Chapter 6 the study is extended to higher dimensional systems. Here we present and discuss simulation results of within-burst synchrony changes involving systems of three and four coupled Bautin elliptic bursters.

Within-burst synchrony changes is subject to further study in Chapter 7, where we show simulation results for two coupled Bautin burster producing within-burst synchrony changes property with mutually constant delay coupling. Following this we study a particular example of conductance based biological elliptic burster and show such biological bursters also demonstrate within-burst synchrony changes with mutually delay coupling. Another mechanism generating within-burst synchrony changes in the coupled elliptic bursters is discussed in Chapter 8 in the context of coupled FitzHugh-Rinzel elliptic burster model where an example of a within-burst synchrony change is shown to accompany periodic doubling of the fast subsystem.

In Chapter 9 we study the coupled Hindmarsh-Rose model for square-wave bursting, where the coupled Hindmarsh-Rose neurons with a nonlinear coupling demonstrate clustering properties involving burst synchronization. We analyze the stability of the cluster states by determining the Lyapunov exponents of the corresponding ‘variational’ system for coupled Hindmarsh-Rose neurons about the cluster states. Finally, in Chapter 10 we draw the thesis to a conclusion with broader implications of our research and discuss possible future directions.

Chapter 2

Burst dynamics

In the previous chapter we briefly reviewed some examples of biological bursters and the basic mathematical properties of general bursting models. We also discussed the Rinzel's classification scheme for the bursters. In this chapter we continue to a classification of bursters by Izhikevich based on the distinctive topology associated with different bursting pattern. This classification makes way to a development of minimal models for bursters which we discuss briefly in the chapter. Next we examine a particular example of bursting model known as the Bautin elliptic burster. We discuss the dynamics of a single compartment Bautin elliptic burster and the mechanisms underlying the generation of such bursting.

2.1 Topological classification

Bursting oscillations of neurons have been found to depend more on the type of bifurcations that the fast subsystem undergoes as the slow variable changes rather than on the activity of any specific ionic current in the governing neuronal system [90]. This observation motivated the development of a topological classification for bursters based on the bifurcation properties of the fast variable. This classification scheme is due to the seminal work of Izhikevich and Hoppensteadt [58, 56]. For a comprehensive discussion of the classification scheme, we refer to [59]. In this section, we briefly discuss this classification scheme using the definitions and

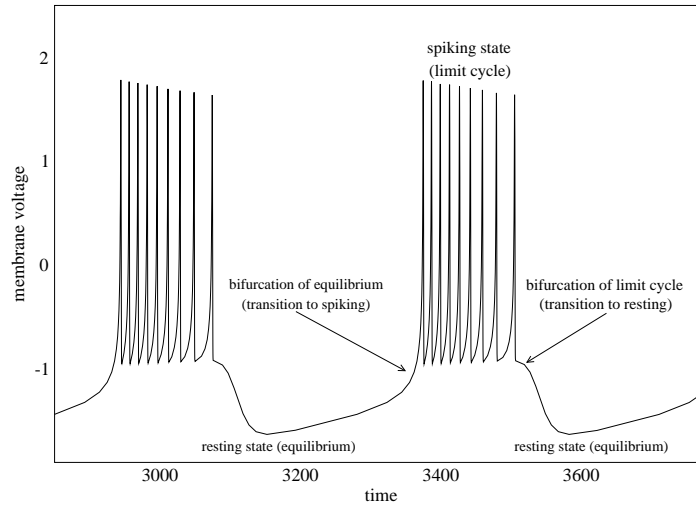


Figure 2.1: Bifurcations at the onset and offset of bursting oscillations.

nomenclature as used by the authors of the scheme. Firstly, in this classification, bursters are distinguished qualitatively according to their topological types, and there are two important bifurcations of the fast subsystem that determine the topological type:

- Resting to spiking: bifurcation of an equilibrium attractor that results in transition from resting to repetitive spiking.
- Spiking to resting: bifurcation of a limit cycle attractor that results in transition from spiking to resting.

A complete topological classification of bursters based on these two bifurcations is provided by Izhikevich [59], who identified 120 different topological types. In this review, we limit our discussion to only ‘planar point-cycle’ codimension-1 bursters. A burster is planar when its fast subsystem is two-dimensional, and point-cycle bursting referred to the slow-fast dynamics characterized by a stable equilibrium as its resting state and a stable limit cycle as its spiking state and a stable limit cycle as its spiking state. Note that bifurcations of codimension-1 need only one parameter and are more encountered in natural systems. Moreover, having a two-dimensional fast subsystem imposes severe restrictions on possible codimension-1 bifurcations of the resting and spiking states. In particular, there are only four

codimension-1 bifurcations of an equilibrium that lead to loss of its stability or its disappearance [65], they are:

- Saddle-node (fold) bifurcation: A stable and an unstable equilibrium coalesce and annihilate each other. The solution leaves a neighbourhood of the equilibria.
- Saddle-node on invariant circle (SNIC) bifurcation: It is similar to a fold bifurcation with an additional condition that it occurs on an invariant circle. Typically, the invariant circle consists of two trajectories connecting the node and the saddle. As the saddle and node coalesce, the small trajectory shrinks and the larger connecting trajectory becomes a homoclinic invariant circle, i.e., originating and terminating at the same point. When the point disappears, the circle becomes a limit cycle. Such a bifurcation results in an oscillation having very large period.
- Supercritical Andronov-Hopf bifurcation: The resting state (equilibrium) loses stability via an Andronov-Hopf bifurcation. The loss of stability is accompanied by the appearance of a stable limit cycle, which is why this is referred to as a supercritical bifurcation.
- Subcritical Andronov-Hopf bifurcation: If a stable equilibrium in the phase space of a system is surrounded by an unstable cycle, then the subcritical Andronov-Hopf bifurcation results when the unstable cycle shrinks to the stable equilibrium and makes it lose stability.

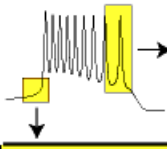
Similarly, there are only four codimension-1 bifurcations of a stable periodic orbit in which the fast variable goes from being active (spiking) state to a resting state (equilibrium) [65], they are:

- Saddle-node on invariant circle (SNIC) bifurcation: A stable limit cycle can disappear via SNIC bifurcation. A stable limit cycle disappears because there is a saddle-node bifurcation that breaks the cycle and gives birth to a pair of equilibria - stable node and unstable saddle. After the bifurcation, the

limit cycle becomes an invariant cycle consisting of a union of two connecting trajectories, namely, saddle-to-node and node-to-saddle. At this bifurcation, the period of oscillation becomes infinite as saddle-node equilibrium appears on the circle.

- Saddle homoclinic orbit bifurcation: The stable periodic orbit or the cycle becomes a homoclinic orbit to saddle equilibrium with infinite period. Note both the saddle homoclinic orbit bifurcation and the SNIC bifurcation involve an equilibrium and a large amplitude homoclinic trajectory that becomes a limit cycle or a stable orbit. The key difference is that equilibrium is a saddle in the saddle homoclinic orbit bifurcation and a saddle-node in the SNIC bifurcation. The saddle equilibrium persists as the bifurcation parameter changes, whereas the saddle-node disappears or bifurcates into two points depending on the direction of change of the bifurcation parameter.
- Supercritical Andronov-Hopf bifurcation: A stable limit cycle shrinks to a point via supercritical Andronov-Hopf bifurcation. As a result, the amplitude of the limit cycle attractor vanishes, and the cycle becomes a stable equilibria. Note, the disappearance of the stable limit cycle is due to the direction of the change in bifurcation parameter is opposite to that results in the appearance of a stable periodic orbit from the equilibrium.
- Fold (saddle-node of) limit cycle bifurcation: In this bifurcation, the stable periodic orbit is approached by an unstable one, they coalesce and annihilate each other. At the point of annihilation, there is a periodic orbit, but it is neither stable nor unstable. More precisely, it is stable from the side corresponding to the stable cycle, and unstable from the other side. This periodic orbit is referred to as a fold limit cycle, and is analogous to the fold (saddle-node) equilibrium. Note when a limit cycle attractor undergoes a fold limit cycle bifurcation, its radius undergoes saddle-node (fold-equilibrium) bifurcation.

bifurcations of limit cycles



| | | saddle-node on invariant circle | saddle homoclinic orbit | supercritical Andronov-Hopf | fold limit cycle |
|----------------------------|---------------------------------|---------------------------------|-------------------------|-----------------------------|--------------------|
| bifurcations of equilibria | saddle-node (fold) | fold/circle | fold/homoclinic | fold/Hopf | fold/fold cycle |
| | saddle-node on invariant circle | circle/circle | circle/homoclinic | circle/Hopf | circle/fold cycle |
| | supercritical Andronov-Hopf | Hopf/circle | Hopf/homoclinic | Hopf/Hopf | Hopf/fold cycle |
| | subcritical Andronov-Hopf | subHopf/circle | subHopf/homoclinic | subHopf/Hopf | subHopf/fold cycle |

Figure 2.2: Topological classification of generic fast-slow bursters having two-dimensional fast (spiking) subsystem (from [56]).

Note any combination of a bifurcation from equilibrium and of a bifurcation from a periodic orbit attractor results in a distinct topological type of burster. Hence, there are 16 such planar point-cycle codimension-1 bursters. The naming of different types of bursters in this scheme is straight forward. The bursters are named according to the types of the bifurcations of the resting and spiking states. To keep the names short, bifurcations with longer names are referred with shorter terms, e.g., saddle-node on invariant circle (SNIC) bifurcation is referred to as only ‘circle’, super(sub)critical Andronov-Hopf bifurcation as ‘super(sub)Hopf’, the fold limit cycle bifurcation as ‘fold cycle’, and the saddle homoclinic as ‘homoclinic’. According to this nomenclature, a ‘fold/homoclinic’ type burster means the transition from rest to spiking in this burster occurs via a fold bifurcation and the transition from spiking to rest occurs via a homoclinic bifurcation. The classical three basic types of bursters discussed earlier may be put under the topological classification based on the bifurcations in their dynamics:

- Square-wave bursting is of ‘fold/homoclinic’ type, because the rest state disappears via a fold bifurcation, and the periodic spiking disappears via a saddle

homoclinic orbit bifurcation.

- In parabolic bursting, the equilibrium corresponding to the resting state disappears via a saddle-node on invariant circle (SNIC) bifurcation, and the limit cycle attractor corresponding to the spiking state disappears via another SNIC bifurcation, so the burster is of the ‘circle/circle’ type.
- Elliptic bursting is ‘subHopf/fold cycle’ type as the resting state loses stability via subcritical Andronov-Hopf bifurcation, and the spiking state disappears via fold limit cycle bifurcation.

One bold aspect of this model is that although not all the types of bursters from this classification scheme have been found in nature, yet the scheme predicts them. We would like to stress that the topological classification of bursters is defined for mathematical models of the slow-fast system of form (1.1) assuming the ratio of time scale, η , is sufficiently small. If a bursting neuron can be described accurately by a model having a slow-fast form like (1.1), then its topological type can be determined just by applying the singular perturbation method, i.e., by freezing the slow subsystem and finding bifurcations of the fast subsystem on treating u as a parameter. Unfortunately, not all neurons can be described adequately by such models, and so the classification scheme renders inadequate in such case. A typical example of the classification failure is the model of bursting of the sensory processing neuron in weakly electric fish, known as the ‘Ghostbursting’ [29], in which $\eta > 0.1$.

Finally to add to this discussion of the topological classification scheme, mathematical studies of bursters revealed that different topological types have different neurocomputational properties [59, 56]:

- Bursters that involve fold, subcritical Andronov-Hopf, saddle homoclinic orbit, and fold limit cycle bifurcations have coexistence of resting and spiking states, and hence exhibit bistability. It implies that all ‘fold/f’ and ‘sub-Hopf/f’ exhibit bistability, at least before the onset of a burst, where ‘f’ denotes any appropriate bifurcation of the spiking state. Similarly, ‘i/homoclinic’

and ‘i/fold cycle’ bursters also exhibit bistability, at least at the end of a burst, where ‘i’ denotes appropriate bifurcation of the equilibrium or resting state. An obvious consequence of bistability is that an appropriate stimulus can switch the system from resting to spiking and back. The input does not even have to be excitatory [59].

- Bursters that involve Andronov-Hopf bifurcation in the quiescent state, so belonging to ‘Hopf/f’ and ‘subHopf/f’ types, act as resonator, i.e., they are sensitive to the frequency content of the synaptic input. Such a burster exhibits damped ‘subthreshold’ oscillations of the membrane potential. If it prefers a certain resonant frequency of the input train that is equal to a low order multiple of its eigenfrequency. Increasing the frequency of the input may delay or even terminates its response.
- In contrast, bursters of type ‘fold/f’ and ‘circle/f’ act as integrators, i.e., they prefer high-frequency inputs, the higher the frequency, sooner the transition to the spiking state. These types of bursters do not have subthreshold oscillations. Integrators can easily encode information about the intensity of stimulation into their mean firing rate. Moreover, integrators distinguish between weak excitatory and inhibitory inputs, unlike resonators.
- Bursters belonging to types ‘Hopf/Hopf’ and ‘subHopf/fold cycle’ bursting show the slow passage effect. The slow passage effect can be shortened significantly by noise or weak input from other bursters.
- Bursters of type ‘fold/f’, ‘fold cycle/f’, and ‘homoclinic/f’ bursting may have a so-called ‘canard’ periodic solution [4], i.e., the fast variable stays near the unstable state for some time before jumping to the limit cycle attractor. The fast variable near the unstable branch is highly susceptible to small perturbation including these coming from other bursters. An excitable spike can make it fire, whereas an inhibitory spike can delay the onset of spiking even further.

Thus, different bursters can communicate, synchronize, and process information differently. However, a pair of distinct bursters can have identical neurocomputational properties [59].

2.2 Minimal bursting models

In this section we discuss development and mathematical analysis of bursting system with reduced or minimal models. Firstly, to understand what is a minimal model of a neuronal system, we may take the following example [56]: let us consider a conductance-based model capable of exhibiting periodic spiking, that is, having a limit cycle attractor. Let us completely remove a current or a gating variable, then see if the reduced model has a limit cycle attractor, at least for some values of parameters. If it does, we remove one gating variable or current, and proceed until we arrive at a model that satisfies the two properties: (a) it has a limit cycle attractor, at least for some values of parameters; (b) if one removes any more current or gating variable, the model has only equilibrium attractors for any value of parameters, i.e., no spiking activity. Such a model is referred to as being minimal or irreducible for spiking. Thus, minimal models can exhibit periodic activity, even if it is of small amplitude, but their reductions cannot. Note according to this definition, any space-clamped conductance-based model of a neuron either is a minimal model or could be reduced to a minimal model or models by removing gating variables. So it is obvious that some well known conductance-based models form a partially ordered set. For example, the chain of neuronal models Morris-Lecar ($I_{Ca} + I_K$) \rightarrow Hodgkin-Huxley ($I_{Na,t} + I_K$) \rightarrow Butera-Rinzel-Smith ($I_{Na,t} + I_K + I_{K,slow}$) is obtained by adding a conductance or gating variable to one model to get the next one. So, following this idea of minimal models, a bursting model is minimal if removal of any current or gating variable eliminates the ability to burst.

One way to build a slow-fast minimal model for bursting is to take a minimal model for spiking, which consists of an amplifying gate and a resonant gate, and add another slow resonant gate, which result in a system of form (1.1). Note that

both the Plant model and the Chay-Keizer model discussed in Chapter 1 belong to minimal models of bursting. Minimal models are appealing because they are relatively simple, each individual variable has an established electrophysiological meaning, and its role in dynamics can easily be identified. It may be shown that many minimal models have subsystems that can be reduced to planar system, which is amenable to analysis using geometrical phase plane methods [56]. So, thinking in terms of minimal models, one can understand what is essential for spiking and bursting and what is not. In the following we briefly discuss the canonical model approach to bursters developed by Hoppensteadt and Izhikevich [51, 59, 56] followed by an in depth review of a reduced model known as Bautin elliptic burster [61]. We study the Bautin system in this thesis in order to understand the synchrony dynamics of coupled bursters.

2.2.1 Canonical models for bursters

In theoretical studies of human brain, it is essential to study families of models instead of one model. It is not possible to know precisely the parameters describing dynamics of a neuron; even if all ionic channels expressed by the neuron are known, the parameters describing their kinetics are usually obtained via averaging over many neurons, there are measurement errors, the parameters change slowly, and so on. Besides, the results can depend on particulars of the underlying model and various models of the same brain structure could produce different results. So, it is more reasonable, from theoretical neuroscience point of view, to consider families of neuronal models having a common property, e.g., the family of all integrators, the family of all resonators, or the family of ‘fold/homoclinic’ bursters, and so on. In fact the canonical model approach is to do with the study behaviour of the entire family of neuronal models if no information about most of its members is known. In another words, a model is canonical for a family of there is a piecewise continuous change of variables that transforms any model from the family into this one. The change of variables does not have to be invertible, so the canonical model is usually lower-dimensional, simple and tractable, yet it would also mean

that we might lose information in return for generality. Nevertheless, it retains many important features of the family, e.g., if the canonical model has multiple attractors, then each member of the family has multiple attractors, likewise if a canonical model has a periodic solution, then each member has at least a periodic solution along with possible quasi-periodic or chaotic solutions, and similarly if the canonical model can burst, so can the each member of the family, and so on. The advantage of this approach is we can study general neurocomputational properties that are shared by all members of the family because all such members can be put into the canonical form by a suitable change of variables. Moreover, it is not actually needed to determine the change of variables, it suffice to prove that such a change of variables exists for the family [51]. In fact, the approach of employing a simplifying change of variables is not new to applications in the life sciences, an example of this can be found in Thom's use of normal form and universal unfolding theories [42].

Now we provide a mathematical description of the canonical models after [51]. Suppose the brain dynamics can be described by a system of differential equations of the form

$$\dot{x} = f(x), \tag{2.1}$$

with $x \in X$, where X is the space of appropriate variables and f is some function. This system (2.1) could be taken as the mathematical model of the brain if its correct space and function are known. Unfortunately, not much known about the system. The standard approach to this problem is to invent a simpler dynamical system, say,

$$\dot{x} = f_1(x), \tag{2.2}$$

with $x \in X_1$. This presumably mimics or illustrates some feature of the brain. But the major drawbacks with (2.2) are that these models do not quite reflect the reality, and the results obtained for them could depend on the model and its function. To cope with this drawbacks we may incorporate more and more data like more ions, channels, and pumps in a neuron's membrane into the model to

lead to another yet more complicated dynamical system, say

$$\dot{x} = f_2(x), \quad (2.3)$$

with $x \in X_2$ and this is apparently more complex than the first earlier one, yet does not reflect all peculiarities of the brain. Thus, the process of refinement is unending. It produces a family of dynamical systems $F = f_k | k = 1, 2, \dots$; and instead of studying each member of F , one may adopt the following approach: let there be a dynamical system

$$\dot{y} = g(y), \quad (2.4)$$

such that any member of F can be converted to this system by a continuous change of variables, so that $h : X \rightarrow Y$, such that if $x(t)$ is a solution of (2.1), then $y(t) = h(x(t))$ is a solution of (2.4). In this case, (2.4) is a factor of (2.1). When h is a homeomorphism (continuous with continuous inverse), dynamical system (2.1) and (2.4) are topologically equivariant. Hence, the dynamical system (2.4) is a canonical model for the family F of dynamical systems if for every member $f_k \in F$ there is a continuous ‘observation’ $h_k : X_k \rightarrow Y$ such that solutions of $\dot{x} = f_k(x)$ are mapped to the solutions of (2.4). Studying the canonical models provide us with information about the behaviour of every member of the family F . We refer to [51] for more detailed discussion on the mathematical aspects of canonical modeling.

A simple example of a canonical model is the phase model $\dot{\theta} = 1$ with $\theta \in \mathbb{S}$, which is a global canonical model for the family of nonlinear oscillators having exponentially stable limit cycle attractors [56]. Also, consider the following canonical models for bursting:

- Under fairly general conditions any slow wave ‘circle/circle’ type or parabolic burster can be transformed to the Ermentrout-Kopell canonical model [34, 35]:

$$\left. \begin{aligned} \dot{\theta} &= 1 - \cos \theta + (1 + \cos \theta)r(\Phi) \\ \dot{\Phi} &= \omega, \end{aligned} \right\} \quad (2.5)$$

where $\theta, \Phi \in \mathbb{S}^1$ are phase variables, indicating the autonomous oscillation of the fast and slow subsystems, respectively, $\omega \approx 0$ is the frequency of the

slow oscillation, and $r : \mathbb{S}^1 \rightarrow \mathbb{R}$ is a periodic function, like $r(\Phi) = \cos \Phi$, that depends on the particulars of the burster, and changes sign and slowly drives the fast neuron in (2.5) back and forth through the bifurcation. When $r(\Phi) < 0$ the cell is quiescent, and when $r(\Phi) > 0$, it fires periodically.

- Another example of a canonical model belongs to the type called ‘fold/homoclinic’ or classically square-wave bursters. Under fairly general conditions on the dynamics of the slow subsystem, the burster can be transformed into the following canonical model [59]:

$$\left. \begin{aligned} \dot{\vartheta} &= 1 - \cos \vartheta + (1 + \cos \vartheta)u \\ \dot{u} &= \mu u, \end{aligned} \right\} \quad (2.6)$$

where, $\vartheta \in \mathbb{S}^1$ and μ is a small parameter. In (2.6), each spike resets to a and decreases u by a constant b , i.e., $\vartheta \rightarrow a$ and $u(t) \rightarrow u(t) - b$ as soon as $\vartheta = \pi$. The canonical model exhibits square-wave bursting for any $0 < a < \pi$, any $b > 0$ and sufficiently small μ .

After a successful canonical model for parabolic burster [34, 35] by Ermentrout and Kopell, Hoppenstedt and Izhikevich went on to derive the canonical model for elliptic burster [59], also known as Bautin burster. In this ‘subHopf/fold cycle’ type bursting, when the two bifurcations occur for nearby values of the slow variable, the fast subsystem is near a Bautin bifurcation. A powerful method of deriving canonical models is based on normal form theory, and it is known that the canonical model for a system near an equilibrium is the topological normal form at the equilibrium [65]. Such a canonical model is local, but it can be extended to describe global dynamics [56].

2.2.2 Normal form

Let a smooth dynamical system be

$$\dot{x} = f(x), \quad (2.7)$$

with $x = (x_1, \dots, x_m) \in \mathbb{R}^m$, for which $x = 0$ is an equilibrium; that is $f(0) = 0$. Let $\lambda_1, \dots, \lambda_m$ be the eigenvalues of the Jacobian matrix $L = Df$ at $x = 0$. For

simplicity, let the eigenvalues be distinct, so that L is diagonal. Each integer-valued relation of the form

$$\lambda_i = n_1\lambda_1 + \cdots + n_m\lambda_m, \quad (2.8)$$

where n_1, \dots, n_m are non-negative integers and $\sum n_j \geq 2$, is called a resonance. With each resonance we can associate a resonant monomial $v_i x_1^{n_1} \cdots x_m^{n_m}$, where $v_i \in \mathbb{R}^m$ is the i th eigenvector of L corresponding to λ_i . The Poincare-Dulac theorem [3] asserts that there is a near identity change of variables $x = y + P(y)$, with $P(y) = 0$, $DP(0) = 0$, that transforms the dynamical system (2.7) to

$$\dot{y} = Ly + W(y), \quad (2.9)$$

where the nonlinear vector function W consists of only resonant monomials. Such a system is called a normal form. In particular, if there are no resonances, then the dynamical system can be transformed to its linearization $\dot{y} = Ly$. It is possible to find a change of variables that removes all nonresonant monomials and transforms the nonlinear system into a simple form [51] – a property desirable for mathematical modeling of the neurons.

2.2.3 Topological normal forms for bifurcations

Topological normal forms provide general bifurcation diagrams for local bifurcations of equilibria and fixed points, i.e., near bifurcation boundaries in the parameter space and corresponding critical orbits in the phase space [65]. This is one of the central notions in bifurcation theory. Sometimes it is possible to construct a simple polynomial system

$$\dot{\xi} = g(\xi, \beta; \sigma), \quad (2.10)$$

with $\xi \in \mathbb{R}^n$, $\beta \in \mathbb{R}^k$, $\sigma \in \mathbb{R}^l$, which is a polynomial in ξ_i and has an equilibrium at $\beta = 0$ satisfying k bifurcation conditions determining a codimension- k bifurcation of this equilibrium, meaning the minimum number of free parameters required to meet a codimension- k bifurcation in a parameter dependent system is exactly equal to k . Here σ is a vector of the coefficients, σ_i , $i = 1, 2, \dots, l$, of the polynomials

involved in (2.10). Together with (2.10) let us consider a system

$$\dot{x} = f(x, \alpha), \quad (2.11)$$

with $x \in \mathbb{R}^n$, and $\alpha \in \mathbb{R}^k$, having at $\alpha = 0$ an equilibrium $x = 0$. System (2.10) is called a topological normal form for the bifurcation if any ‘generic’ system (2.11) with the equilibrium $x = 0$ satisfying the same bifurcation conditions at $\alpha = 0$ is locally topologically equivalent near the origin to (2.10) for some values of the coefficient σ_i . Here, a system like (2.10) is referred to as generic system because the system satisfies a finite number of genericity conditions. Typically, these conditions have the form of inequalities: $N_i(f) \neq 0$, $i = 1, 2, \dots, s$, where each N_i is some algebraic function of certain partial derivative of $f(x, \alpha)$ with respect to x and α evaluated at $(x, \alpha) = (0, 0)$. A detailed discussion of the topological normal forms of different codimension bifurcation can be found in [65]. In this review we only explore the Bautin bifurcation relevant to our research.

2.3 The Bautin bifurcation

The Bautin bifurcation is also known as a generalized or degenerate Andronov-Hopf bifurcation. Bautin bifurcation is a bifurcation of an equilibrium in a two-parameter family of autonomous ordinary differential equations at which the critical equilibrium has a pair of purely imaginary eigenvalues and the first Lyapunov coefficient for the Andronov-Hopf bifurcation vanishes. So, Bautin bifurcation has codimension-2. The bifurcation point separates branches of sub- and supercritical Andronov-Hopf bifurcations in the parameter plane, and for nearby parameter values, the system has two limit cycles which collide and disappear via a saddle-node bifurcation of periodic orbits. Mathematically, let us consider an autonomous system as (2.11) with $x \in \mathbb{R}^n$ and $\alpha \in \mathbb{R}^2$, and smooth f . Suppose, for all sufficiently small α , the system has an equilibrium at $x = 0$, and its Jacobian matrix has one pair of complex eigenvalues: $\lambda_{1,2}(\alpha) = \mu(\alpha) \pm i\omega(\alpha)$, such that $\mu(0) = 0$ and $\omega(0) = \omega_0 > 0$, and the first Lyapunov coefficient for Andronov-Hopf bifurcation is zero. So, the bifurcation is characterized two bifurcation conditions. Generi-

cally, $\alpha = 0$ is the origin in the parameter plane of two branches of Andronov-Hopf bifurcation curve corresponding to the sub- and supercritical cases, and a curve of saddle-node bifurcations of periodic orbits, where two limit cycles collide and disappear. Moreover, this bifurcation is nondegenerate and no other bifurcation occur in a small fixed neighbourhood of $x = 0$ for parameter values sufficiently close to $\alpha = 0$. In this neighbourhood, the system has at most one equilibrium and two limit cycles [3, 65, 42]. Bautin bifurcation can be observed in many neural models, for example, in the Wilson-Cowan oscillator [12].

Any dynamical system at the Bautin bifurcation can be transformed by a suitable continuous change of variables into its topological normal form [59, 56, 61], namely,

$$\dot{z} = (l_0 + i\Omega)z + l_1z|z|^2 + l_2z|z|^4, \quad (2.12)$$

where $z \in \mathbb{C}$ is a complex variable, $\Omega > 0$ is the imaginary part of the complex-conjugate eigenvalue at the Bautin point, and l_0 , l_1 , and l_2 are real parameters. l_1 and l_2 are called first and second Lyapunov coefficients, respectively. The Bautin bifurcation occurs when $l_0 = l_1 = 0$ but $l_2 \neq 0$. When $l_2 < 0$ ($l_2 > 0$), the Bautin bifurcation is said to be supercritical (subcritical) and the limit cycle is stable (unstable). Note (2.12) undergoes Andronov-Hopf bifurcation for $l_0 = 0$, which is supercritical (subcritical) for $l_1 < 0$ ($l_1 > 0$). Moreover, if $l_1 > 0$, then (2.12) undergoes fold limit cycle or saddle-node bifurcation of periodic orbits when $l_1^2 - 4l_0l_2 = 0$. Both Andronov-Hopf and fold limit cycle bifurcations occur simultaneously at the Bautin point $l_0 = l_1 = 0$. In any case, variable z exhibits damped on sustained oscillations with $\Omega > 0$.

2.3.1 Bautin elliptic burster

We present an elliptic bursting model which was called Bautin elliptic burster by Izhikevich[61, 51]. This model which we will present shortly in the following obtained by fixing l_2 in the equation 2.12, so it does not imply unfolding.

Theorem 2.3.1. [65](*Topological normal form for Bautin bifurcation*) *Any generic*

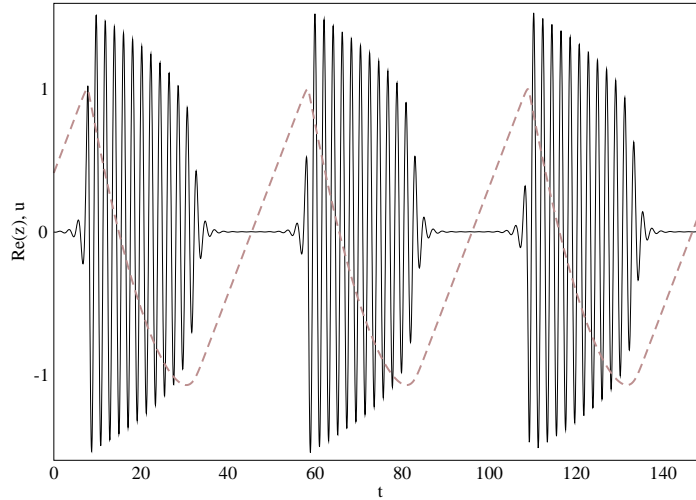


Figure 2.3: The elliptic bursting pattern generated by the system (2.13). The time series plots the real part of z (solid line) and the corresponding slow variable u (broken line). The parameters are $a = 0.8$, $\omega = 3$ and $\eta = 0.1$.

planar two-parameter system

$$\dot{x} = f(x, \alpha),$$

having at $\alpha = 0$ an equilibrium $x = 0$ that exhibits the Bautin bifurcation, is locally topologically equivalent near the origin to one of the following complex normal forms:

$$\dot{z} = (\beta_1 + i)z + 2z|z|^2 \pm z|z|^4.$$

Theorem 2.3.2. [61, 51] Consider $\dot{x} = f(x, y)$ and $\dot{y} = \mu g(x, y)$, $x \in \mathbb{R}^m$ and $y \in \mathbb{R}^k$, having a fast subsystem in an ε -neighbourhood of the Bautin bifurcation point. There is a continuous change of variables that transform all such systems into the canonical model

$$\begin{aligned} z' &= (u + i\omega)z + 2z|z|^2 - z|z|^4 + O(\varepsilon^{\frac{1}{4}}) \\ u' &= \eta(a - |z|^2) + O(\varepsilon^{\frac{1}{4}}), \end{aligned} \tag{2.13}$$

where $\iota = \frac{d}{d\tau}$, $\tau = O(\varepsilon)t$ is slow time, $z \in \mathbb{C}$ and $u \in \mathbb{R}$ are new fast and slow variables, respectively, and $a, \omega \in \mathbb{R}$ and $\eta = O(\mu/\varepsilon^{3/2})$ are parameters.

Non-zero values of $z(t)$ corresponds to periodic spiking of the fast variable $x(t)$ with amplitude of order $\varepsilon^{1/4}|z|$ and ω is the interspike frequency of the system. At

the Bautin point the eigenvalues of the fast subsystem $\dot{x} = f(x, y)$ are $\pm i\omega$. The canonical model (2.13) exhibits bursting when $\eta \ll 1$ and $0 < a < 1$. Tonic spiking sets in for $a > 1$. The co-efficient 2 in the term $2z|z|^2$ ensures that fast subsystem undergoes Andronov-Hopf and fold limit cycle bifurcations for $u = 0$ and $u = -1$, respectively. The particulars of f and g do not affect the form of the canonical model but affect only the radius of parameter η and a . Figure 2.3 demonstrates the elliptic bursting pattern generated by the system (2.13).

The canonical model (2.13) may be written as

$$\left. \begin{aligned} r' &= ur + 2r^3 - r^5 \\ \theta' &= \omega \\ u' &= \eta(a - r^2). \end{aligned} \right\} \quad (2.14)$$

It is obtained by substituting $z = re^{i\theta}$. The phase θ satisfies $\theta' = \omega$, $r = |z|$ denotes the amplitude of oscillation of the fast variable. Non-trivial $r \neq 0$ equilibria of this system correspond to limit cycles of the canonical model, which look like periodic spiking with frequency ω . The non-trivial equilibria of the system (2.14) are $(r_0, u_0) = (\sqrt{a}, a^2 - 2a)$ for all η .

It should be noted that the system (2.14) consists of three differential equations, two of which are dependent and on with θ -variable is independent. $\dot{\theta} = \omega$, gives just rotation of trajectory, while the equations for r and u offer the interesting dynamical behaviours. Now we will discuss the dynamics of the equilibria of the normal form given by equation (2.14). At the equilibria: $r' = 0$, and $u' = 0$, which yields

$$r(u + 2r^2 - r^4) = 0,$$

and $r = \pm\sqrt{a}$.

The non-trivial equilibrium at $(r_0, u_0) = (\sqrt{a}, a^2 - 2a)$. We will discuss the role of the parameters of the system (2.13) by considering more a general form. In what follows, we consider the fast dynamics (or r -dynamics) of the system by setting the slow variable u constant, $r' = f(r, u, \beta)$ and $u = \text{constant}$, where β is the second parameter as the coefficient of the cubic term of the system (2.13). Note that, $\beta = 2$ in the Izhikevich's canonical model (2.13). To obtain the fast subsystem, we

assume $\eta = 0$, i.e., we have frozen the slow dynamics, and the evolution of the fast subsystem is just followed in varying u and β scenario. Hence, the equation for r (fast subsystem) may be written as

$$r' = r(u + \beta r^2 - r^4). \quad (2.15)$$

In order to follow the dynamics of the non-trivial equilibria of the equation (2.15), we write

$$y = u + \beta x - x^2, \quad (2.16)$$

where $r^2 = x$. So, only the positive roots of x are of interest here. The curve of the function (2.16) is a parabola concave downward. In the system described by equation (2.13), the negative sign in the $|z|^4 z$ term signifies similar behaviour. It is obvious that u gives the point of intersection of the parabola with the y -axis ($x = 0$), and changing u shifts the parabola along the y -direction. The slope of the tangent line of this parabola at the point $x = 0$, $dy/dx|_{x=0} = \beta$ is shown in the Figure 2.4. The geometry of this equation (2.16) provides a simple means to discern the phase portrait of the fast subsystem for r described by equation (2.15). It is obvious that the function $r' = r(u + \beta r^2 - r^4)$ is just $y = u + \beta x - x^2$ multiplied by a non-negative number r . This means that if graph of $y = u + \beta x - x^2$ is positive (negative), the graph of $r' = r(u + \beta r^2 - r^4)$ is also positive (negative). Hence, the phase portrait of the dynamics in $r'r^2$ -plane may be implied from the graphical behaviour of the dynamics sketched in xy - plane. Now let us consider a case where $\beta > 0$ and u varies from negative to positive. This situation captures the dynamics of the Bautin elliptic burster. Other situations for different β and u are also admissible and give different dynamics.

The dynamics in the xy -plane and $r'r^2$ -plane are shown in the Figure 2.5. Here β is held constant to a positive value, so the function $y = u + \beta x - x^2$ has positive slope at $x = 0$. To begin with, we vary u from positive to negative. So, when $u > 0$ as shown in the Figure 2.5a, along the y -axis there is a positive intercept of an amount u , and a crossing through abscissa which implies the existence of an equilibrium of the dynamics. More precisely, in the codimension-2 case, these y -intercept and x -intersection points Figure 2.5b correspond to an unstable equilibrium and a stable

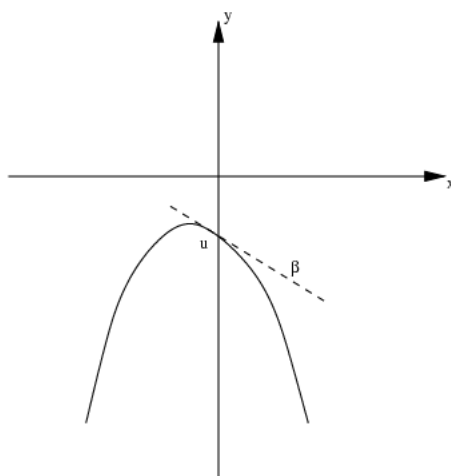


Figure 2.4: The parabolic shape of the function $y = u + \beta x - x^2$. The intercept, u , on the y -axis and the tangent, β , at $x = 0$ are also shown.

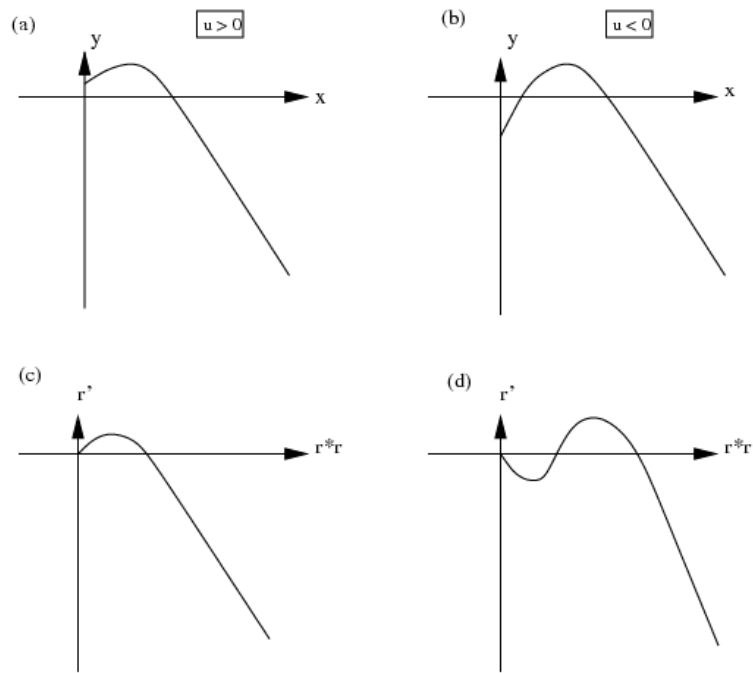


Figure 2.5: The dynamics of the equilibria governed by (2.15) and (2.16) as u is changed from negative to positive while keeping β constant and positive. In the panels (a) and (b), y against $x = r^2$ is shown, while in (c) and (d), $r' = ry$ is shown against r^2 .

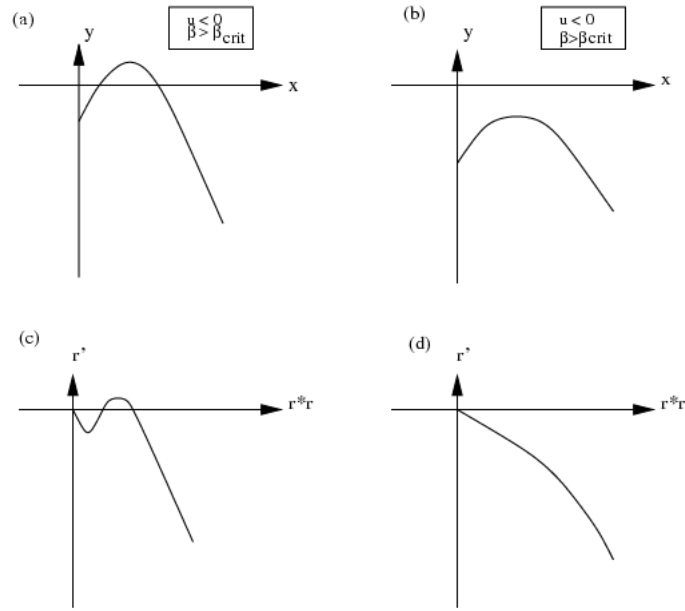


Figure 2.6: The dynamics of the equilibria governed by (2.15) and (2.16) as β is changed from $\beta > \beta_{crit}$ (a.c) to $\beta < \beta_{crit}$. In the panel (a) and (b), dynamics of xy are shown, and in (c) and (d) the corresponding phasespaces are displayed.

limit cycle with nonzero r , respectively.

Now, as u decreases, the graph of the function $y = u + \beta x - x^2$ shifts downward, and at $u = 0$, another point of $y = 0$ occurs. This shows the emergence of a bifurcation point, where we see an unstable equilibrium in the case of $u > 0$ becomes stable, and two other intersections in x -axis represent two limit cycles: one stable and another one unstable. In Figure 2.5c, this case is displayed at $u < 0$, and Figure 2.5d shows the dynamics in $r'r^2$ -plane. This may be interpreted as a subcritical Andronov-Hopf bifurcation.

Interesting dynamics may be observed if β is decreased. With decreasing β the slope of the function $y = u + \beta x - x^2$ flattens, and the two equilibria move closer. At a certain critical value of $\beta (= \beta_{crit})$ the two equilibria, corresponding to two stable an unstable limit cycles, coalesce, and for $\beta > \beta_{crit}$ the limit cycles disappears following the annihilation of the equilibria leaving only one stable equilibrium.

This bifurcation scenario is known as saddle-node bifurcation of limit cycles (see Figure 2.6). In order to find the line of the saddle-node bifurcation of the limit cycles, we determine the non-trivial solution of equation (2.14), which yields

$$r_{1,2}^2 = \frac{1}{2}(\beta \pm \sqrt{\beta^2 + 4u}).$$

During fold (saddle-node) bifurcation of limit cycles, both stable and unstable limit cycles coalesce which implies

$$\begin{aligned} \beta^2 + 4u &= 0 \\ \Rightarrow \beta &= \pm\sqrt{-4u}, \end{aligned} \tag{2.17}$$

and $r_{1,2}^2 = \frac{\beta}{2}$. Since, $r_{1,2}^2$ must be positive, $\beta > 0$, so the saddle-node bifurcation of limit cycles takes place at the upper left gradient of the $u\beta$ -plane. The bifurcation line this plane is parabolic trajectory given by equation (2.17) as shown in the figure (2.7). $\beta > 0$ implies $\beta = \sqrt{4u}$ with $u < 0$. So, as u is decreased from positive to negative value (Figure 2.7), it hits on the curve of the saddle-node bifurcation of limit cycles in the upper-left quadrant and the systems settles to a stable fixed point.

In the case of the system (2.13), the value for β is chosen to be 2, so it follows from equation (2.17) that $u = -1$. Hence, the onset of the repetitive firing takes place via a sub-critical Andronov-Hopf bifurcation at $u = 0$, while the steady state is reached via saddle-node bifurcation of limit cycles at $u = -1$, for the system (2.13). Figure 2.7 demonstrates the bifurcation points leading to the bursting pattern governed by the system (2.13). One important feature of the system (2.13) as can be seen in its polar version (2.14) that the frequency of the periodic spiking is independent of the amplitude ('isochronous') and is a constant; in the following chapter we present a 'non-isochronous' form of the Bautin bursting model where the frequency of the spike depends on the amplitude of the fast oscillations.

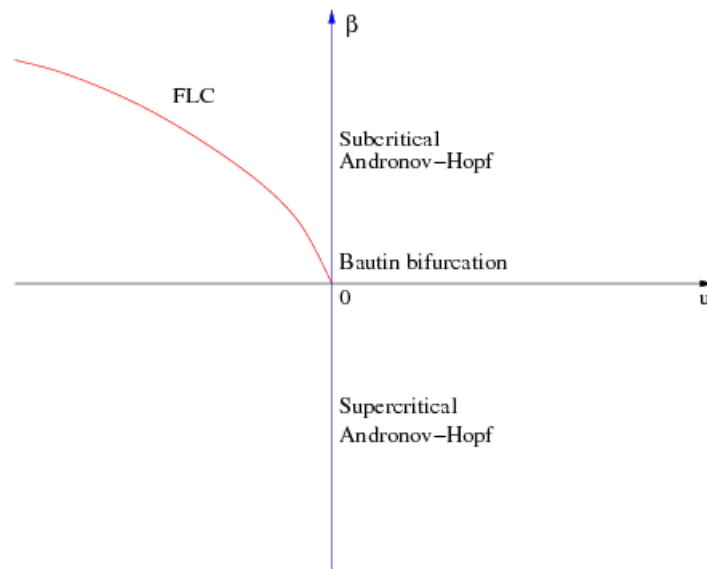


Figure 2.7: The curve of $\beta = \sqrt{4u}$ (FLC) in $u\beta$ -plane. This curve shows the locality of the fold (saddle-node) bifurcation of limit cycles in the co-dimension plane. Sub- and supercritical Andronov-Hopf bifurcation and Bautin bifurcation are shown.

2.4 Delayed bursting: slow passage effect

A prominent feature of ‘subHopf/fold cycle’ type or elliptic bursting, as we mentioned earlier, is that the transition from resting to spiking does not occur at the bifurcation of the equilibrium state, rather the fast subsystem remains at the unstable equilibrium for quite some time before jumping to the spiking state. This phenomenon is known as slow passage effect, or ramp effect, or memory effect, or delayed loss of stability [56, 59]. It is ubiquitous in simulations of smooth dynamical systems near subcritical or supercritical Andronov-Hopf bifurcations. This phenomenon was discovered by Fenichel [37] Shishkova [101]. The mechanism of slow passage effect or delayed loss of stability is following: the state of the system is attracted to the stable focus before the bifurcation. Even though the focus loses stability at the bifurcation, the state is infinitesimally close to the equilibrium, so it can take a long time to diverge from there. The longer it takes to converge to the equilibrium, longer it takes to diverge from it, hence the noticeable delay. In slow-fast bursting such as (1.1) involving Andronov-Hopf bifurcation of the fast subsystem, solutions stay close to the equilibrium or quiescent state as the $O(\eta)$ -slow variable passes through a threshold where linear stability is lost. Subsequently, after a substantial $O(1)$ delay, solutions jump away from the equilibrium. This effect has been studied by many authors [95, 114, 115, 116, 77, 78, 61]. The delay in slow passage through an Andronov-Hopf bifurcation is generically more significant for systems that are analytic in complex time, as shown by Shiskova [101] and Neishtadt [77, 78]. When a system can be reduced to a homogeneous system, the delay can be attributed to a simple contraction of solutions, but in general, more conditions are required for a delay. Moreover, the amount of delay is determined by many factors, such as nearby singularities, if external forcing is present, and the difference between intrinsic and forcing frequencies [116]. Baer et al. [95] observed that the delay is greater if the initial point is further from the bifurcation point. They also derived a new stability condition by perturbation method for small η , which is $\int_0^\tau Re[\lambda(s)]ds < 0$, where τ is the time of the slowly varying solution with respect to the fast time t , and λ denotes the eigenvalue of the largest real part.

The authors showed that the integral condition implies a memory effect and it applies over a robust parameter range in which the time scale of the characteristic frequency is $O(1)$ associated with Andronov-Hopf bifurcation. The importance of this integral condition for predicting the delay was also reported for bursting solutions [95].

This delay is sensitive to small amplitude noise and to periodic environmental perturbations of near resonant frequency. When noise is added, numerical computations and asymptotic methods [116] suggest that the amount of delay is significantly reduced or even advanced (‘advanced loss of stability’) because noise perturbs the trajectory to escape the attractor earlier than it does. These results clarify why delay is not always observed in experiments of biological neurons which always contain noise, despite the fact that it is often present in simulations. In Chapter 5 we dwell on the presence of a slow passage effect and the effect of noise in the context of coupled Bautin burster system.

Chapter 3

Coupled neuronal bursters

In this chapter we discuss biology and dynamics of coupled-burster systems. Multiplicity of time scale and multidimensionality are at the origin of complexities in coupled-burster systems, which results in many interesting types of synchrony dynamics. Typical to the slow-fast rhythms of the bursters, the synchrony behaviour possess two aspects: ‘burst synchronization’ and ‘spike synchronization’ corresponding to synchronization of slow and fast subsystem dynamics, respectively. What follows in the discussion of this chapter is a brief review of a biological model of the leech heart interneurons which show bursting rhythms with interesting synchrony behaviour which underlies the generation and control of the heartbeat rhythm of the leech. Following this biological example we discuss the burst and spike synchrony types of coupled bursters and their underlying mechanisms. Next we discuss a more particular example of coupled bursting system involving Bautin elliptic bursters with non-isochronous phase dynamics and show a novel synchrony dynamics involving the fast subsystem for two coupled Bautin bursters.

3.1 The leech heart interneuron model

A well studied example of a functional network of neurons that generates bursting is the leech heart interneuron circuit. In the leech, blood is propelled through the circulatory system to all of leech’s individual body segments by the rhythmic con-

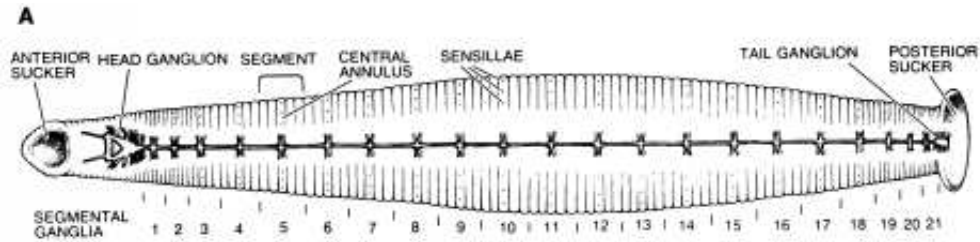


Figure 3.1: The leech nervous system with 21 ganglia (from [64]).

strictions of two lateral heart tubes. Figure 3.1 shows a sketch of the nervous system of a leech. The timing and coordination of these constrictions are controlled by a central pattern generator [74, 80]. Central pattern generators (CPGs) are neuronal networks that can endogenously (without rhythmic sensory or central input) produce rhythmic patterned outputs; these networks underlie the production of most rhythmic motor patterns [68, 109]. The leech heart CPG comprises a network of seven bilateral pairs of segmental heart interneurons. The CPG produces rhythmic activity at about 0.1 Hz that paces segmental heart motor neurons, which in turn drive the two hearts. This network can be divided into two subsets [74, 80, 68]:

- The rhythm generator: produces the pattern's basic rhythm.
- The pattern generator: generates the actual motor pattern in response to driving input from the rhythm generator.

The rhythm generator circuit contains four pairs of heart interneurons. Figure 3.2 shows a schematic diagram of the rhythm generator circuit and the synaptic connectivity among the neurons. The synaptic connections among the interneurons and from the interneurons to the motor neurons are inhibitory. It is clear from Figure 3.2 that the network consists of four bilaterally symmetrical neuron pairs. The right and left '3' and '4' neurons inhibit each other, and on each side '1' and '2' are reciprocally inhibitory with neurons '3' and '4', the network thus forms a ring of reciprocally inhibitory neuron pairs. This four pairs of heart interneurons control the timing of the network and the timing oscillation is dominated by the activity of the '3' and '4' neurons of the network. Figure 3.3(A) shows simultaneous intracellular recordings from right and left neurons '3' indicated as (R,3) and (L,3), respectively.

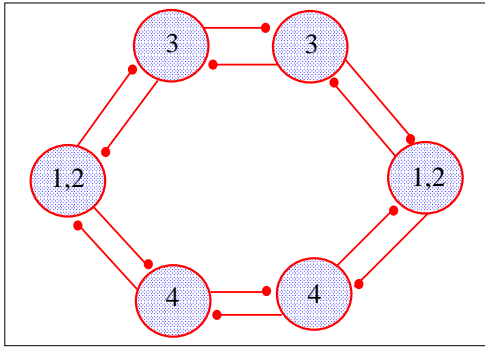


Figure 3.2: Sketch of the leech heartbeat rhythm-generating network.

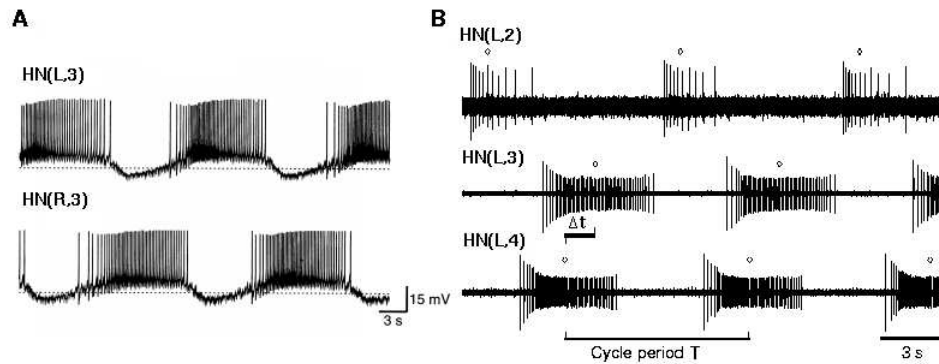


Figure 3.3: (A) shows a simultaneous intracellular recordings of the elemental oscillator consisting of left and right heart interneuron indicated by (L,3) and (R,3), respectively, in ganglion 3. (B) shows extracellular recordings from three left heart interneurons indicated as (L,2), (L,3) and (L,4); Note that the cells (L,3) and (L,4) fire approximately inphase and both of these cells fire approximately antiphase with cell (L,2) (from [74, 80]).

It is apparent that they rhythmically fire bursts of action potentials precisely out of phase (antiphase). The recordings in Figure 3.3 (B) shows that neurons ‘3’ and ‘4’ on the right ((L,3) and (L,4), respectively) fire approximately inphase to an experimental error and both of these neurons fire approximately out of phase with left neuron ‘2’ (indicated as (L,2)). According to [74, 80] further recordings show (not shown here) that the ‘3’ and ‘4’ neurons on one side fire inphase bursts with the ‘1’ and ‘2’ neurons on the other side. The network thus produces a two-phase rhythm. When released from synaptic inhibition, these neurons exhibit tonic firing but do not show bursting activity [62].

Key to understanding rhythm generation in the leech heart interneuron network is the concept of a half-centre oscillator. In small circuit of coupled spiking neurons, such as two mutually inhibitory oscillators, alternating bursting can appear, known as a half-centre oscillator, suggested by Brown [13]. In this network, while one cell fires, the other is inhibited, then they switch roles, and so on. Activity within a half-centre oscillator consists of alternating bursts of action potentials and quiescent intervals. Half-centre oscillators are thought to be building blocks of CPGs in the pyloric network of the lobster stomatogastric ganglion, fictive motor patterns and swimming patterns of many vertebrates and invertebrates [67]. Figure 3.4 shows a sketch of a half-centre network consisted of two cells. To explain the alternation patterns of burst and quiescent of the neurons, Wang, Rinzel [122] and Skinner [102] suggested four mechanisms of release and escape:

- In intrinsic release, the active cell stops spiking, terminates inhibition and allows the inhibited cell to fire.
- In intrinsic escape mechanism, the inhibited cell recovers, starts to fire and shuts off the active cell.
- In synaptic release mechanism, the inhibition weakens and allows the inhibited cell to fire.
- In synaptic escape mechanism, the inhibited cell depolarizes above a certain threshold and starts to inhibit the active cell.

Note all four mechanisms assume that in addition to fast variables responsible for spiking, there are slow variables responsible for termination of spiking, recovery or synaptic depression (weakening of the inhibition). Thus, the circuit is a slow-fast system.

In the leech heart, the rhythm generator circuit containing neuron pairs ‘3’ and ‘4’ are half-centre oscillators (Figure 3.2) and because of their reciprocally inhibitory synapses the pairs ‘3’ and ‘4’ neurons produce bursting oscillations. particularly, the mechanism of oscillation for reciprocally inhibitory neuron pair ‘4’ shown Figure 3.2 may be explained as following: say the right neuron fires

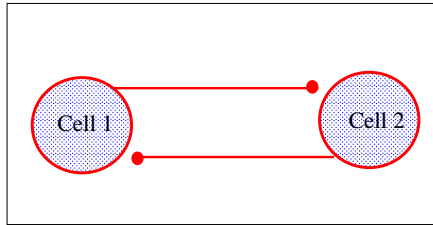


Figure 3.4: A half-centre oscillator. The filled circles at the end of the links indicate inhibitory connection.

and thus inhibits the left neuron, but also induces a slow depolarization in it, and eventually the left neuron reaches spike threshold and begins to fire. Firing in the left neuron inhibits and stops the right neuron from firing, but again also induces a slow depolarization in it. The right neuron therefore eventually begins to fire and the cycle repeats. The rhythmogenesis in the leech heartbeat rhythm generator arises from the interplay of these ‘elemental’ half-centre oscillators, which may be described as following: each neuron pair of the neurons ‘3’ and ‘4’ forms a functional half-centre in which two neuron burst in antiphase. Neurons ‘1’ and ‘2’ reciprocally inhibit the ipsilateral ‘3’ and ‘4’ neurons, and hence the only stable mode of bursting for the neurons of one side is for the ‘3’ and ‘4’ neurons burst together and inphase with neurons ‘1’ and ‘2’; this results in the entire network having the activity shown in Figure 3.3. The neurons ‘3’ and ‘4’ half-centre oscillators form the rhythmic heart of the network, and ‘1’ and ‘2’ neurons coordinate the activity of these two half-centre oscillator [68]. This process is now understood on the conductance level of the neurons [80]. The leech heart interneuron model shows the rhythm generated by burst synchrony dynamics which control the heart beat. This review is important as a motivation to study the synchrony properties of the bursters. In this thesis we focus mostly on the synchrony behaviour of the fast spikes and we address the burst synchrony behaviour in Chapter 9 for a particular neuronal bursting model. In the following section we discuss the aspects and dynamics of synchronization of coupled-burster systems.

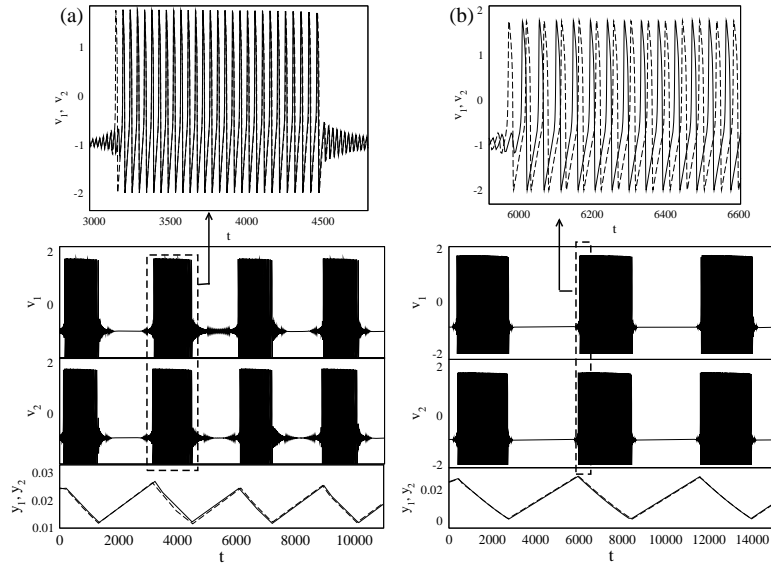


Figure 3.5: Distinguishing burst and spike synchronization in two coupled FitzHugh-Rinzel bursters (8.2). In both cases the system is burst synchronized, but (left) the excitatory coupling renders inphase spikes and (right) inhibitory gives antiphase spikes.

3.2 Synchronization of coupled bursters

Before we study the example of coupled Bautin elliptic bursters, we discuss briefly some general aspects of synchrony dynamics systems of coupled bursters. There are two rhythmic processes associated with bursting, one is repetitive spiking (fast activity) and repetitive bursting (slow modulation). Therefore, there could be at least two different regimes of synchronization — synchronization of individual spikes and synchronization of bursts. Note that one of them does not imply the other and there is an additional regime where both types of synchronization occur simultaneously. It has been observed that whether a pair of bursters could synchronize depends on the burster types [60]. In the following we discuss the spike and burst synchronization of coupled bursters and the mechanism leading to such synchronization.

3.2.1 Burst synchronization

The mechanism of stable burst synchronization dynamics of bursters can be understood from an example of two planar point-cycle burster: one is in the active

(spiking) state and the other still in the quiescent state. If the active burster makes the quiescent burster jump from the quiescent state prematurely, then the pair may exhibit burst synchronization. If it prolongs the quiescent state, then the inphase burst synchronization cannot be stable, but other regimes such as antiphase burst synchronization may be stable [59]. Dynamics of burst synchronization of weakly coupled bursters is similar in some aspects to that of strongly coupled relaxation oscillators [52]. Analyses of coupled bursters show that there are two mechanisms leading to burst synchronization. One is fast threshold modulation (FTM) [56, 59, 61] and the other is the destruction of the slow passage effect. Also, stable burst synchronization depends on whether the quiescent burster is an integrator or a resonator; for example, if a bursting neuron is a resonator, then both excitation and inhibition may lead to burst synchronization [56, 59]. In the followings we briefly discuss the outlined mechanisms leading to burst synchronization and burst synchrony behaviour of bursting neurons depending on particular neurocomputational properties.

Fast threshold modulation

The mechanism by which one cell fires, and thereby causes the other cell to fire, is referred to as fast threshold modulation (FTM). It was first discussed in the context of strongly coupled relaxation oscillator in [105, 106]. Burst synchronization with threshold modulation was discussed in [59, 93]. A simple enumeration of the mechanism is: let there be two ‘fold/homoclinic’ or square-wave bursters labeled as A and B, respectively. Burster A is slightly ahead of burster B, so that A starts the spiking phase while B is still resting. If the synaptic connections between the bursters are excitatory, firing A causes B to jump to the spiking state prematurely, because according to FTM the rate of change of slow variable before the jump is less than that after the jump. This premature jumping of B to follow A shortens the time difference between the bursters. In addition, the evoked burst of B is shorter, which also speeds up the synchronization, this results in stable burst synchronization. In contrast, when the connections are inhibitory, firing A delays the

transition of B to the spiking state, thereby increasing the time difference between the bursts and desynchronizing the bursters. This illustrates the principle of ‘excitation means synchronization’ and ‘inhibition means desynchronization’, which is discussed in [93] for the square-wave burster.

Burst synchronization via slow passage effect

To understand how burst synchronization can be achieved via a slow passage effect, we consider an example: let there be two coupled ‘subHopf/fold cycle’-type bursters, labeled as A and B, respectively. Note that bursters of this topological type have a slow passage effect at the on-set and off-set of the burst. Now, suppose A is slightly ahead of B, i.e., they have essentially different values of slow variables. Let by the time A starts to fire B is well in the zone of the slow passage effect. Since the slow passage effect is sensitive to perturbation and it can be shortened significantly by weak input from other bursters, firing A destroys the effect and elicits an almost instantaneous response from burster B. Thus, instantaneous burst synchronization occurs between the bursters. This mechanism leads to instantaneous inphase burst synchronization of the bursters even when they have essentially different spike frequencies. In [61] a discussion of instantaneous burst synchronization via slow passage effect can be found involving coupled Bautin elliptic bursters.

Burst synchronization and neurocomputational properties of bursters

The mechanism of burst synchronization depends on the topological types of bursting, more specifically it depends on whether the resting state is an integrator or a resonator. If a point-cycle bursting occurs via ‘fold/f’ hysteresis loop, then the burster acts as an integrator: while the slow variable is near the bifurcation value, the fast variable is ready to jump up in response to incoming pulses from the active burster. Similar behaviour can be seen in the bursting of ‘circle/f’ or ‘Hopf/f’ type. In any case the jump shortens the quiescent phase and eventually synchronization follows from the rule ‘excitation means synchronization’ and ‘inhibition means desynchronization’. Similarly, if point-cycle bursting occurs via ‘subHopf/f’

hysteresis loop, then the burster acts as a resonator in the quiescent state. Such a burster exhibits damped subthreshold oscillations of the membrane potential. If the frequency of the incoming pulses is resonant with the frequency of the subthreshold oscillation, then both excitation and inhibition may evoke premature spiking, this may result in stable inphase burst synchronization. If the input pulse is not resonant, the quiescent state is not affected.

3.3 Spike synchronization

Spike synchronization involves the fast time scale. So, the intuitive approach to study spike synchronization of bursters is to neglect the slow variable dynamics. To illustrate the method mathematically, let us consider two bursting neurons coupled weakly through their fast variables:

$$\dot{x}_i = f(x_i, u_i) + K_i(x_i, x_j, \varepsilon) \quad (3.1)$$

$$\dot{u}_i = \eta g(x_i, u_i), \quad (3.2)$$

with $i \neq j$, and $i, j = 1, 2$. K_i represents the coupling with ε as coupling strength. To study synchronization of individual spikes within the burst, consider $\eta = 0$ in order to freeze the slow subsystem (3.2), and consider the fast subsystem (3.1) describing weakly coupled oscillator characterized by small ε . When $u_i \approx u_j$, the fast variables oscillates with approximately equal period, so (3.1) can be reduced to the phase model:

$$\dot{\theta} = \varepsilon H(\theta_j - \theta_i, u_i), \quad (3.3)$$

with $u_i = \text{constant}$ which parameterizes the form of the connection function. For example, during ‘circle/Hopf’ burst, the function is transformed from $H(X) = \sin^2 X$ or $1 - \cos X$ at the beginning of the burst to $H(X) = \sin X$ at the end of the burst [56], changing u_i slowly one can study when spike synchronization appears and when it disappears during the burst. A necessary condition for synchronization for two weakly coupled oscillators is that they have nearly equal frequencies [61].

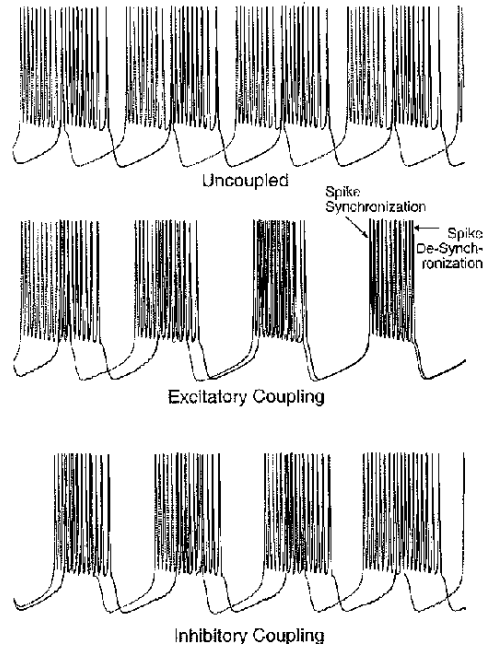


Figure 3.6: Example of (middle) transition of spikes from inphase synchronization to asynchronization towards the end of the burst in coupled Morris-Lecar square-wave bursters with an additional slow variable (from [59]).

The ‘nearness’ depends on the strength of coupling. Thus, synchronization of individual spikes within a single burst depends crucially on the interspike frequencies, which may vary substantially during a burst. Indeed, a small perturbation of the slow variable may result in large perturbations of the interspike frequency, hence such a burster would be unlikely to exhibit spike synchronization unless the coupling is strong [56]. Spike synchronization may occur during the entire duration of a burst, or during the initial or the final stage of the burst as observed in [59]. Spike synchronization during the initial stage of the burst usually does not occur between ‘circle/f’ bursters because the interspike frequency changes substantially during the initial stage and small deviation in the value of the slow variables may lead to drastic variance in the frequencies. The other types of burster tend to have regular spiking during the initial stage of a burst. Therefore, they could exhibit spike synchronization. However, convergence to the synchronized state takes as many as $O(1/\varepsilon)$ spikes, and can be longer than the entire initial stage [59]. Similarly, ‘i/circle’ type bursters do not usually exhibit spike synchronization during

the final stage of the burst. In Figure 3.6 an example of coupled ‘fold/homoclinic’ (square wave) bursters is shown where the last few spikes were shown to desynchronize as the sudden drop in the interspike frequency occurs during the last few spikes. In what follows we explore similar “within burst synchrony changes” behaviour in a particular example of coupled Bautin elliptic bursters with nonisochronicity, i.e., where the instantaneous frequency of the spikes undergoes transition during the burst.

3.4 Coupled Bautin bursters

Elliptic bursting in a neuronal system is a type of recurrent alternation between active phases (large amplitude oscillations) and quiescent phases (small amplitude oscillations). This kind of rhythmic pattern can be found in rodent trigeminal neurons [76], thalamic relay and reticularis neurons [25, 27], the primary afferent neurons in the brain stem circuits [81], and neurons in many other areas of the brain. It is clearly of interest for neuronal population information encoding and transmission where several bursters fire within a population. Patterns of synchrony of elliptic bursters may also be helpful in understanding firing patterns in more general types of burster [23, 41, 56, 90].

In a previous study of the synchronization of elliptic bursters, Izhikevich examined a pair of coupled ‘normal form’ elliptic bursters [61] characterized by slow passage through a Bautin (codimension two Andronov-Hopf) bifurcation. In that study, burst (slow activity pattern) synchronization between the bursters was found to be easily achievable, whereas spike (fast activity pattern) synchronization was harder to achieve. Other studies include [30] who have examined nonlinearly coupled Bautin bifurcations, though not in a bursting setting and [59, 34, 96] who have looked at various aspects of burst and spike synchronization for a variety of coupled burster models.

In this section we study the potential that spike synchronization for coupled Bautin-type elliptic bursters show more complicated phase (spiking) dynamics. We show that higher order terms that are not important in the normal form of a

single burster can be responsible for nontrivial phase dynamics in coupled bursters even for linear coupling. In particular, we observe and explain coexistence of and transitions between inphase and antiphase spiking within a single burst for two and more coupled bursters. This sheds light onto possible dynamical patterns of spike synchronization for coupled bursters in neuronal systems.

We discuss a normal form for coupled Bautin-type elliptic bursters and focus on burst and spike synchronization in a system of n identical coupled bursters with $z_j \in \mathbb{C}$, $u_j \in \mathbb{R}$ and $j = 1, \dots, n$ given by

$$\left. \begin{aligned} \dot{z}_j &= (u_j + i\omega) z_j + B z_j |z_j|^2 + C z_j |z_j|^4 + K_j \\ \dot{u}_j &= \eta(a - |z_j|)^2, \end{aligned} \right\} \quad (3.4)$$

where $\omega, a, \eta \in \mathbb{R}$ and $B = B_r + iB_i, C = C_r + iC_i \in \mathbb{C}$ are fixed parameters, K_j represents coupling. We assume $B_r > 0$ and $C_r < 0$, and set

$$B = 2 + i\zeta = 2 + i\frac{\sigma r^2}{2}, \quad C = -1 + i\gamma = -1 - i\frac{\sigma}{4}. \quad (3.5)$$

We assume that the coupling term is

$$K_j = (\kappa_1 + i\kappa_2) \sum_{k=1}^n c_{jk} z_k, \quad (3.6)$$

where $\kappa_1, \kappa_2 \in \mathcal{R}$ are constant coupling parameters and c_{jk} a constant connectivity matrix. For convenience here we take $c_{jk} = 1$ for $j \neq k$, $c_{jj} = 0$; i.e. all-to-all coupling. Biologically, although there are no rigorous reductions of specific bursters to this model, one can think of $z = x + iy$ as a fast variable x that is analogous membrane voltage, y that is analogous to the fast current, and a slow variable u analogous to a slow adaptation current for a neuronal burster.

3.5 The model for coupled Bautin bursters

Bursting is a multiple time scale phenomenon. In bursting, the fast dynamics of repetitive spiking is modulated by a slow dynamics of recurrent alternation between active and quiescent states. As explained in [56] one may obtain bursting from a variety of dynamical mechanisms; here we focus on bursters (3.4, 3.5, 3.6) with

bursting behaviour associated with a Bautin bifurcation (Section 2.3); we briefly review the single burster dynamics. After this we discuss the spike and burst synchronization for two coupled bursters.

Suppose we have a Bautin bifurcation, namely a codimension two Andronov-Hopf bifurcation where the criticality changes on varying an additional parameter. Then as discussed in Section 2.3 there is a normal form that is locally topologically equivalent to the bifurcation, and the equation 2.12 may be recast as following for $z = x + iy \in \mathbb{C}$

$$\dot{z} = Az + Bz|z|^2 + Cz|z|^4 + O(|z|^6), \quad (3.7)$$

where $A = A_r + iA_i$; B , and C are real coefficients. One can verify that an Andronov-Hopf bifurcation occurs as A_r passes through 0 and a change of criticality occurs where B also passes through zero. The fourth order term is needed to determine the criticality at the degenerate point $B = 0$. We consider a more general ordinary differential equation where B and C are complex; we write B and C as in (3.5). It can be shown that ζ, γ and $O(|z|^6)$ terms do not affect the local branching dynamics of the system (3.7). We will however argue that ζ and γ may influence the synchrony for two or more coupled elliptic bursters.

From (3.7) we obtain bursting dynamics [59, 61, 56] by coupling the system to a slow variable $u \in \mathbb{R}$ that is the Andronov-Hopf parameter for the Bautin normal form, such that for z small u increases, while for z large u decreases:

$$\left. \begin{aligned} \dot{z} &= (u + i\omega)z + (2 + i\zeta)z|z|^2 + (-1 + i\gamma)z|z|^4 \\ \dot{u} &= \eta(a - |z|^2). \end{aligned} \right\} \quad (3.8)$$

Note that $\eta \ll 1$ is the ratio of the fast to slow time scales. The system (3.8) exhibits bursting for $0 < a < 1$ while tonic spiking sets in for $a > 1$.

In polar form, $z = re^{i\theta}$, (3.8) becomes

$$\left. \begin{aligned} \dot{r} &= ur + 2r^3 - r^5 \\ \dot{\theta} &= \omega + \zeta r^2 + \gamma r^4 \\ \dot{u} &= \eta(a - r^2). \end{aligned} \right\} \quad (3.9)$$

In these coordinates it is clear that the fast subsystem undergoes an Andronov-Hopf bifurcation at $u = 0$ and a limit cycle fold bifurcation (a saddle-node of

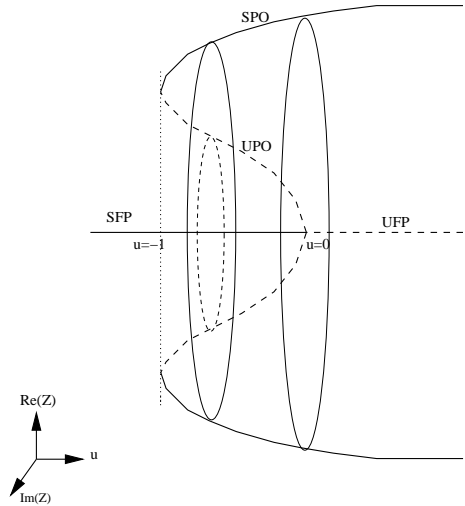


Figure 3.7: Schematic bifurcation diagram for z for the fast subsystem of (3.8) on varying u . SFP denotes the stable fixed point, UFP unstable fixed point, SPO stable periodic orbit and UPO unstable periodic orbit. It is clearly seen that at $u = 0$, the system undergoes subcritical Andronov-Hopf bifurcation, while saddle node bifurcation of limit cycles occur at $u = -1$.

limit cycles) at $u = -1$. At the saddle-node bifurcation of limit cycles, stable and unstable limit cycles coalesce. A bifurcation sketch for the system (3.8) is shown in the Figure 3.7. It is clear from this figure that periodic firing appears at a subcritical Andronov-Hopf bifurcation at $u = 0$ with the emergence of a limit cycle. Likewise the steady state is reached via a saddle-node bifurcation of limit cycles at $u = -1$, where the stable limit cycle (solid line) meets the unstable limit cycle (dashed line) and eventually cancel each other at $u = -1$.

Note that during bursts, if $\zeta, \gamma \neq 0$ the limit cycles are ‘non-isochronous’; there is a change in frequency of the fast oscillation during the bursts. As this non-isochronicity does not affect the r or u dynamics, and hence the branching behaviour, it is not important for single bursters. The phase dynamics in (3.9) depends on amplitude r :

$$\dot{\theta} = \Omega(r) = \omega + \zeta r^2 + \gamma r^4. \quad (3.10)$$

The non-trivial periodic orbits of the system (3.9) are $(r_0, u_0) = (\sqrt{a}, a^2 - 2a)$ for $\eta = 0$. Non-trivial periodic orbits, $r \neq 0$ correspond to periodic orbits of (3.8)

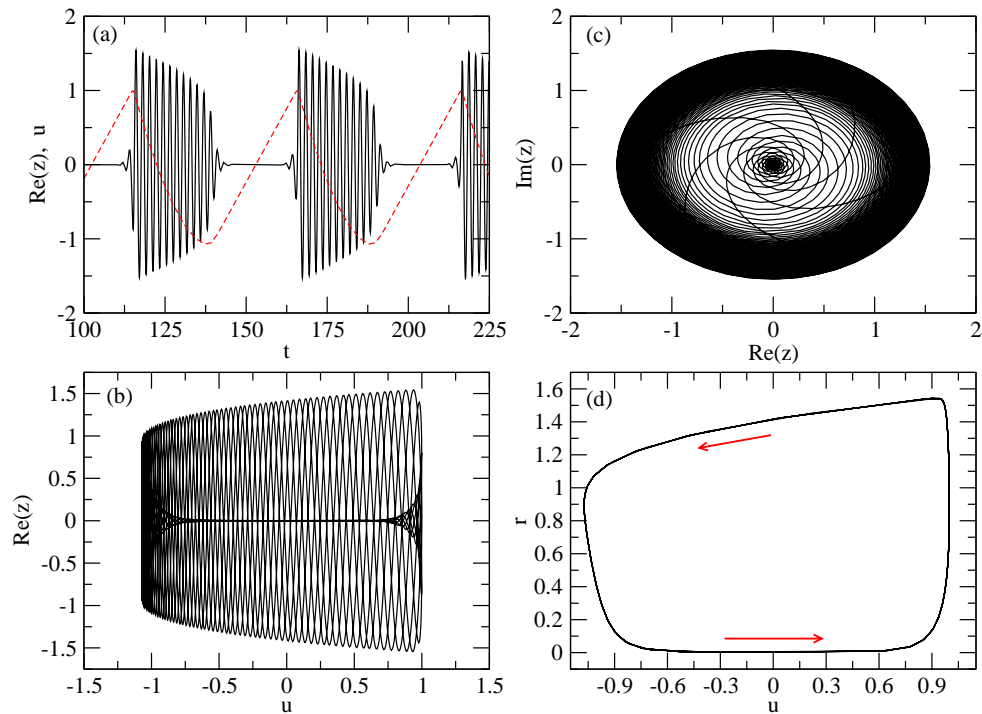


Figure 3.8: Dynamics of a single compartment Bautin Burster governed by (3.8) and (3.11). In panel (a), the timeseries of $Re(z)$ is shown with solid line and the corresponding slow variable, u , with dashed line. The parameters for the simulation are $\omega = 3$, $a = 0.8$, $\eta = 0.1$, $\sigma = 4$, and $r_m = 1.35$. The arrows in (d) indicates the direction of change of the slow variable, u .

with periodic spiking. The dynamics of the (3.8) is summarized in figure 3.8 for parameters $\omega = 3$, $\eta = 0.1$, $a = 0.8$, $\alpha = 2$, $\beta = -1$, $\zeta = 0$, and $\gamma = 0$. Observe the slow passage effect [95] apparent from Figure 3.8; although the stability calculation shows the Andronov-Hopf bifurcation occurs at $u = 0$, but simulation shows a delayed bifurcation [95].

Note that we use parameters in (3.5) such that

$$\zeta = \frac{\sigma r_m^2}{2}, \quad \gamma = -\frac{\sigma}{4}, \quad (3.11)$$

meaning that

$$\frac{d\Omega}{dr} = \sigma r(r_m^2 - r^2). \quad (3.12)$$

From this it is clear that there is a turning point of $\Omega(r)$ at $r = r_m$. The parameter σ can be interpreted as the magnitude of non-isochronicity for the phase dynamics.

We consider direct linear coupling for the system (3.8) via the fast variables z to give a coupled system of the form (3.4, 3.6) with coupling parameters κ_1 and κ_2 , in Section 4.2.2 we considered other types of coupling. The coefficients c_{jk} for the coupling term of (3.4) are the connectivity matrix; here we assume all-to-all coupling, namely

$$c_{jk} = \begin{cases} 1 & \text{if } j \neq k \\ 0 & \text{otherwise} . \end{cases}$$

This form of coupling is analogous to the electrical (gap junction) coupling between synapses with phase shift expressed by the argument of $\kappa_1 + i\kappa_2$. Positive κ_1 corresponds to excitatory coupling, while negative κ_1 corresponds to inhibitory coupling.

3.5.1 Burst and spike synchronization for two coupled bursters

We numerically investigate the dynamics of a pair of coupled elliptic bursters governed by the system (3.4). Burst synchronization between the cells can be easily achieved for a wide range of parameter values with this system. In case of $\kappa_2 = 0$ and $\kappa_1 > 0$ (excitatory coupling), this generally generates inphase bursts, while

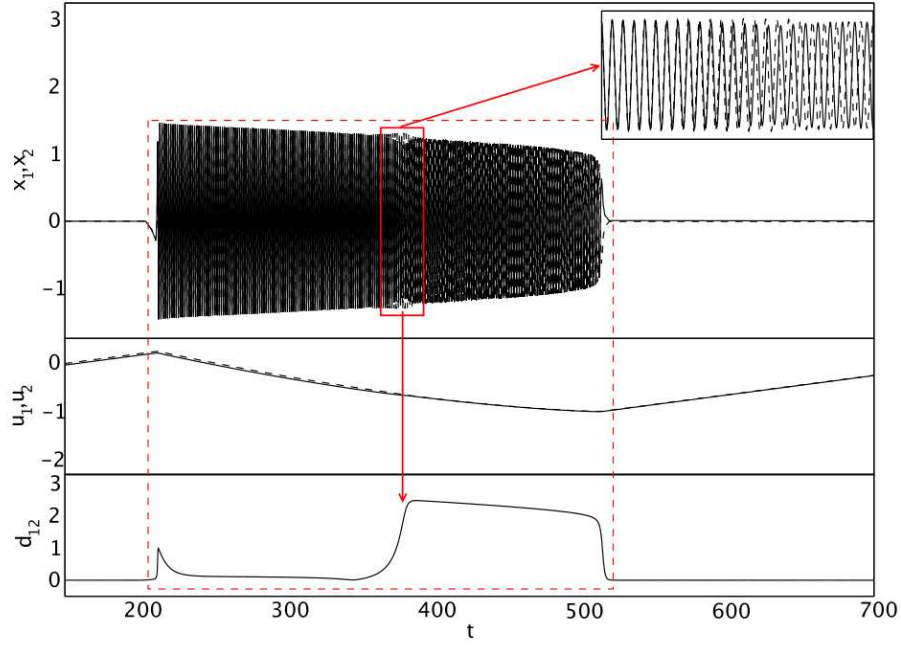


Figure 3.9: Within-burst synchrony change from stable inphase to stable antiphase states for two coupled bursters. The dashed box shows the activity pattern of one burst and the burst repeats periodically and within-burst synchrony change repeats during each burst. This result is obtained from simulation of (3.4), (3.5) and (3.6) for $n = 2$, and parameters $\kappa_1 = 0.001$, $\kappa_2 = 0.2$, $\sigma = 3$, $\eta = 0.005$, $r_m = 1.35$, $\omega = 0.01$. Noise of amplitude 10^{-5} was added to the fast subsystem. In this figure, the two coupled bursters are burst synchronized and the spikes become inphase at the beginning of the burst, but changes to antiphase near the middle of the burst. The inset in the topmost panel shows the region of the transition. Note that the initial transient and sudden change in the synchrony pattern along the burst profile are observable from d_{12} , where $d_{12} = 0$ indicates inphase synchronization.

antiphase bursts result from inhibitory coupling.¹

There is a spontaneous ‘within-burst synchrony change’ observable within fig-

¹We write the system (3.4) using $z_1 = x_1 + iy_1$ and $z_2 = x_2 + iy_2$ for the purposes of numerical simulation. All the simulations were done with the interactive package XPPAUT [33]. For integrations, the built-in adaptive Runge-Kutta integrator was used, and results were checked using the adaptive Dormand-Prince integrator.

ure 3.9. The top panel shows x_1 and x_2 . All transients were allowed to decay and the displayed pattern is repeated within each burst. A detail of the middle of the burst is shown in the top-right inset. The corresponding slow variables of the system, u_1 and u_2 , are shown in the middle panel. The distinguishing solid and dashed traces correspond to the activity patterns of the two cells, respectively. The bottom shows the Euclidean distance

$$d_{12} = \sqrt{(x_1 - x_2)^2 + (y_1 - y_2)^2 + (u_1 - u_2)^2}$$

between the two systems to show the presence ($d_{12} = 0$) or absence ($d_{12} > 0$) of synchrony. The values of the parameters used in the simulation are $\kappa_1 = 0.001$, $\kappa_2 = 0.2$, $\sigma = 3$, $\eta = 0.005$, $r_m = 1.35$, $\omega = 0.01$. Wiener noise of amplitude 10^{-5} was added to the fast variables (see Section 4.2.1 for a discussion of the effect of noise).

The spikes are inphase at the beginning of the burst, but change to antiphase within the burst. The inset shows the region of this transition. This transition region may be shifted along the burst profile on changing r_m . Larger values of r_m shift this transition towards the beginning of the burst with larger amplitude spikes, and vice versa. This change in the synchrony pattern along the burst profile is also captured by d_{12} .

We present another example of within-burst synchrony change for different parameter values in figure 3.10, where spikes of the two coupled cells start antiphase and change to inphase during the burst. The parameters for this are $\kappa_1 = 0.001$, $\kappa_2 = -0.2$, $\eta = 0.05$, $\sigma = 3$, and $r_m = 1.35$. As before, low amplitude noise of order 10^{-5} was added to fast variables. The inset in the first panel shows the region of the transition. In the last panel, d_{12} indicates that the burst is initially antiphase, and as it returns to $d_{12} = 0$ there is a transition to inphase synchronization of the within-burst spikes of the two cells. The corresponding slowly changing current variables, u_1 and u_2 , are shown in the middle panel. The overlapped solid and dashed lines imply the inphase burst synchronization of the coupled system.

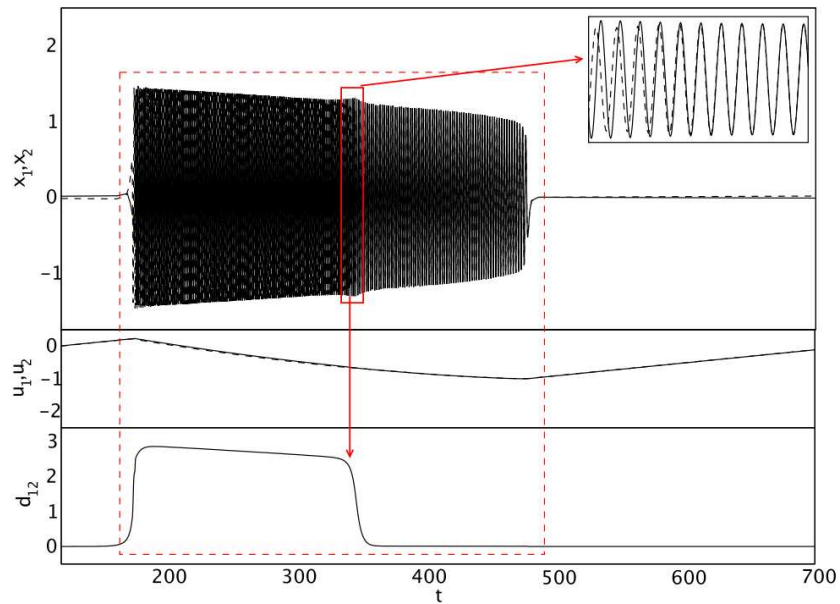


Figure 3.10: Within-burst synchrony change from stable antiphase to stable inphase states. The governing system and details as in figure 3.9 except $\kappa_2 = -0.2$. The inset in the topmost panel shows the transition in detail. In the last panel, the bump in d_{12} signifies the antiphase synchronization of the spikes within the synchronized burst. The corresponding slowly changing variables, u_1 and u_2 , are shown in the middle panel with solid and dotted lines, respectively.

Chapter 4

Analysis of within-burst synchrony changes

In Section 5.1 of the previous chapter we reported ‘within-burst synchrony changes’ for two directly coupled Bautin bursters governed by the system (3.4, 3.5, 3.6), where the fast spikes undergo spontaneous synchrony changes over a burst period. The analysis of the phenomenon is the goal of this chapter, which is done with a reduced model obtained by forcing the the fast subsystem of the both bursters with same slow variable. We also examine effect of low amplitude noise added to the fast subsystem on the synchrony dynamics. After we study the coupled system incorporating more general biologically-motivated coupling with a aim to observe similar effect.

4.1 A burst-synchronized constrained model

Although it is possible to find within-burst synchrony changes within (3.4, 3.5, 3.6), it is hard to explain their existence analytically from the full model. To overcome this, we reduce the coupled system to a constrained problem where we assume burst synchronization, followed by a slow-fast decomposition. Using this we can explain how non-isochronicity and linear coupling can lead to within-burst synchrony changes.

4.1.1 Two coupled bursters in polar coordinates

Writing (3.4, 3.5, 3.6) in polar coordinates $z_j = r_j e^{i\theta_j}$ for $n = 2$ gives the system

$$\left. \begin{aligned} \dot{r}_1 &= u_1 r_1 + 2r_1^3 - r_1^5 + r_2(\kappa_1 \cos(\theta_2 - \theta_1) - \kappa_2 \sin(\theta_2 - \theta_1)) \\ \dot{\theta}_1 &= \omega + \frac{1}{2}\sigma r_m^2 r_1^2 - \frac{1}{4}\sigma r_1^4 + \frac{r_2}{r_1}(\kappa_1 \sin(\theta_2 - \theta_1) + \kappa_2 \cos(\theta_2 - \theta_1)) \\ \dot{u}_1 &= \eta(a - r_1^2) \\ \dot{r}_2 &= u_2 r_2 + 2r_2^3 - r_2^5 + r_1(\kappa_1 \cos(\theta_1 - \theta_2) - \kappa_2 \sin(\theta_1 - \theta_2)) \\ \dot{\theta}_2 &= \omega + \frac{1}{2}\sigma r_m^2 r_2^2 - \frac{1}{4}\sigma r_2^4 + \frac{r_1}{r_2}(\kappa_1 \sin(\theta_1 - \theta_2) + \kappa_2 \cos(\theta_1 - \theta_2)) \\ \dot{u}_2 &= \eta(a - r_2^2). \end{aligned} \right\} \quad (4.1)$$

We constrain the system to exact burst synchronization by replacing the equations for \dot{u}_1 and \dot{u}_2 by

$$\left. \begin{aligned} u(t) &= u_1(t) = u_2(t) \\ \dot{u} &= \dot{u}_1 = \dot{u}_2 = \eta \left(a - \frac{1}{2}(|z_1|^2 + |z_2|^2) \right). \end{aligned} \right\} \quad (4.2)$$

Thus, the system (4.1) may be written with constraint (4.2) and $\phi = \theta_1 - \theta_2$ as

$$\left. \begin{aligned} \dot{r}_1 &= u r_1 + 2r_1^3 - r_1^5 + \kappa_1 r_2 \cos \phi + \kappa_2 r_2 \sin \phi \\ \dot{r}_2 &= u r_2 + 2r_2^3 - r_2^5 + \kappa_1 r_1 \cos \phi - \kappa_2 r_1 \sin \phi \\ \dot{\phi} &= \frac{1}{2}\sigma r_m^2 (r_1^2 - r_2^2) - \frac{1}{4}\sigma (r_1^4 - r_2^4) \\ &\quad - \kappa_1 \left(\frac{r_1^2 + r_2^2}{r_1 r_2} \right) \sin \phi - \kappa_2 \left(\frac{r_1^2 - r_2^2}{r_1 r_2} \right) \cos \phi \\ \dot{u} &= \eta \left(a - \frac{1}{2}(r_1^2 + r_2^2) \right). \end{aligned} \right\} \quad (4.3)$$

As we are interested in synchrony changes, we define longitudinal and transverse coordinates

$$\left. \begin{aligned} r_l &= (r_1 + r_2)/2 \\ r_t &= (r_1 - r_2)/2. \end{aligned} \right\} \quad (4.4)$$

The system (4.1) reduces to the four dimensional system

$$\left. \begin{aligned}
 \dot{r}_l &= ur_l + 2r_l^3 + 6r_l r_t^2 - r_l^5 - 10r_l^3 r_t^2 - 5r_l r_t^4 \\
 &\quad + \kappa_1 r_l \cos \phi - \kappa_2 r_t \sin \phi \\
 \dot{r}_t &= ur_t + 6r_l^2 r_t + 2r_t^3 - 5r_l^4 r_t - 10r_l^2 r_t^3 - r_t^5 \\
 &\quad - \kappa_1 r_t \cos \phi + \kappa_2 r_l \sin \phi \\
 \dot{\phi} &= 2\sigma r_m^2 r_l r_t - 2\sigma r_l r_t (r_l^2 + r_t^2) \\
 &\quad - 2\kappa_1 \frac{(r_l^2 + r_t^2)}{r_l^2 - r_t^2} \sin \phi - 4\kappa_2 \frac{r_l r_t}{r_l^2 - r_t^2} \cos \phi \\
 \dot{u} &= \eta(a - (r_l^2 + r_t^2)).
 \end{aligned} \right\} \quad (4.5)$$

Here, (r_l, r_t, ϕ) govern the fast dynamics, and u governs the slow dynamics. The system (4.5) is a reduced four-dimensional realization of the full system (4.1) for a pair of coupled elliptic bursters. Figure 4.1 shows a bifurcation diagram for the fast subsystem of (4.3) on varying u . The dashed loop indicates how a periodic burst including a within-burst synchrony change can occur: we define an observable R_d^2 by

$$R_d^2 = r_1^2 + r_2^2 + \frac{1}{4}r_1 r_2 \cos \phi. \quad (4.6)$$

Note that R_d is such that $R_d = \frac{9}{4}r$ if the oscillations are inphase and $R_d = \frac{7}{4}r$ if they are antiphase, and $r_1 = r_2 = r$. It is also symmetric under interchange of the bursters. In [98] antiphase, asymmetric or quasiperiodic spike synchrony patterns have been reported from a system of two of gap-junction-coupled pancreatic β -cells. They attributed this to bifurcations on the periodic branches of the fast subsystem for a similarly burst constrained system.

4.1.2 Stability analysis of the burst constrained system

In this section, we carry out a linear stability analysis of the fast sub-system of (4.5) about inphase and antiphase states with $r_t = 0$ and $r_l = r$, which means both cells are burst synchronized and $r_1 = r_2 = r$. In the analysis, we assume the slow variable u is a constant of the system by setting the time scale ratio, $\eta = 0$, as a

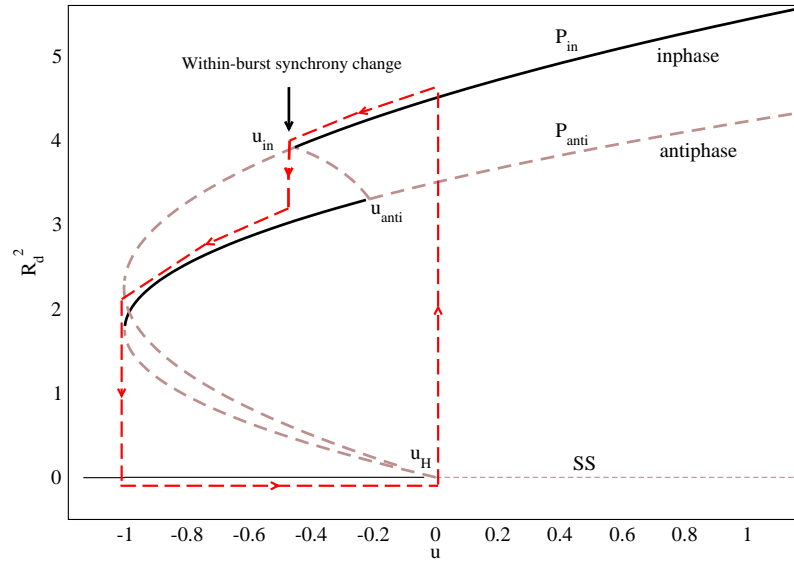


Figure 4.1: Bifurcation of the fast dynamics for the coupled constrained system (4.3), plotting R_d^2 against u (see (4.6)) and parameters as in figure 3.9. The branches P_{in} and P_{anti} are the inphase and antiphase periodic branches of the system. The steady state branch is denoted by SS. Solid and dashed parts of the branches denote the stable and unstable solutions, respectively. u_{in} and u_{anti} are bifurcations giving loss of stability of the inphase and antiphase periodic orbits respectively, while u_H is the Andronov-Hopf bifurcation of SS. The dashed loop indicates how the slow dynamics generates periodic bursts. Note the switching of the trajectory from inphase to antiphase along the periodic branches implies a within-burst synchrony change.

singularly perturbed parameter. The dynamics, as a result, is only governed by the fast spiking activity. For $r_t = 0$ and $\eta = 0$ we write $r_l = r$ as the stable nontrivial solution of (4.5) in the appropriate subspace

$$\dot{r}_l = (u + 2\kappa_1 \cos \phi)r_l + 2r_l^3 - r_l^5 \quad (4.7)$$

corresponding to bursting behaviour. Note that for small $|\kappa_1|$, this will have a solution close to the single burster case.

If we consider the fast subsystem of (4.5) with u between -1 and +1 then one can verify the existence of two solutions

- Inphase where $r_t = \phi = 0$, $r_l = r$,
- Antiphase where $r_t = 0$, $\phi = \pi$, $r_l = r$,

where $r > 0$ is a solution of

$$u = r^4 - 2r^2 - 2\kappa_1 \cos \phi. \quad (4.8)$$

The Jacobian for the fast subsystem at the inphase solution is block diagonal with one single real eigenvalue and a block

$$J_{in} = \begin{pmatrix} u + 6r^2 - 5r^4 - \kappa_1 & \kappa_2 r \\ 2\sigma r_m^2 r - 2\sigma r^3 - \frac{4\kappa_2}{r} & -2\kappa_1 \end{pmatrix}. \quad (4.9)$$

Likewise, the Jacobian for the fast system at the antiphase solution is also block diagonal with a single real eigenvalue and a block

$$J_{anti} = \begin{pmatrix} u + 6r^2 - 5r^4 + \kappa_1 & -\kappa_2 r \\ 2\sigma r_m^2 r - 2\sigma r^3 + \frac{4\kappa_2}{r} & 2\kappa_1 \end{pmatrix}. \quad (4.10)$$

Note that the off-diagonal entries of the Jacobian matrices (4.9) and (4.10) depend on the imaginary part of the coupling coefficient, κ_2 , and other system parameters. The real eigenvalues can be assumed negative because of stability of the solution of (4.7).

The eigenvalues of (4.9) can be determined by examining the trace

$$tr(J_{in}) = u + 6r^2 - 5r^4 - 3\kappa_1 \quad (4.11)$$

and the determinant

$$\det(J_{in}) = -2(u + 6r^2 - 5r^4)\kappa_1 - 2\sigma r^2(r_m^2 - r^2)\kappa_2 + 2\kappa_1^2 + 4\kappa_2^2. \quad (4.12)$$

Similarly, we can understand their antiphase counterparts from (4.10) by examining

$$\text{tr}(J_{anti}) = u + 6r^2 - 5r^4 + 3\kappa_1 \quad (4.13)$$

and

$$\det(J_{anti}) = 2(u + 6r^2 - 5r^4)\kappa_1 + 2\sigma r^2(r_m^2 - r^2)\kappa_2 + 2\kappa_1^2 + 4\kappa_2^2. \quad (4.14)$$

For simplicity, we consider a special case when $\kappa_1 = 0$ and $|\kappa_2| \ll 1$. In such a case, it may easily be seen that both $\text{tr}(J_{in})$ and $\text{tr}(J_{anti})$ in (4.11) and (4.13), respectively, are negative, as stability of the periodic solution of (4.7) means that $u + 6r^2 - 5r^4 < 0$. So, from (4.11) and (4.13), $\text{tr}(J_{in}) < 0$, and $\text{tr}(J_{anti}) < 0$. For this weak coupling, it is also evident that $(\text{tr}(J_{in(anti)}))^2 > 4\det(J_{in(anti)})$. Hence, the system will have a stable node for $\det(J_{in(anti)}) > 0$ and a saddle for $\det(J_{in(anti)}) < 0$.

To explain the within-burst synchrony change observed in figures 3.9 and 3.10, we write (4.12) and (4.14) to first order in κ_2 , we approximate $\kappa_1 = 0$ and consider small $\kappa_2 > 0$, gives

$$\det(J_{in}) = -2\sigma r^2(r_m^2 - r^2)\kappa_2 + O(\kappa_2^2) \quad (4.15)$$

and

$$\det(J_{anti}) = 2\sigma r^2(r_m^2 - r^2)\kappa_2 + O(\kappa_2^2). \quad (4.16)$$

From equation (5.15), if $r > r_m + O(\kappa_2)$, then $\det(J_{in}) > 0$. Together with the condition $\text{tr}(J_{in}) < 0$, this implies that the inphase solution is stable, whereas (4.16) implies that the antiphase solution is unstable for $r < r_m + O(\kappa_2)$. We may derive approximate expressions for $r(= r_l)$ where the bifurcations take place. We denote the bifurcation value for amplitude of the inphase solution by r_{in} , and the amplitude of the antiphase solution by r_{anti} . Note that r_{in} may be obtained by equating $\det(J_{in})$ to zero in the equation (4.12) with $\kappa_1 = 0$ giving

$$\det(J_{in}) = -\kappa_2(2\sigma r_{in}^2 - 2\sigma r_{in}^2 r_m^2 - 4\kappa_2) = 0. \quad (4.17)$$

Now solving (4.17) gives

$$r_{in} = r_m \left(1 - \frac{\kappa_2}{\sigma r_m^4}\right) + O(\kappa_2^2). \quad (4.18)$$

Likewise, from equation (4.14), the bifurcation point, r_{anti} , may be obtained as

$$r_{anti} = r_m \left(1 + \frac{\kappa_2}{\sigma r_m^4}\right) + O(\kappa_2^2). \quad (4.19)$$

Note that r depends on u via (4.8). So, the corresponding bifurcation points for in(anti)phase oscillations can be derived from (4.18, 4.19) and (4.8) for the special case $\kappa_1 = 0$ as

$$u_{in} = r_m^2(r_m^2 - 2) + \frac{4\kappa_2}{\sigma r_m^2}(1 - r_m^2) + O(\kappa_2^2), \quad (4.20)$$

and

$$u_{anti} = r_m^2(r_m^2 - 2) - \frac{4\kappa_2}{\sigma r_m^2}(1 - r_m^2) + O(\kappa_2^2). \quad (4.21)$$

Note that a more general analysis of these bifurcation points for non-zero κ_1 and κ_2 can be undertaken by examining roots of (4.12, 4.14).

4.1.3 Synchrony bifurcations of the fast subsystem

We now extend the numerical bifurcation analyses of the fast subsystem (4.3) from figure 4.1 by taking η as the singular perturbation parameter to take the fast system through single bursts and to compare with the asymptotic results found for $\kappa_1 = 0$.

We present in figure 4.2 bifurcations of bursting solutions of (4.3) projected onto the phase difference, ϕ , as u is varied. The solid line represents the stable periodic solutions, while the unstable solutions are shown with dash-dotted lines. The arrow, running from right to left, shows the direction of the change of u . What figure 4.2(a) shows is a burst that begins with stable inphase solution, and till almost half way through the burst, the inphase solution remains stable and then the antiphase solutions gain stability. The coupling coefficients in this results are $\kappa_1 = 0.001$ and $\kappa_2 = 0.2$. The other parameter values are $\sigma = 3$, $\omega = 3$, and $r_m = 1.35$. This behaviour agrees with the simulation result shown in the figure 3.9 and figure 4.1, both obtained for the same parameters. Similarly, figure 4.2(c) explains what is found in the simulation in figure 3.10. Here, the burst starts off

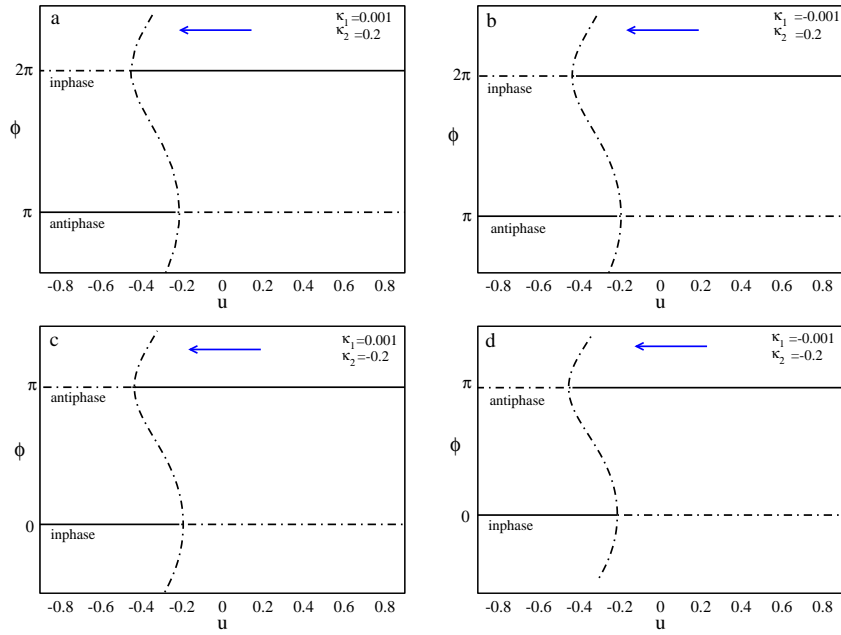


Figure 4.2: Bifurcation diagram of ϕ against u for the burst-synchronized constrained system (4.3), where u is a parameter that slowly decreases during each burst as shown by the arrow. The parameters are $\omega = 3$, $\sigma = 3$, $r_m = 1.35$, and different κ_1 and κ_2 as indicated in the panels from (a) to (d). Note (a) corresponds to the parameters in figure 3.9 and 4.1 and (c) to that in figure 3.10. The solid lines represent stable solutions, while the unstable solutions are shown with dash-dotted lines.

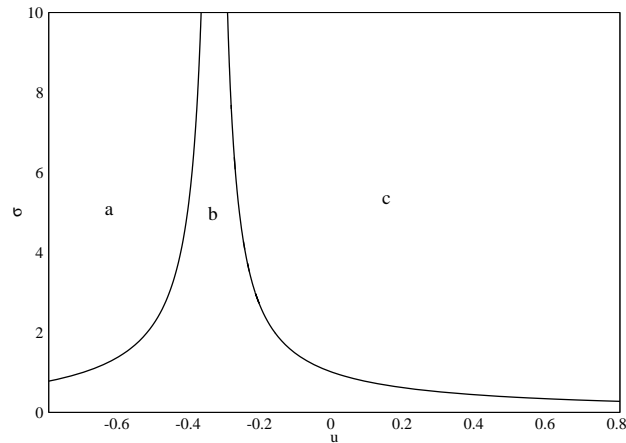


Figure 4.3: Two parameter bifurcation diagram of σ against u for the fast subsystem of (4.3). The other parameters are fixed at $\kappa_1 = 0.001$, $\kappa_2 = 0.2$, and $r_m = 1.35$. There are stable inphase oscillations in region b,c, and stable antiphase oscillations in region a,b.

in stable antiphase and changes to stable inphase. Figure 4.2(b) and (d) show the results with $\kappa_1 = -0.001$ but different κ_2 . An interesting observation is the presence of the bistable region around the middle of the burst separating the stable inphase and antiphase solutions. This region occurs near the transition point ($r_m = 1.35$) along the burst profile as predicted in the analysis in the previous section. These bifurcations show the robust coexistence of the inphase and antiphase synchrony patterns of the within burst spikes for a range of u , and within-burst synchrony changes of the coupled bursting system (3.4).

Figure 4.3 shows a two-parameter bifurcation diagram in the $u\sigma$ plane. As σ increases, the bistable region is seen to get narrower, in agreement with (4.18, 4.19). Likewise, figure 4.4 is obtained from parameters: $\kappa_1 = 0.001$, $\kappa_2 = 0.2$, and $\sigma = 3$. This figure shows how the position of the bistable region ‘b’ changes on varying r_m .

The role of the coupling parameter κ_1 is shown in figures 4.5 and 4.6 for two values of κ_2 . The parameters in figure 4.5 are $\kappa_2 = 0.2$, $\sigma = 3$, and $r_m = 1.35$ and the behaviour is similar to figure 4.2(a) and (b). It is interesting to note that within-burst synchrony changes appear even for weak inhibitory coupling ($\kappa_1 < 0$). Moreover, stronger inhibitory values of κ_1 would mean only antiphase spike synchronization. Similarly, figure 4.6 demonstrates similar dynamics to figure 4.2(c)

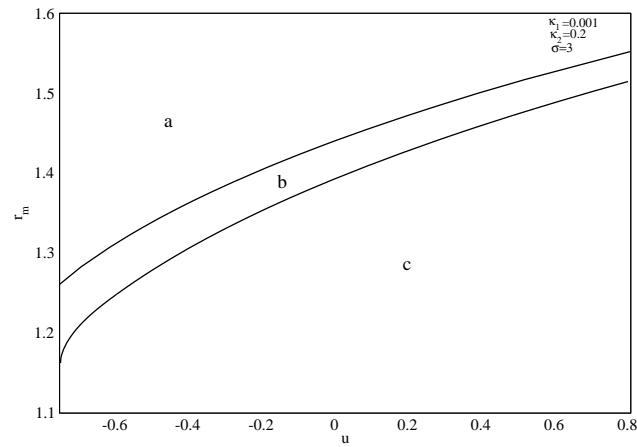


Figure 4.4: Two parameter bifurcation diagram of r_m against u , for system and parameters as in figure 4.3 and $\sigma = 3$. There are stable inphase oscillations in the region b,c, and stable antiphase oscillations in the region a,b.

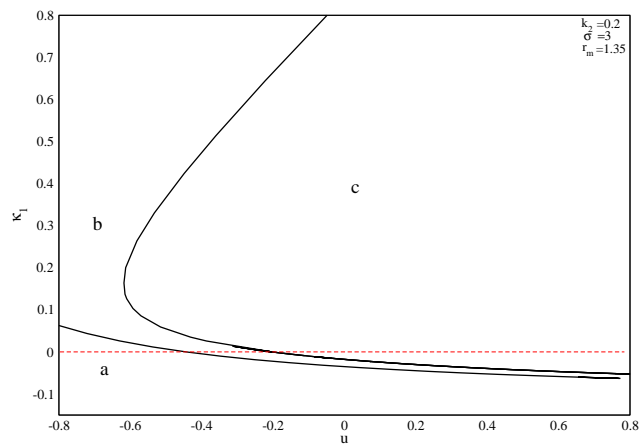


Figure 4.5: Bifurcation diagram of κ_1 against u for system and parameters as in figure 4.2(a,b) with $\kappa_2 = 0.2$. There are stable inphase oscillations in the region b,c, and antiphase in the region a,b.

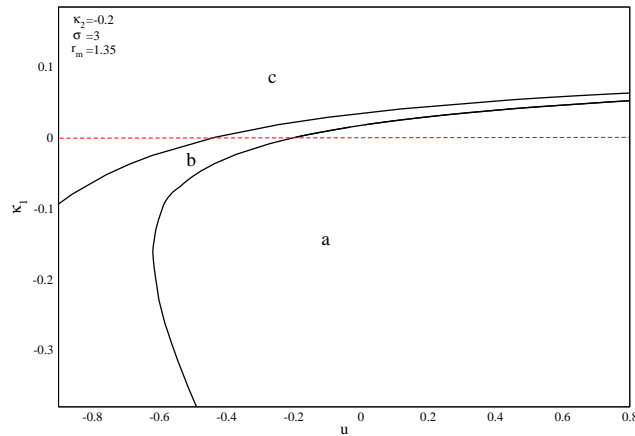


Figure 4.6: Two parameter bifurcation diagram of κ_1 against u for system and parameters as in figure 4.2(c,d) $\kappa_2 = -0.2$. There are stable antiphase oscillations in the region a,b, and inphase in the region b,c.

Table 4.1: Comparison of the bifurcation points, r_{in} , r_{anti} , u_{in} and u_{anti} , obtained from simulations of system (4.3) and those from equations (4.18, 4.19, 4.20, 4.21) for $\kappa_1 = 0$, $\kappa_2 = 0.2$, $\sigma = 3$ and $r_m = 1.35$.

| | r_{in} | r_{anti} | u_{in} | u_{anti} |
|---|----------|------------|----------|------------|
| From system (4.3) (figure 4.5) | 1.3210 | 1.376 | -0.4433 | -0.2027 |
| From equations (4.18, 4.19, 4.20, 4.21) | 1.3229 | 1.3771 | -0.4438 | -0.2032 |

and (d). Figure 4.6 has parameters as those in figure 4.5 except $\kappa_2 = -0.2$. The excursion of the bistable region ‘b’ above the dotted horizontal line indicates the appearance of within-burst synchrony changes for weak excitatory values, $\kappa_1 > 0$. Stronger κ_1 results in inphase spike synchronization.

Tables 4.1 and 4.2 show the comparison of the inphase and antiphase bifurcation points, r_{in} , u_{in} and r_{anti} , u_{anti} , for $\kappa_1 = 0$ and two values of κ_2 calculated from (4.18, 4.20) and (4.19, 4.21), respectively, with those from simulations of systems (4.3). Note that the bifurcation points obtained from (4.3) and the approximate (4.18, 4.19, 4.20, 4.21) agree very well.

Figures 4.7 and 4.8 portray bifurcation diagram in $u\kappa_2$ -space for two values κ_1 . These figures show the role of κ_2 in spike synchronization. Figure 4.7 uses the parameters: $\kappa_1 = 0.001$, $\sigma = 3$, $r_m = 1.35$. For negative and weak positive values

Table 4.2: Comparison of the bifurcation points as in table 4.1 except $\kappa_2 = -0.2$.

| | r_{in} | r_{anti} | u_{in} | u_{anti} |
|---|----------|------------|----------|------------|
| From system (4.3) (figure 4.6) | 1.376 | 1.321 | -0.2027 | -0.4433 |
| From equations (4.18, 4.19, 4.20, 4.21) | 1.377 | 1.3229 | -0.2032 | -0.4438 |

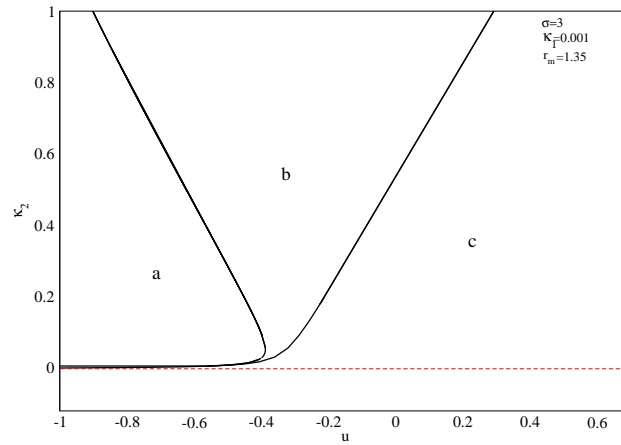


Figure 4.7: Two parameter bifurcation diagram of κ_2 against u for system and parameters as in figure 4.2(a,b) with $\kappa_1 = 0.001$. There are stable inphase oscillations in the region b,c, and antiphase in the region a,b.

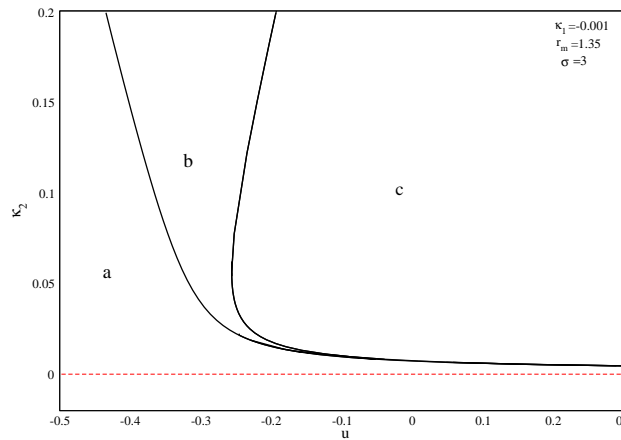


Figure 4.8: Bifurcation diagram as in figure 4.7 but $\kappa_1 = -0.001$. There are stable inphase oscillations in the region b,c, and antiphase in the region a,b.

of κ_2 (region c) only stable inphase solutions are present. It may be observed that the bistable region b narrows down with decreasing κ_2 without intersecting the bifurcation branches and the within-burst synchrony change move to the left or towards the end of the burst. In the simulation of the full system within-burst synchrony changes were not observed for smaller values of κ_2 in order of that of κ_1 , more precisely we did not observe within-burst synchrony changes for $\kappa_2 < 0.05$ and that is because the within-burst synchrony changes move more to the burst offset point preventing the synchrony changes in practice. Figure 4.8 shows the bifurcation diagram for $\kappa_1 = -0.001$. As before a,b are regions of stable antiphase, and b,c the stable inphase solutions. It may be observed that for negative and weak positive values of κ_2 (region a), one can see only stable antiphase synchronization of spikes in the burst.

4.2 Understanding within-burst synchrony changes from the constrained system

Recall from figure 4.1 that the constrained system can be used to explain periodic bursting with a within-burst synchrony change in coupled bursters. In this section we examine the effect of noise, the extension to three bursters and to more general couplings.

4.2.1 Effects of noise on within-burst synchrony changes

We include in this section a discussion of the influence of noise on the phenomenon of within-burst synchrony changes for coupled elliptic bursters. Noise was added to the fast subsystems of the governing system for two coupled bursters (3.4, 3.5, 3.6). We considered Wiener noise W which in the XPPAUT incorporated as ‘functions’ that return scaled white noise [33]. they are held fixed for t to $t + dt$ during an integration. At each time step, they are then changed and their value is a normally distributed random number with zero mean and unit variance. The program scales them by the appropriate time step as well. Their purpose is so that one can

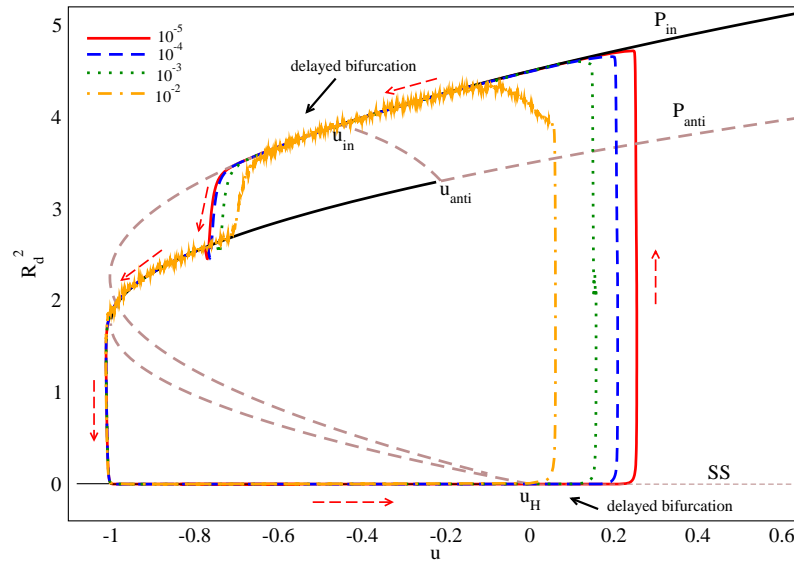


Figure 4.9: Noise dependent bifurcation delays both at onset of burst from Andronov-Hopf bifurcation point at u_H and within-burst synchrony change at u_{in} for two coupled bursters (3.4, 3.5, 3.6). The trajectories for the four indicated amplitudes of added noise with same initial conditions and parameters as in figure 3.9 with $u = \frac{u_1+u_2}{2}$ are superimposed on the bifurcation diagram 4.1. The dashed arrows show the direction of trajectory during a periodic bursts. Note the delays reduce with increasing noise amplitude; this is a typical slow passage effect.

use methods other than Euler for solving noisy problems. In our simulation we considered the noise term as δW where δ is a small amplitude. It is well known that bursters are significantly affected by the presence of noise, even if it is low amplitude, because of slow passage effects. In particular the Andronov-Hopf bifurcation at the onset of each burst is delayed by a time approximately proportional to the logarithm of the noise level [116, 95, 77, 78]. This effect can be understood as a delay in leaving the neighbourhood of the quiescent equilibrium state after it has gone unstable (i.e. where the slow variable passes through the Andronov-Hopf bifurcation point shown in figure 3.8(d)); larger amplitude noise generates the required fluctuation sooner.

However, there is an additional effect: within-burst synchrony change also exhibits a slow passage effect (a delayed pitchfork bifurcation at loss of synchrony). Figure 4.9 exhibits evidence of both slow passage effects; there are delays corresponding to transitions to bursting and synchrony change (u_H and u_{in} , respectively), depending on noise amplitude δ . On increasing noise above 10^{-2} (not shown) the synchrony change is no longer apparent because there are large fluctuations in the amplitude and phase difference within burst caused by the noise. Moreover, if the noise level is too small, the delay to the within-burst synchrony change may become longer than the length of the burst. Indeed, the system without noise may become ‘stuck’ in an inphase solution for the whole burst.

4.2.2 Examples with biologically-motivated coupling

We now demonstrate that within-burst synchrony changes may also emerge in systems of coupled Bautin bursters with more biologically motivated coupling schemes: this includes gap-junction coupling, i.e., a linear diffusive coupling, and nonlinear synaptic coupling as discussed in [30, 96] in the context of the Bautin normal form. Firstly, we consider gap-junction coupling K_j in (3.4) as

$$K_j = (\kappa_1 + i\kappa_2) \sum_{k=1}^n c_{jk}(z_k - z_j), \quad (4.22)$$

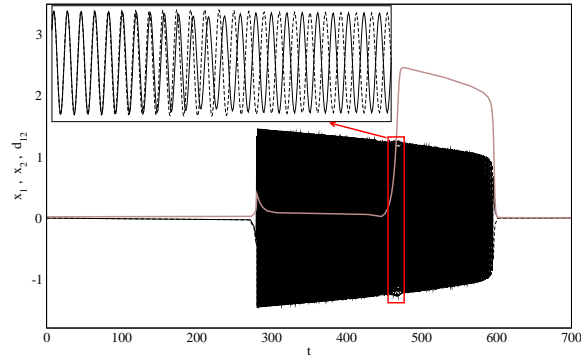


Figure 4.10: Within-burst synchrony change from stable inphase to stable antiphase states for two coupled bursters governed by the system (3.4, 3.5) and ‘gap-junction’ coupling (4.22). This pattern repeats during each burst. The parameters are $\sigma = 5$, $\kappa_1 = -0.001$, $\kappa_2 = 0.2$, $r_m = 1.35$, $\omega = 0.001$ and $\eta = 0.005$. A low amplitude noise of order 10^{-6} is added to the components of the fast subsystem.

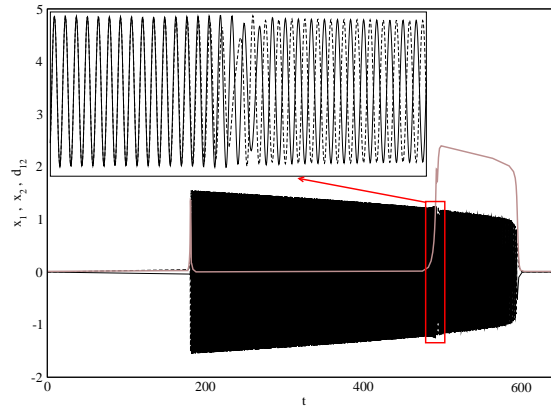


Figure 4.11: Within-burst synchrony change from stable inphase to stable antiphase states for two coupled bursters governed by the system (3.4, 3.5) and ‘nonlinear synaptic’ coupling (4.23). This pattern repeats during each burst. The parameters are $\sigma = 5$, $\kappa_1 = -0.001$, $\kappa_2 = 0.2$, $r_m = 1.35$, $\omega = 0.003$ and $\eta = 0.005$.

with $j \neq k$ but still a complex coefficient as in [30, 96]. Figure 4.10 demonstrates a simulation of (3.4, 3.5) for two coupled Bautin bursters with gap-junction coupling (4.22). It is apparent from this figure that the system undergoes within-burst synchrony changes from inphase to antiphase. Secondly, we consider cubic coupling between the bursters as an approximation to nonlinear synaptic coupling [30]:

$$K_j = (\kappa_1 + i\kappa_2) \sum_{k=1}^n c_{jk} z_k^2 \overline{z_k}. \quad (4.23)$$

Figure 4.11 shows the simulation of (3.4, 3.5) with nonlinear coupling (4.23) for two coupled bursters. As in the direct and gap-junction coupling cases, the system undergoes within-burst synchrony changes from inphase to antiphase. We have not done a detailed analysis of burst constrained systems with gap-junction and nonlinear synaptic coupling, but this should be possible as in Section 4.1. The simulations presented here show in particular that direct coupling is not necessary for within-burst synchrony changes in coupled Bautin bursters. Moreover, it is obvious that inclusion of biologically motivated coupling types (4.22, 4.23) do not pose any additional mathematical complexity. It is obvious that the extra term z_j in the gap-junction coupling (4.22) merely shifts the bifurcation points u_{in} and u_{anti} and similar mathematical analysis may be carried out for these coupling cases.

The examples we have studied are clearest for ‘long’ bursts where there are many oscillations within a burst. Similar effects are also present in shorter bursts, but are harder to observe because the changes in synchrony must occur over a small number of spikes to be observable. Moreover, burst length is inversely proportional to the slow time scale η , so the clearest within-burst synchrony changes are observed for sufficiently small η . Also note that eigenvalues for the fast subsystem (4.9, 4.10) depend on the coupling strength but not on η , so apart from bifurcation delay we expect no constraint between η , κ_1 and κ_2 other than all being small enough.

Chapter 5

Within-burst cascade of synchrony changes

In the previous chapter we analyzed the within-burst synchrony change property of two coupled elliptic bursters governed by (3.8) with nonisochronicity given by (3.10, 3.11, 3.12). The synchrony change is associated with the turning point in instantaneous frequency (frequency transition) within a burst. So, it is intuitive that if non-isochronous term in the fast subsystem accommodates multiple frequency transitions, then this should cause a sequence of synchrony changes within a coupled system of elliptic bursters. In this chapter we show that multiple frequency transitions can cause multiple synchrony changes. We call the latter within burst cascades of synchrony changes. Here we explore both numerically and analytically examples of within-burst cascade synchrony changes in coupled elliptic bursters, by having an appropriate modification to our model and we restrict our investigation to two elliptic bursters with direct coupling between them.

5.1 The model

To begin with, we present a model for a single elliptic burster with a specified frequency transition of fast spikes at two points within one burst period and then we present an example of two elliptic bursters with direct coupling.

5.1.1 Single compartment elliptic burster

We modify the original system(3.8) by incorporating additional frequency transitions. The normal form for single compartment Bautin elliptic burster may be written separating the complex terms in the fast subsystem as

$$\left. \begin{aligned} \dot{z} &= uz + 2z|z|^2 - z|z|^4 + i\Omega z \\ \dot{u} &= \eta(a - |z|^2) \end{aligned} \right\} \quad (5.1)$$

and

$$\Omega = \omega + \omega_0|z|^2 + \omega_1|z|^4 + \omega_2|z|^6. \quad (5.2)$$

Here ω is the frequency of the fast spiking as before and $\omega_0, \omega_1, \omega_3 \in \mathbb{R}$. We assume,

$$\left. \begin{aligned} \frac{d\Omega}{dr} &= \sigma r(r^2 - r_p^2)(r^2 - r_q^2) \\ &= \sigma (r^5 - (r_p^2 + r_q^2)r^3 + r_p^2 r_q^2 r). \end{aligned} \right\} \quad (5.3)$$

So,

$$\left. \begin{aligned} \Omega &= \omega + \frac{1}{2}\sigma r_p^2 r_q^2 r^2 - \frac{1}{4}\sigma(r_p^2 + r_q^2)r^4 + \frac{1}{6}\sigma r^6 \\ &= \omega + \frac{1}{2}\sigma r_p^2 r_q^2 |z|^2 - \frac{1}{4}\sigma(r_p^2 + r_q^2)|z|^4 + \frac{1}{6}\sigma |z|^6. \end{aligned} \right\} \quad (5.4)$$

Comparing (5.2) and (5.4) we obtain

$$\left. \begin{aligned} \omega_0 &= \frac{1}{2}\sigma r_p^2 r_q^2 \\ \omega_1 &= -\frac{1}{4}\sigma(r_p^2 + r_q^2) \\ \omega_2 &= \frac{1}{6}\sigma. \end{aligned} \right\} \quad (5.5)$$

Here, $r_p, r_q \in \mathbb{R}$ signify the position of frequency transitions along the burst profile, and we assume $r_p < r_q < r$ with $z = x + iy$, $r = \sqrt{x^2 + y^2}$.

5.1.2 Model for coupled elliptic bursters

The general model for elliptic bursters directly coupled with all-to-all may be written as

$$\left. \begin{aligned} \dot{z}_j &= u_j z_j + 2z_j |z_j|^2 - z_j |z_j|^4 + i\Omega_j z_j + K_j \\ \dot{u}_j &= \eta(a - |z_j|^2), \end{aligned} \right\} \quad (5.6)$$

Where

$$\left. \begin{aligned} \Omega_j &= \omega + \frac{1}{2}\sigma r_p^2 r_q^2 |z_j|^2 - \frac{1}{4}\sigma(r_p^2 + r_q^2)|z_j|^4 + \frac{1}{6}\sigma|z_j|^6 \\ K_j &= (\kappa_1 + i\kappa_2) \sum_{k=1}^n c_{jk} z_k. \end{aligned} \right\} \quad (5.7)$$

We set $c_{jk} = 1$ implying all-to-all coupling between the bursters and $j, k = 1, \dots, n$, where n is the number of bursting cells.

5.2 Cascades with two synchrony changes

In this section we explore the within-burst synchrony changes for two coupled elliptic bursters where each of the burster dynamics is governed by (5.1, 5.4) and the coupled system by (5.6, 5.7). The frequency changes at r_p and r_q are expected to cause a double within-burst synchrony changes associated with r_p and r_q , respectively. The Euclidean of (5.6, 5.7) for $n = 2$ may be written as

$$\left. \begin{aligned} \dot{x}_j &= (u_j x_j - \omega y_j) + \left(2x_j - \frac{\sigma r_p^2 r_q^2}{2} y_j\right)(x_j^2 + y_j^2) + \left(-x_j + \frac{\sigma(r_p^2 + r_q^2)}{4} y_j\right)(x_j^2 + y_j^2)^2 \\ &\quad - \frac{\sigma}{6} y_j (x_j^2 + y_j^2)^3 + \kappa_1 x_k - \kappa_2 y_k \\ \dot{y}_j &= (\omega x_j + u_j y_j) + \left(\frac{\sigma r_p^2 r_q^2}{2} x_j + 2y_j\right)(x_j^2 + y_j^2) + \left(-y_j - \frac{\sigma(r_p^2 + r_q^2)}{4} x_j\right)(x_j^2 + y_j^2)^2 \\ &\quad + \frac{\sigma}{6} x_j (x_j^2 + y_j^2)^3 + \kappa_2 x_k + \kappa_1 y_k \\ \dot{u}_j &= \eta(a - x_j^2 - y_j^2). \end{aligned} \right\} \quad (5.8)$$

Here, $j, k = 1, 2$, and $j \neq k$.

5.2.1 Simulation of two within-burst synchrony changes

We numerically investigate the dynamics of two coupled elliptic bursters governed by the system (5.8). Burst synchronization between the cells can easily be achieved for a wide range of parameter values with this system. With excitatory coupling this generally generates inphase bursts, while antiphase bursts result from inhibitory coupling. There are spontaneous within-burst cascades of synchrony changes observable in Figure 5.1. Panel (b) shows the periodic bursts with the fast variables x_1

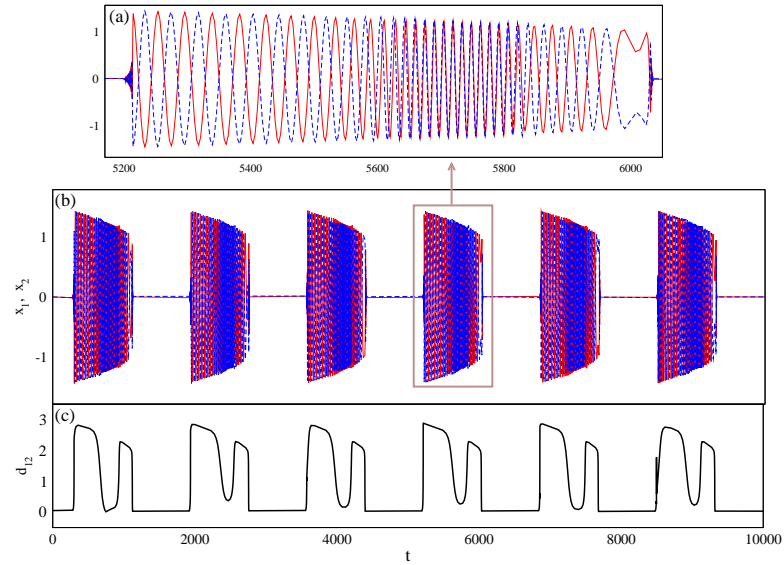


Figure 5.1: Within-burst cascade of synchrony changes from stable antiphase to stable inphase to again stable antiphase states for two coupled elliptic bursters. Activity pattern of one burst (shown in box) has been blown up in (a); within-burst cascade of synchrony changes repeats during each burst and the burst repeats periodically (b). Note that the two coupled bursters are burst synchronized (b) and the spikes become antiphase at the beginning of the burst, then changes to inphase around the middle and again changes to antiphase towards the end of the burst (a). These transitions are also observable from d_{12} (c). These within-burst synchrony changes are characterized by two transitions described by (5.8).

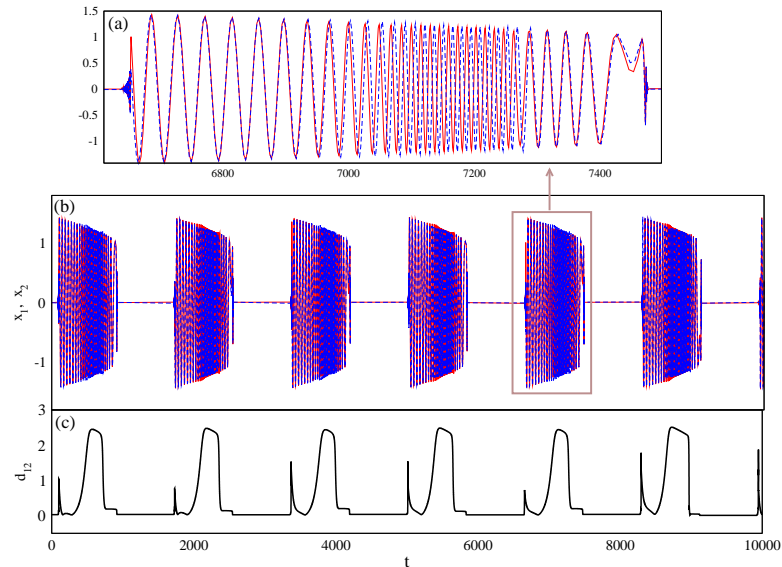


Figure 5.2: Within-burst cascade of synchrony changes from stable inphase to stable antiphase and back to stable inphase states. The governing system and details are as in Figure 5.1 except for $\kappa_1 = 0.008$, $\kappa_2 = -0.1$.

and x_2 . All transients were allowed to decay. One burst is blown up in the panel (a) showing the synchronization and transitions. The distinguishing solid and dashed traces correspond to the two bursting activity patterns, respectively. The panel (c) shows the Euclidean distance $d_{12} = \sqrt{(x_1 - x_2)^2 + (y_1 - y_2)^2 + (u_1 - u_2)^2}$ between the two bursters to the presence ($d_{12} = 0$) or absence ($d_{12} > 0$) of synchronization. The simulations were done with XPPAUT [33]. For integrations, the built-in adaptive Runge-Kutta integrator was used. The parameters in the simulation are $\sigma = 8$, $\kappa_1 = -0.008$, $\kappa_2 = 0.1$, $r_p = 1.2$, and $r_q = 1.4$. Independent Wiener noise of amplitude 10^{-6} was added to the fast variables. The spikes are antiphase at the beginning of the burst, until the frequency transition in the fast spiking occurs at $r_q = 1.4$ where they change to inphase. Then the spikes again change to antiphase caused by the frequency transition at $r_p = 1.2$. Consequently, we observe within-burst cascades of synchrony changes and this is also obvious from d_{12} .

We present another example in Figure 5.2 of within-burst cascades of synchrony changes for the system (5.8) but with different parameter values. The parameter values are same as those in Figure 5.1 except for the coupling strengths: $\kappa_1 = 0.008$,

$\kappa_2 = -0.1$. Noise of amplitude 10^{-6} was also added to the fast subsystems of the bursters. The panel (a) shows the synchrony patterns of the two bursters illustrated by the corresponding fast variables x_1 and x_2 . The bursts are synchronized throughout (b) but the spikes are inphase at the beginning of the burst, until the frequency transition at $r_q = 1.4$ where they change to antiphase. Then the spikes again change back to inphase due to the frequency transition at $r_p = 1.2$. These examples demonstrate that the within-burst cascades of synchrony changes can appear as a pair of frequency changes involving the fast spiking of the bursters.

5.2.2 The burst-synchronized constrained model

In this section, we carry out similar basic analysis of the within-burst cascades of synchrony changes as in Chapter 4. We do this by considering a burst-synchronized constrained system for (5.6) and (5.7). Generally, the burst-synchronized constrained system for coupled n -Bautin burster may be written as

$$\left. \begin{aligned} \dot{z}_j &= u_j z_j + 2z_j |z_j|^2 - z_j |z_j|^4 + i\Omega_j z_j + K_j \\ \dot{u} &= \eta \left(a - \frac{1}{n} \sum_{j=1}^n |z_j|^2 \right) \end{aligned} \right\} \quad (5.9)$$

with the constraint $u_1 = u_2 = \dots = u$ so that the system is put to exact burst synchronization by the constraint and here $j = 1, \dots, n$. We write the burst-synchronized constrained system (5.9) in polar coordinates using transformation $z_j = r_j e^{i\theta_j}$ for $n = 2$ as

$$\left. \begin{aligned} \dot{r}_1 &= u_1 r_1 + 2r_1^3 - r_1^5 + r_2 (\kappa_1 \cos(\theta_2 - \theta_1) - \kappa_2 \sin(\theta_2 - \theta_1)) \\ \dot{\theta}_1 &= \omega + \frac{1}{2} \sigma r_p^2 r_q^2 r_1^2 - \frac{1}{4} \sigma (r_p^2 + r_q^2) r_1^4 + \frac{1}{6} \sigma r^6 \\ &\quad + \frac{r_2}{r_1} (\kappa_1 \sin(\theta_2 - \theta_1) + \kappa_2 \cos(\theta_2 - \theta_1)) \\ \dot{r}_2 &= u_2 r_2 + 2r_2^3 - r_2^5 + r_1 (\kappa_1 \cos(\theta_1 - \theta_2) - \kappa_2 \sin(\theta_1 - \theta_2)) \\ \dot{\theta}_2 &= \omega + \frac{1}{2} \sigma r_p^2 r_q^2 r_2^2 - \frac{1}{4} \sigma (r_p^2 + r_q^2) r_2^4 + \frac{1}{6} \sigma r^6 \\ &\quad + \frac{r_1}{r_2} (\kappa_1 \sin(\theta_1 - \theta_2) + \kappa_2 \cos(\theta_1 - \theta_2)) \\ \dot{u} &= \eta \left(a - \frac{1}{2} (r_1^2 + r_2^2) \right). \end{aligned} \right\} \quad (5.10)$$

As we are interested in synchrony changes, we define longitudinal and transverse coordinates

$$\left. \begin{aligned} r_l &= (r_1 + r_2)/2 \\ r_t &= (r_1 - r_2)/2 \\ \phi &= \theta_1 - \theta_2. \end{aligned} \right\} \quad (5.11)$$

Thus, the system (5.10), with transformations (5.11), reduces to

$$\left. \begin{aligned} \dot{r}_l &= ur_l + 2r_l^3 + 6r_l r_t^2 - r_l^5 - 10r_l^3 r_t^2 - 5r_l r_t^4 + \kappa_1 r_l \cos \phi - \kappa_2 r_t \sin \phi \\ \dot{r}_t &= ur_t + 6r_l^2 r_t + 2r_t^3 - 5r_l^4 r_t - 10r_l^2 r_t^3 - r_t^5 - \kappa_1 r_t \cos \phi + \kappa_2 r_l \sin \phi \\ \dot{\phi} &= 2\sigma r_p^2 r_q^2 r_l r_t - 2\sigma(r_p^2 + r_q^2)r_l r_t(r_l^2 + r_t^2) + \frac{2}{3}r_l r_t(3r_l^4 + 10r_l^2 r_t^2 + 3r_t^4) \\ &\quad - 2\kappa_1 \frac{(r_l^2 + r_t^2)}{r_l^2 - r_t^2} \sin \phi - 4\kappa_2 \frac{r_l r_t}{r_l^2 - r_t^2} \cos \phi \\ \dot{u} &= \eta(a - (r_l^2 + r_t^2)). \end{aligned} \right\} \quad (5.12)$$

Note the system (5.12) is same as (4.5) except the phase dynamics of the former contains the non-isochronicity associated with the a pair of frequency transitions of the fast spiking characterized by r_p and r_q resulting in two synchrony changes. In (5.12), (r_l, r_t, ϕ) govern the fast dynamics, and u governs the slow dynamics. This system can be used to understand the spike synchrony behaviour of the coupled system by the analysis of the fast subsystem via singular perturbation method [93].

5.2.3 Synchrony bifurcation of the fast subsystem

We carry out a numerical bifurcation analysis of the fast subsystem of (5.12) by taking η as the singular perturbation parameter to understand the within-burst cascades of synchrony changes observed in Figures 5.1, 5.2. We present in Figure 5.3 bifurcations of a bursting solution of (5.10) projected onto the phase difference, ϕ , as u is varied. The solid lines represent the stable periodic solutions, while the unstable solutions are shown with dash-dotted lines. The arrow, running from right to left, shows the direction of change of u . What Figure 5.3 shows is a burst that begins with stable inphase solution, and then antiphase solutions gain stability via a bifurcation and again the antiphase solutions lose stability to stable inphase

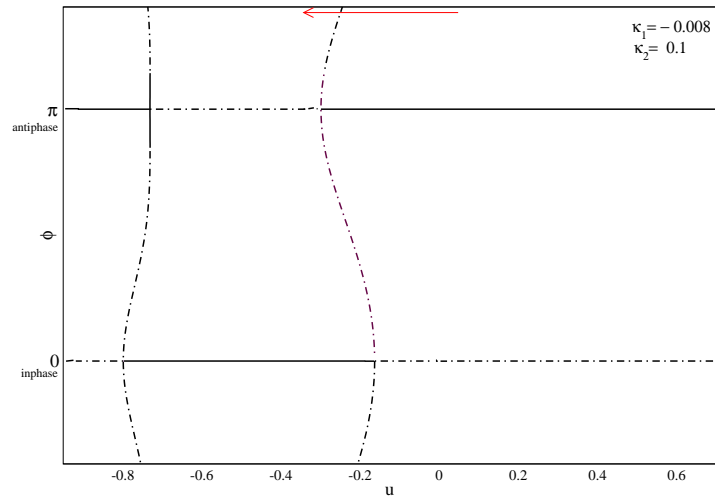


Figure 5.3: Bifurcation diagram of ϕ against u for the burst-synchronized constrained system (5.12), where u is a parameter that slowly decreases during each burst. The parameters are $\sigma = 8$, $r_p = 1.2$, $r_q = 1.4$, $\kappa_1 = -0.008$ and $\kappa_2 = 0.1$. The solid lines represent stable solutions, while the unstable solutions are shown with dash-dotted lines. The arrow, running from right to left, shows the direction of the change of u during the active phase of the burst. Note this bifurcation diagram agrees with the synchrony changes observed in Figure 5.1.

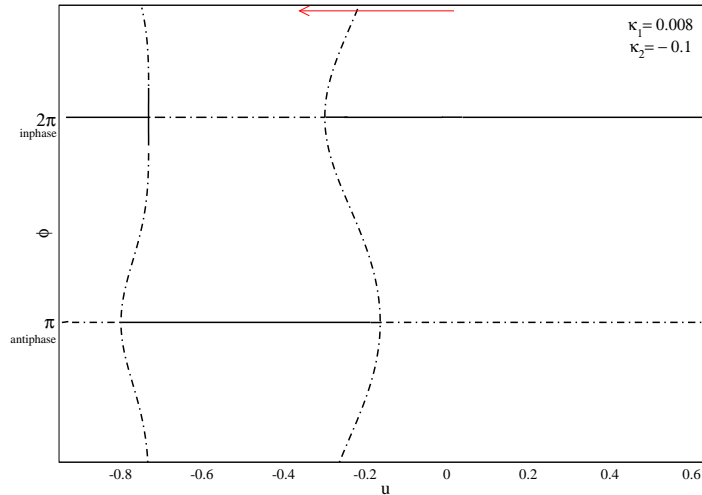


Figure 5.4: Bifurcation diagram of ϕ against u for the burst-synchronized constrained system (5.12) with parameters $\sigma = 8$, $r_p = 1.2$, $r_q = 1.4$, $\kappa_1 = 0.008$ and $\kappa_2 = -0.1$. The solid lines represent stable solutions, while the unstable solutions are shown with dash-dotted lines. The arrow, running from right to left, shows the direction of the change of u . Note this bifurcation diagram agrees with the synchrony changes observed in Figure 5.2.

solutions. So, this bifurcation diagram implies the presence of multiple bifurcations on the periodic orbit of the bursting solutions associated with inphase and antiphase synchrony patterns. Note the presence of bistable regions between the bifurcations of antiphase and inphase solutions as also observed in Figure 4.2. The parameters in this result are $\sigma = 8$, $r_p = 1.2$, $r_q = 1.4$, $\kappa_1 = -0.008$ and $\kappa_2 = 0.1$. This behaviour agrees with the simulation result shown in Figure 5.1. Similarly, Figure 5.4 agrees with what is observed in the simulation in Figure 5.2. Here burst starts of stable inphase, then changes to stable antiphase and again changes back to stable inphase. The parameter values in this result are $\sigma = 8$, $r_p = 1.2$, $r_q = 1.4$, $\kappa_1 = 0.008$ and $\kappa_2 = -0.1$. Hence, both bifurcation diagrams (Figures 5.3, 5.4) from the burst-synchronized constrained system (5.12) demonstrate the effect of within-burst cascade of synchrony changes associated with the a pair frequency transitions in the fast spiking dynamics.

5.2.4 Stability analysis of the burst-synchronized constrained system

In this section, we carry out a linear stability analysis similar to Section 4.1 of the fast subsystem of (5.12) about inphase and antiphase states with $r_t = 0$ and $r_l = r$, which means both cells are burst synchronized with $r_1 = r_2 = r$. In this analysis, we assume that the slow variable u is a constant of the system by setting the time scale ratio, $\eta = 0$. The dynamics, as a result, is only governed by the fast spiking activity. For $r_t = 0$ and $\eta = 0$ we write $r_l = r$ as the stable nontrivial solution of (5.12) in the appropriate subspace (4.7) corresponding to bursting behaviour. Note that for small $|\kappa_1|$ there will be a solution close to the single burster case. For the fast subsystem of (5.12) with u between -1 and +1, one can verify the existence of two solutions

- Inphase where $r_t = \phi = 0$, $r_l = r$,
- Antiphase where $r_t = 0$, $\phi = \pi$, $r_l = r$,

where $r > 0$ is the solution of (4.8).

The Jacobian for the fast system at the inphase solution is block diagonal with a single real eigenvalue and a block

$$J_{in} = \begin{pmatrix} u + 6r^2 - 5r^4 - \kappa_1 & \kappa_2 r \\ 2\sigma r_p^2 r_q^2 r - 2\sigma(r_p^2 + r_q^2)r^3 + 2r^5 - \frac{4\kappa_2}{r} & -2\kappa_1 \end{pmatrix}. \quad (5.13)$$

Note that the off-diagonal entries of the Jacobian matrices (5.13) depend on the imaginary part of the coupling coefficient, κ_2 , and other system parameters. The real eigenvalues can be assumed negative because of stability of the solution of (4.7). The eigenvalues of the equation (5.13) can be determined by examining the trace of the matrix (5.13) which is same as (4.11) and the determinant

$$\det(J_{in}) = -2(u + 6r^2 - 5r^4)\kappa_1 - 2\sigma r^2(r_p^2 - r^2)(r_q^2 - r^2)\kappa_2 + 2\kappa_1^2 + 4\kappa_2^2. \quad (5.14)$$

5.2.5 Case $\kappa_1 = 0$

We consider the special case when $\kappa_1 = 0$, and $|\kappa_2| \ll 1$. In such a case, it may easily be seen that $tr(J_{in})$ in (4.11) is negative, as stability of the periodic solution

of (4.7) means that $u + 6r^2 - 5r^4 < 0$. So, from (4.11), $tr(J_{in}) < 0$. For this weak coupling, it is also evident that $(tr(J_{in}))^2 > 4det(J_{in})$. Hence, the system will have a stable node for $det(J_{in}) > 0$ and a saddle for $det(J_{in}) < 0$.

To explain the within-burst synchrony changes observed in Figures 5.1 and 5.2, we may write the determinant of the matrix (5.13) to first order in κ_2 (small $\kappa_2 > 0$) by setting $\kappa_1 = 0$ as

$$det(J_{in}) = -2\sigma r^2(r_p^2 - r^2)(r_q^2 - r^2)\kappa_2 + O(\kappa_2^2). \quad (5.15)$$

From equation (5.15), there are three scenarios of possible solutions:

- Unstable inphase for $r < r_p + O(\kappa_2), r_q + O(\kappa_2)$, implying $det(J_{in}) < 0$ and $tr(J_{in}) < 0$;
- stable inphase for $r_p + O(\kappa_2) < r < r_q + O(\kappa_2)$, implying $det(J_{in}) > 0$ and $tr(J_{in}) < 0$;
- unstable inphase for $r > r_p + O(\kappa_2), r_q + O(\kappa_2)$, implying $det(J_{in}) < 0$ and $tr(J_{in}) < 0$.

We may calculate approximate values of r where the bifurcations take place by equating $det(J_{in})$ to zero. Thus, from equation (5.14) with $\kappa_1 = 0$ we obtain

$$\left. \begin{aligned} det(J_{in}) &= -\kappa_2 \left(-\sigma r^2(r_p^2 - r^2)(r_q^2 - r^2) - 2\kappa_2 \right) \\ &= r^6 - (r_p^2 + r_q^2)r^4 + r_p^2 r_q^2 r^2 - \frac{2\kappa_2}{\sigma} \\ &= 0. \end{aligned} \right\} \quad (5.16)$$

Now for simplicity we assume $r_P = r_p^2 + r_q^2$, $r_Q = r_p^2 r_q^2$, $k_2 = \frac{2\kappa_2}{\sigma}$, and $r^2 = x$. So, equation (5.16) reduces to

$$x^3 - r_P x^2 + r_Q x - k_2 = 0. \quad (5.17)$$

For given values of κ_2 , r_p , r_q and σ , equation (5.17) can be solved to obtain the r bifurcation points numerically to an order $O(\kappa_2^2)$, and the corresponding slow variables, u 's, may be obtained from (4.8). Analytical expressions for bifurcation points in this case will be harder to obtain as Equation (5.17) is a general cubic expression.

5.2.6 Case $\kappa_1 \neq 0$

In this section we carry out a qualitative analysis for stability of the inphase solution. We may write the trace of (5.13) as

$$\text{tr}(J_{in}) = u + 6r^2 - 5r^4 - 3\kappa_1 = -|T|, \quad (5.18)$$

so (5.14) may be written to the first order in κ_1 and κ_2 with small $\kappa_1 < 0$, and small $\kappa_2 > 0$ as

$$\det(J_{in}) = 2|T|\kappa_1 - 2\sigma r^2(r_p^2 - r^2)(r_q^2 - r^2)\kappa_2 + O(\kappa_1^2, \kappa_2^2). \quad (5.19)$$

It is clear that the term $2|T|\kappa_1$ is negative because of negative κ_1 as per assumption in (5.19). So, as before for $r < (r_p + O(\kappa_2), r_q + O(\kappa_2))$, $\det(J_{in}) < 0$, and with $\text{tr}(J_{in}) < 0$ this means the inphase solution is unstable. But as r grows to $r_p + O(\kappa_2) < r < r_q + O(\kappa_2)$, we observe $2|T|\kappa_1$ must be smaller than $-2\sigma r^2(r_p^2 - r^2)(r_q^2 - r^2)\kappa_2$ to have a bifurcation so that inphase solution may become stable with $\det(J_{in}) > 0$ and $\text{tr}(J_{in}) < 0$. This implies κ_1 must be very small for such dynamics. Again, as r grows further to $r > r_p + O(\kappa_2), r_q + O(\kappa_2)$, we obtain $\det(J_{in}) < 0$ and $\text{tr}(J_{in}) < 0$, so the inphase solution becomes unstable. For nonzero κ_1 and κ_2 one such example is the simulation Figure 5.1 with $\kappa_1 = -0.008$ and $\kappa_2 = 0.1$ where the bursts starts off stable antiphase (unstable inphase) and changes to stable inphase and again antiphase (inphase) becomes stable (unstable) towards the end.

5.3 Cascades with multiple synchrony changes

We observe the within-burst cascades of synchrony changes resulting from multiple frequency transitions in the fast spiking of the elliptic bursters irrespective of coupling types (Section 4.2.2). In this section, we develop a Bautin elliptic burster model by considering a transcendental non-isochronicity. Under this modification each Bautin elliptic burster dynamics is governed by the system (5.1) with Ω defined as

$$\Omega = \omega + \sigma \sin(k|z|^2). \quad (5.20)$$

Here, $k, \sigma \in \mathbb{R}$ are parameters. Obviously, Ω in the form (5.20) implies multiple frequency transitions in the fast spiking dynamics of the burst governed by (5.1) and the value of k would affect the number of such frequency transitions; a higher k indicates more number of frequency transitions and this is expected to cause more cascades in the within-burst synchrony changes. In what follows in the section we attempt to obtain more cascades by simulating the system (5.1) with the transcendental Ω (5.20) in two all-to-all directly coupled Bautin elliptic bursters (similar to the coupling in (5.7)).

5.3.1 Two coupled bursters

In this section, we study two directly coupled Bautin bursters, each of which is governed by the system (5.1) and (5.20). The Euclidean of (5.1) together with (5.20) for two coupled system may be written as

$$\left. \begin{aligned} \dot{x}_j &= (u_j x_j - \omega y_j) + 2x_j(x_j^2 + y_j^2) - x_j(x_j^2 + y_j^2)^2 - \sigma y_j \sin(k(x_j^2 + y_j^2)) \\ &\quad + \kappa_1 x_k - \kappa_2 y_k \\ \dot{y}_j &= (\omega x_j + u_j y_j) + 2y_j(x_j^2 + y_j^2) - y_j(x_j^2 + y_j^2)^2 + \sigma x_j \sin(k(x_j^2 + y_j^2)) \\ &\quad + \kappa_2 x_k + \kappa_1 y_k \\ \dot{u}_j &= \eta(a - x_j^2 - y_j^2). \end{aligned} \right\} \quad (5.21)$$

Here, $j, k = 1, 2$, and $j \neq k$.

Figure 5.5 illustrates the within-burst cascade of synchrony changes in the coupled system (5.21) where the cascades contain more than two synchrony changes as observed before in Figures 5.1 and 5.2. The parameters for both Figures 5.5(a) and (b) are $\omega = 10^{-6}$, $\sigma = 7$, $\eta = 0.005$; the parameter $k = 13$. Here only one burst period is shown in each case and this pattern repeats. Here the activity of the two bursts, x_1, x_2 , are superimposed and it is obvious that the bursts are synchronized. The simulation was conducted in XPPAUT [33] with Runge-Kutta integrator. In Figure 5.5(a), the coupling co-efficients are $\kappa_1 = 0.001$ and $\kappa_2 = 0.1$. Here we observe that the synchronized bursts begin with inphase spikes and then spike synchronization changes to antiphase and then to inphase, then to antiphase

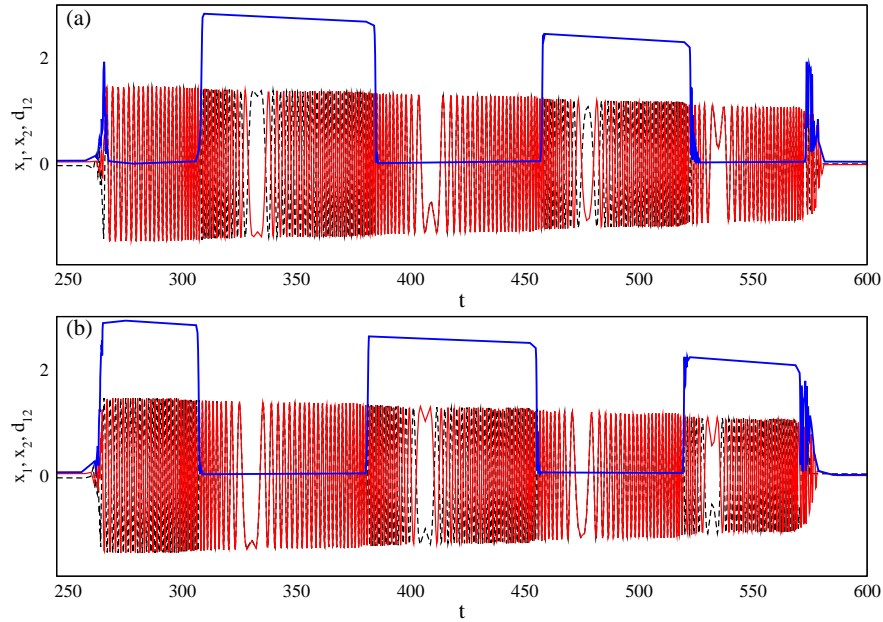


Figure 5.5: Simulation of the system (5.21) showing two examples with different coupling parameters of within-burst cascade of synchrony changes. Only one burst in each example has been amplified for better observation. The burst pattern repeats with time. Each of these simulations has been obtained after a run of 10^6 steps to get rid of all transients. Note the cascade changes from inphase to antiphase spikes along the burst profile as depicted by d_{12} (thick line) and the spike activities, x_1 and x_2 , of the two bursters shown with solid and dashed lines, respectively. Note the different order in which the synchrony patterns change from inphase to antiphase and vice versa in (a) and (b).

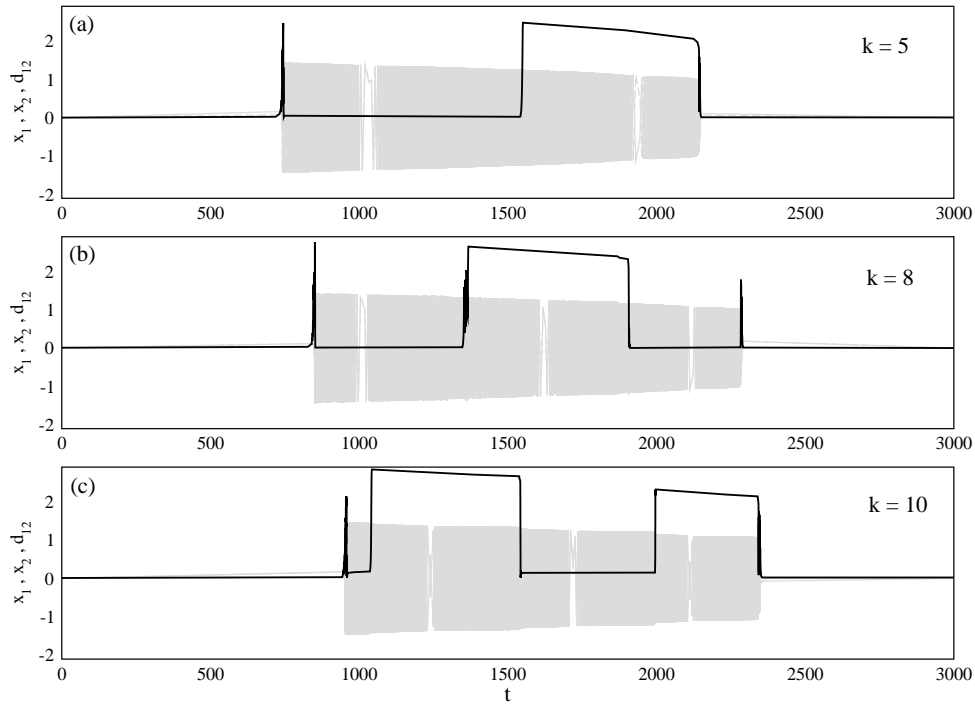


Figure 5.6: Simulation of the system (5.21) for different k . Note the increasing number of synchrony changes in the within-burst cascades of synchrony changes as k is increased from (a) to (c). Only one burst is chosen for better depiction, and the pattern repeats with time. The time series of corresponding d_{12} is superimposed in bold line; $d_{12} = 0$ indicates inphase spikes while $d_{12} \neq 0$ indicates antiphase.

and finally to inphase at the end of the bursts. So, this is an illustration of within-burst cascade of synchrony changes involving more than two synchrony changes. Likewise, Figure 5.5(b) shows another simulation with $\kappa_1 = -0.001$ and $\kappa_2 = -0.1$ illustrating similar within-burst cascade of synchrony changes behaviour, but with an opposite order in the synchrony pattern to the earlier one. In both cases, d_{12} with zero and nonzero values indicates inphase and antiphase spike synchronization, respectively.

5.3.2 Cascades with varying number of synchrony changes

The increased number of synchrony changes or cascades in Figure 5.5 in the within-burst synchrony changes were obtained by considering a transcendental Ω defined in (5.20) with a high $k = 13$. In Figure 5.6, we give results of simulation for two

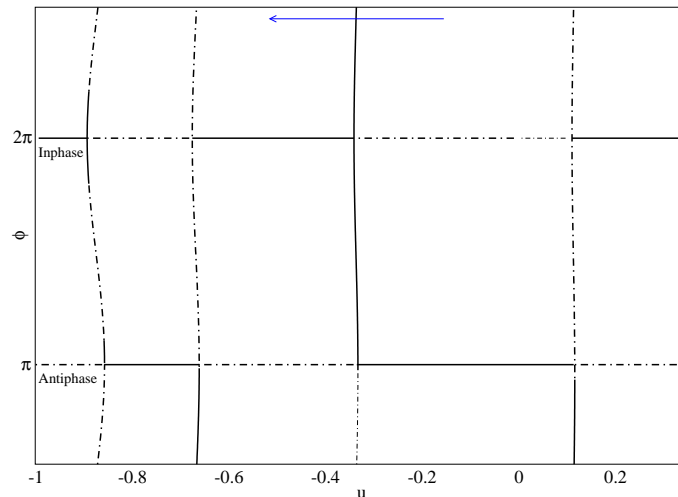


Figure 5.7: Bifurcation diagram of ϕ against u for the burst-synchronized constrained system (5.22), where u is a parameter that slowly decreases during each burst (shown with arrow). The parameters are $\kappa_1 = 0.001$, $\kappa_2 = 0.1$, $\omega = 10^{-6}$, $\sigma = 7$, $\eta = 0.005$, and $k = 13$. The solid lines represent stable solutions, while the unstable solutions are shown with dash-dotted lines. Indeed this bifurcation diagram agrees with the cascades of synchrony changes observed in Figure 5.5(a).

coupled Bautin bursters governed by (5.21) with varying k . The parameters in all the realizations are $\kappa_1 = 0.001$, $\kappa_2 = 0.1$, $\omega = 0.001$, $\sigma = 8$, and $\eta = 0.001$, and low amplitude noise of order 10^{-6} was added to the fast subsystems. It is obvious from the figure that an increasing number of synchrony changes follows on increasing the value of k . In Figure 5.6(a) and (b) we observe single and double synchrony changes, respectively. We obtained such behaviour previously with algebraic Ω in Section 5.2. In fact, the transcendental form for Ω in (5.1) offers a more general non-isochronous expression.

5.3.3 Bifurcation of the fast subsystem with cascades

A similar bifurcation analysis of the fast subsystem of the burst-synchronized constrained system for coupled Bautin bursters can be done to understand the behaviour of such cascade of synchrony changes. In this case as before, by deriving a burst synchronized model of Bautin burster given by (5.1) and (5.20), one can

obtain a similar system as (5.12) and the fast subsystem can be analyzed to give a bifurcation diagram of ϕ against u . By following the above procedure and incorporating transformation as (5.11) we obtain the following burst-synchronized constrained model for system with transcendental non-isochronicity:

$$\left. \begin{aligned} \dot{r}_l &= u_l r_l + u_t r_t + 2r_l^3 + 6r_l r_t^2 - r_l^5 - 10r_l^3 r_t^2 - 5r_l r_t^4 + \kappa_1 r_l \cos \phi - \kappa_2 r_t \sin \phi \\ \dot{r}_t &= u_l r_t + u_t r_l + 6r_l^2 r_t + 2r_t^3 - 5r_l^4 r_t - 10r_l^2 r_t^3 - r_t^5 - \kappa_1 r_t \cos \phi + \kappa_2 r_l \sin \phi \\ \dot{\phi} &= \sigma \sin(k(r_l + r_t)^2) - \sigma \sin(k(r_l - r_t)^2) \\ &\quad - 2\kappa_1 \frac{(r_l^2 + r_t^2)}{r_l^2 - r_t^2} \sin \phi - 4\kappa_2 \frac{r_l r_t}{r_l^2 - r_t^2} \cos \phi \\ \dot{u}_l &= \eta (a - (r_l^2 + r_t^2)). \end{aligned} \right\} \quad (5.22)$$

Figure 5.7 shows one such diagram of bifurcation analysis for such system. The parameters of the analysis are as in Figure 5.5(a). Here, the solid line represents stable periodic solutions of the burst-synchronized constrained system with Ω in the form (5.1) and the dash-dotted line represents unstable solutions. In this figure the multiple cascades representing synchrony changes between stable inphase and stable antiphase can clearly be observed, and this behaviour is same as found in Figure 5.5(a).

5.4 Further cascades of synchrony changes

We observe that by introducing even higher order amplitude dependence in Ω than that in (5.20) such as

$$\Omega = \omega + \sigma \sin(k|z|^4), \quad (5.23)$$

even higher number of within-burst synchrony changes may be obtained. One such example is illustrated in the simulation in Figure 5.8. This simulation is based on the directly coupled system of Bautin bursters governed by system (5.6) with Ω defined as (5.23) for each burster. The parameters for all the realizations are $\kappa_1 = 0.001$, $\kappa_2 = 0.1$, $\omega = 0.001$, $\sigma = 5$, and $\eta = 0.001$. Low amplitude noises of order 10^{-6} are added to the fast subsystems. The values of k is varied from panel (a) to (d) as indicated. It is obvious that the number of synchrony changes

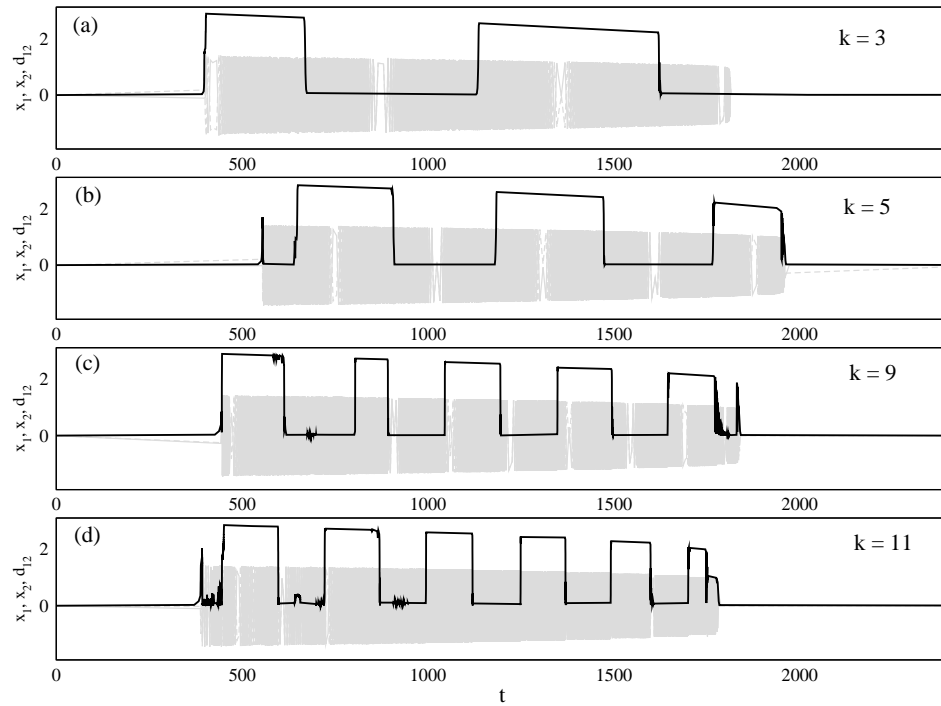


Figure 5.8: Simulation of the system two coupled Bautin elliptic bursters governed by the system (5.6) and (5.7) but with Ω for each burster defined by (5.23). The activity patterns for different values of k are shown. Note the increasing number of synchrony changes as k is increased from (a) to (d). Only one burst is shown and the pattern repeats each burst. The superimposed solid line indicates corresponding time series of d_{12} .

in this system increases dramatically with increasing k . Note at higher values of $k > 9$, the spike synchrony patterns develop irregular behaviour (shown in the corresponding traces of d_{12}) which eventually become highly irregular and lead to burst desynchronization between the coupled bursters. So, these results confirm the possibility of within-burst cascades of synchrony changes for robustly coupled Bautin elliptic bursters.

5.5 Synchrony changes with more general Ω

In this section we carry out an analysis of the within-burst synchrony changes for two coupled elliptic bursters involving more general nonisochronicity, i.e, $\Omega(|z|^2)$. We consider the coupled system (5.6) where $\Omega_j(|z_j|^2)$ is an amplitude dependent arbitrary function and the coupling is defined by K_j in the equation (5.7). For $n = 2$, the burst synchronized constrained system for two coupled burster system with $\Omega_j(|z_j|^2)$ may be written in polar its counterpart as following

$$\left. \begin{aligned} \dot{r}_1 &= u_1 r_1 + 2r_1^3 - r_1^5 + r_2 (\kappa_1 \cos(\theta_2 - \theta_1) - \kappa_2 \sin(\theta_2 - \theta_1)) \\ \dot{\theta}_1 &= \omega + \Omega(r_1^2) + \frac{r_2}{r_1} (\kappa_1 \sin(\theta_2 - \theta_1) + \kappa_2 \cos(\theta_2 - \theta_1)) \\ \dot{r}_2 &= u_2 r_2 + 2r_2^3 - r_2^5 + r_1 (\kappa_1 \cos(\theta_1 - \theta_2) - \kappa_2 \sin(\theta_1 - \theta_2)) \\ \dot{\theta}_2 &= \omega + \Omega(r_2^2) + \frac{r_1}{r_2} (\kappa_1 \sin(\theta_1 - \theta_2) + \kappa_2 \cos(\theta_1 - \theta_2)) \\ \dot{u} &= \eta \left(a - \frac{1}{2}(r_1^2 + r_2^2) \right). \end{aligned} \right\} \quad (5.24)$$

Note that the nonisochronous terms in the above system are in general form.

Now applying transformation (5.11) on system (5.24), we obtain

$$\left. \begin{aligned} \dot{r}_l &= u r_l + 2r_l^3 + 6r_l r_t^2 - r_l^5 - 10r_l^3 r_t^2 - 5r_l r_t^4 + \kappa_1 r_l \cos \phi - \kappa_2 r_t \sin \phi \\ \dot{r}_t &= u r_t + 6r_t^2 r_l + 2r_t^3 - 5r_t^4 r_l - 10r_t^2 r_l^3 - r_t^5 - \kappa_1 r_t \cos \phi + \kappa_2 r_l \sin \phi \\ \dot{\phi} &= \Omega((r_l + r_t)^2) - \Omega((r_l - r_t)^2) - 2\kappa_1 \frac{(r_l^2 + r_t^2)}{r_l^2 - r_t^2} \sin \phi - 4\kappa_2 \frac{r_l r_t}{r_l^2 - r_t^2} \cos \phi \\ \dot{u} &= \eta (a - (r_l^2 + r_t^2)). \end{aligned} \right\} \quad (5.25)$$

Now we analyze the stability of the fast subsystem of (5.25) as before by considering slow-fast decomposition by setting $\eta = 0$. Thereafter the Jacobian for the fast

subsystem of (5.25) at the inphase solution ($r_t = \phi = 0, r_l = r$) is a block diagonal with a single real eigenvalue and a block

$$J_{in} = \begin{pmatrix} u + 6r^2 - 5r^4 - \kappa_1 & \kappa_2 r \\ 4r\Omega' - \frac{4\kappa_2}{r} & -2\kappa_1 \end{pmatrix} \quad (5.26)$$

where $\Omega' = \frac{\partial\Omega}{\partial r}$. The eigenvalues of (5.30) can be determined by examining the trace and the determinant of the matrix. The determinant of (5.30) is

$$\det(J_{in}) = -2\kappa_1(u + 6r^2 - 5r^4) - 4\kappa_2\Omega'r^2 + 2\kappa_1^2 + 4\kappa_2^2. \quad (5.27)$$

For simplicity we consider as before the special case when $\kappa_1 = 0$ and $\kappa_2 \ll 1$. As observed before $tr(J_{in})$ is negative because of the stable periodic solution of the system and for weak coupling $(tr(J_{in}))^2 > 4\det(J_{in})$. In order to explain the within-burst synchrony changes, we may write (5.27) to first order in κ_2 and by setting $\kappa_1 = 0$ as

$$\det(J_{in}) = -4\Omega'r^2\kappa_2 + O(\kappa_2^2). \quad (5.28)$$

It is obvious from (5.28), the change in sign of $\det(J_{in})$ and consequently the synchrony changes and their stability depends on that of Ω' ; the system will have stable node for $\det(J_{in}) > 0$ and saddle for $\det(J_{in}) < 0$. Moreover, the approximate values of r where the bifurcation take place can be determined by solving $\det(J_{in}) = 0$, or

$$\Omega'r_{in}^2\kappa_2 - \kappa_2^2 = 0. \quad (5.29)$$

Similarly for antiphase solutions where $r_t = 0, \phi = \pi$ and $t_l = r$, similar analysis yields

$$J_{anti} = \begin{pmatrix} u + 6r^2 - 5r^4 - \kappa_1 & -\kappa_2 r \\ 4r\Omega' + \frac{4\kappa_2}{r} & -2\kappa_1 \end{pmatrix} \quad (5.30)$$

and the determinant

$$\det(J_{anti}) = -2\kappa_1(u + 6r^2 - 5r^4) + 4\kappa_2\Omega'r^2 - 2\kappa_1^2 - 4\kappa_2^2. \quad (5.31)$$

Again for the special case $\kappa_1 = 0$ and $\kappa_2 \ll 1$

$$\det(J_{in}) = 4\Omega'r^2\kappa_2 + O(\kappa_2^2). \quad (5.32)$$

here the change in stability of the solutions depends on the sign of Ω' and the bifurcation values of r can be found by solving

$$\Omega' r_{in}^2 \kappa_2 + \kappa_2^2 = 0 \quad (5.33)$$

Hence, a similar analysis for within-burst synchrony changes can be done for more general $\Omega(|z|^2)$ and it is obvious that the change in stability of inphase and antiphase solutions depends on sign of Ω' as was shown with especial cases in the previous sections.

Chapter 6

Within-burst synchrony changes in higher dimensions

In Chapters 3, 4 and 5 we explored within-burst synchrony changes for a system of coupled Bautin bursters consisting of two cells for different isochronous conditions. In this chapter we briefly investigate within-burst synchrony changes for a system of higher dimension. Particularly we study a coupled system of three Bautin bursters. In this study we consider the non-isochronous case where the fast spikes undergo frequency transition characterized by the parameter r_m as in (3.12) along the burst period. We consider all-to-all direct linear coupling as in Section 3.4. We also investigate the phenomenon for a system of four Bautin elliptic bursters.

6.1 Three-coupled elliptic bursters system

In order to demonstrate within-burst synchrony changes in a three-coupled elliptic burster system, we use the model (5.6) with

$$\Omega_j = \omega + \frac{1}{2}\sigma r_m^2 r_j^2 - \frac{1}{6}\sigma r_j^4 \quad (6.1)$$

where $j = 1, \dots, n$, where n is the number of bursting cells. The fast spikes in the bursters therefore have one frequency transition characterized by position r_m along the burst profile. In fact this is what was studied in Chapters 3 and 4 for two coupled Bautin elliptic bursters. Now, the Euclidean of the governing system

may be written as

$$\left. \begin{aligned} \dot{x}_j &= (u_j x_j - \omega y_j) + \left(2x_j - \frac{\sigma r_m^2 r_j^2}{2} y_j\right) (x_j^2 + y_j^2) \\ &\quad + \left(-x_j + \frac{\sigma r_m^2}{4} y_j\right) (x_j^2 + y_j^2)^2 + \sum_{k \neq j} (\kappa_1 x_k - \kappa_2 y_k) \\ \dot{y}_j &= (\omega x_j + u_j y_j) + \left(\frac{\sigma r_m^2}{2} x_j + 2y_j\right) (x_j^2 + y_j^2) \\ &\quad + \left(-y_j - \frac{\sigma r_m^2}{4} x_j\right) (x_j^2 + y_j^2)^2 + \sum_{k \neq j} (\kappa_2 x_k + \kappa_1 y_k) \\ \dot{u}_j &= \eta(a - x_j^2 - y_j^2) \end{aligned} \right\} \quad (6.2)$$

where $j, k = 1, 2, 3$.

It is obvious from Figures 6.1 and 6.2 that system of three elliptic bursters can demonstrate within-burst synchrony changes behaviour similar to two-elliptic burster system (Figures 3.9 and 3.10).

Figure 6.1 shows the simulation of the system (6.2) with parameters $\omega = 0.1$, $r_m = 1.35$, $\sigma = 5$, $\kappa_1 = 0.001$, $\kappa_2 = 0.2$. In addition, noise of amplitude 10^{-5} was added to the fast subsystem of each burster. The simulation was done with XPPAUT [33] with adaptive Runge-Kutta integrator. This simulation shows the similar spontaneous within-burst synchrony changes in this even higher dimensional system. The three bursts are synchronized and the fast spiking oscillations are inphase at the beginning within the burst, but change to antiphase as the frequency of the fast spiking shifts (6.1). The idea of antiphase in the case of three bursters is characterized by a phase shift of $\frac{2\pi}{3}$ relative to each other. The inset in the top panel shows a detail of the activity patterns, x_1 , x_2 , and x_3 , where the transition takes place. The middle panel shows the corresponding slow variables, u_1 , u_2 and u_3 , whose synchrony implies burst synchronization of the dynamics. The third panel shows plots of d_{12} , d_{13} , and d_{23} that must be zero for inphase synchronization, where

$$d_{ij} = \sqrt{(x_i - x_j)^2 + (y_i - y_j)^2 + (u_i - u_j)^2}, \quad (6.3)$$

with $i, j = 1, 2, 3$.

Secondly, Figure 6.2 shows similar within-burst synchrony changes for three-burster system. The governing system and parameters of this simulation are same

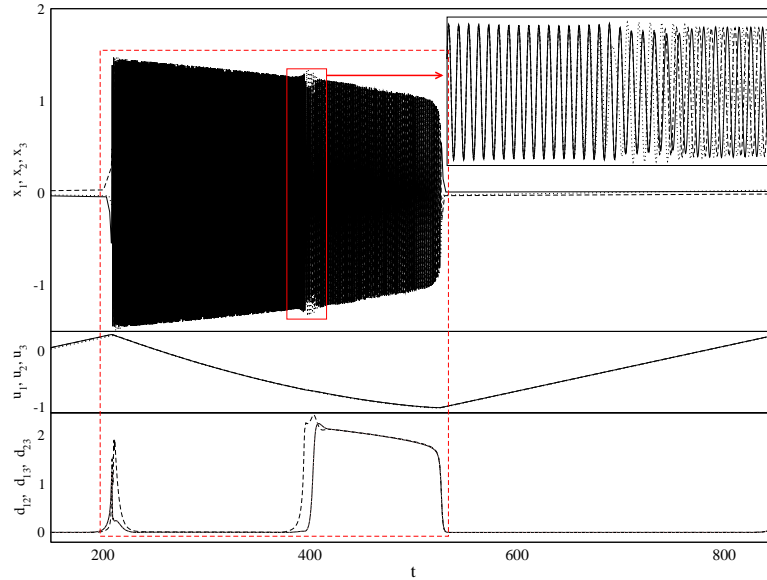


Figure 6.1: Within-burst synchrony changes in three Bautin elliptic bursters governed by (6.2). Here within-burst synchrony changes from stable inphase to stable antiphase. The dashed box shows the activity pattern of one burst, the burst repeats periodically and the within-burst synchrony change appears during each burst. The parameters of the simulation are $\omega = 0.1$, $r_m = 1.35$, $\sigma = 5$, $\kappa_1 = 0.001$, $\kappa_2 = 0.2$. Noise of amplitude 10^{-5} was added to the fast subsystem of each burster. In the figure, the three bursters are burst synchronized (middle) and the spikes in the bursts are inphase at the beginning of the burst but change to antiphase near the middle of the burst. The activities, x_1, x_2, x_3 , of the three different bursters are shown in solid, dashed and dotted lines, respectively. The inset shows the region of transition. The bottom panel shows the corresponding pattern of d_{12} , d_{13} and d_{23} implying spike synchrony behaviour.

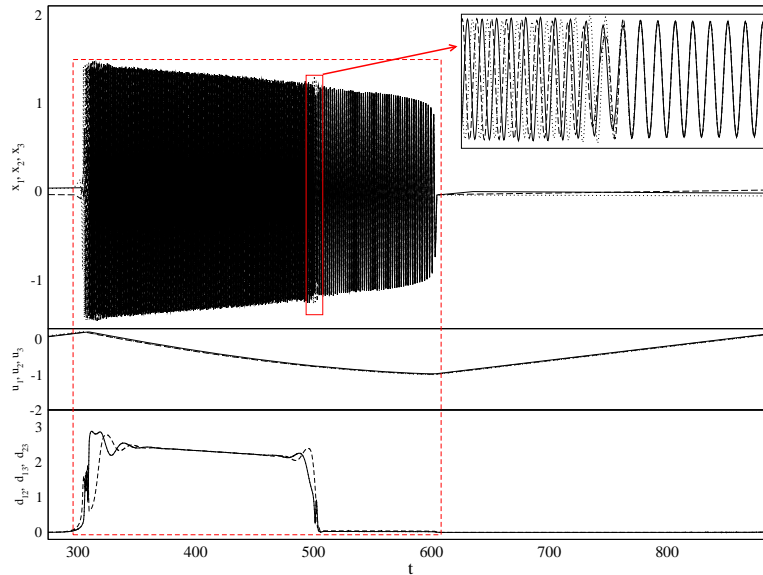


Figure 6.2: Another example of within-burst synchrony changes for three-Bautin elliptic bursters. The parameters and details of this simulation are same as those of Figure 6.1 except $\kappa_1 = -0.001$, $\kappa_2 = -0.2$. For this different coupling we can see the spikes are antiphase to each other at the beginning but changes to inphase past the frequency transition point at $r_m = 1.35$ along the burst profile.

as those for Figure 6.1 except $\kappa_1 = -0.001$, $\kappa_2 = -0.2$. This causes the spike oscillations in the synchronized bursts to have antiphase synchronization at the beginning which soon changes to inphase past the frequency shift towards the end of the burst. Hence, these examples establish the within-burst synchrony changes in the higher-dimensional system of coupled Bautin elliptic bursters.

6.2 Synchrony bifurcation for fast subsystem of three-Bautin burster system

In this section we carry out bifurcation analysis of the fast subsystem of (6.2) for three-Bautin burster system by continuing the transverse phase variables of the oscillations. This is done by studying a burst-synchronized constrained model for the dynamics. In the polar coordinate the system (3.12) for $n = 3$ may be recast as

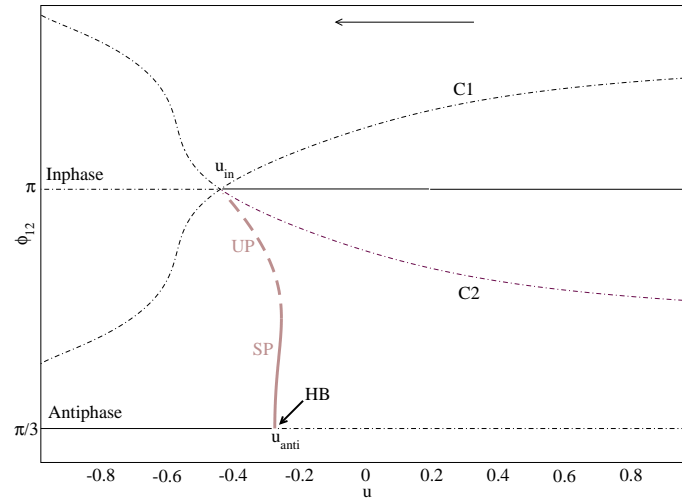


Figure 6.3: Bifurcation diagram of ϕ_{12} (defined in (6.5)) against u for three coupled bursters. The parameters are $\kappa_1 = 0.001$, $\kappa_2 = 0.2$, $\sigma = 5$ and $r_m = 1.35$. Here, S(U)FP=stable (unstable) fixed point, S(U)P=stable (unstable) period and HB=Andronov-Hopf bifurcation point. u_{in} and u_{anti} , the inphase and antiphase bifurcation points, respectively, are shown with arrows. The big arrow on top shows the direction of change of u . The branches C1 and C2 are unstable solutions where spikes from two bursters are synchronized while those from the third are not. The solid (dash-dotted) lines represent (unstable) stable solutions.

$$\left. \begin{aligned}
 \dot{r}_1 &= u_1 r_1 + 2r_1^3 - r_1^5 + \kappa_1(r_2 \cos \phi_{12} + r_3 \cos \phi_{13}) \\
 &\quad + \kappa_2(r_2 \sin \phi_{12} + r_3 \sin \phi_{13}) \\
 \dot{\theta}_1 &= \omega + \frac{1}{2}\sigma r_m^2 r_1^2 - \frac{1}{4}\sigma r_1^4 - \kappa_1 \left(\frac{r_2}{r_1} \sin \phi_{12} + \frac{r_3}{r_1} \sin \phi_{13} \right) \\
 &\quad + \kappa_2 \left(\frac{r_2}{r_1} \cos \phi_{12} + \frac{r_3}{r_1} \cos \phi_{13} \right) \\
 \dot{u}_1 &= \eta(a - r_1^2) \\
 \dot{r}_2 &= u_2 r_2 + 2r_2^3 - r_2^5 + \kappa_1(r_1 \cos \phi_{12} + r_3 \cos(\phi_{12} - \phi_{13})) \\
 &\quad - \kappa_2(r_1 \sin \phi_{12} + r_3 \sin(\phi_{12} - \phi_{13})) \\
 \dot{\theta}_2 &= \omega + \frac{1}{2}\sigma r_m^2 r_2^2 - \frac{1}{4}\sigma r_2^4 + \kappa_1 \left(\frac{r_1}{r_2} \sin \phi_{12} + \frac{r_3}{r_2} \sin(\phi_{12} - \phi_{13}) \right) \\
 &\quad + \kappa_2 \left(\frac{r_1}{r_2} \cos \phi_{12} + \frac{r_3}{r_2} \cos(\phi_{12} - \phi_{13}) \right) \\
 \dot{u}_2 &= \eta(a - r_2^2) \\
 \dot{r}_3 &= u_3 r_3 + 2r_3^3 - r_3^5 + \kappa_1(r_1 \cos \phi_{13} + r_2 \cos(\phi_{12} - \phi_{13})) \\
 &\quad - \kappa_2(r_1 \sin \phi_{13} - r_2 \sin(\phi_{12} - \phi_{13})) \\
 \dot{\theta}_3 &= \omega + \frac{1}{2}\sigma r_m^2 r_3^2 - \frac{1}{4}\sigma r_3^4 + \kappa_1 \left(\frac{r_1}{r_3} \sin \phi_{13} + \frac{r_2}{r_3} \sin(\phi_{13} - \phi_{12}) \right) \\
 &\quad + \kappa_2 \left(\frac{r_1}{r_3} \cos \phi_{13} + \frac{r_2}{r_3} \cos(\phi_{13} - \phi_{12}) \right) \\
 \dot{u}_3 &= \eta(a - r_3^2).
 \end{aligned} \right\} \quad (6.4)$$

Now defining transverse phase variables ϕ_{12} and ϕ_{13} as

$$\left. \begin{aligned}
 \phi_{12} &= \theta_1 + \theta_2 \\
 \phi_{13} &= \theta_1 - \theta_3,
 \end{aligned} \right\} \quad (6.5)$$

and letting $u_1 = u_2 = u_3 = u$, we obtain the reduced burst-synchronized model:

$$\left. \begin{aligned}
 \dot{r}_1 &= ur_1 + 2r_1^3 - r_1^5 + \kappa_1(r_2 \cos \phi_{12} + r_3 \cos \phi_{13}) \\
 &\quad + \kappa_2(r_2 \sin \phi_{12} + r_3 \sin \phi_{13}) \\
 \dot{r}_2 &= ur_2 + 2r_2^3 - r_2^5 + \kappa_1(r_1 \cos \phi_{12} + r_3 \cos(\phi_{12} - \phi_{13})) \\
 &\quad - \kappa_2(r_1 \sin \phi_{12} + r_3 \sin(\phi_{12} - \phi_{13})) \\
 \dot{r}_3 &= ur_3 + 2r_3^3 - r_3^5 + \kappa_1(r_1 \cos \phi_{13} + r_2 \cos(\phi_{12} - \phi_{13})) \\
 &\quad - \kappa_2(r_1 \sin \phi_{13} - r_2 \sin(\phi_{12} - \phi_{13})) \\
 \dot{\phi}_{12} &= \frac{1}{2}\sigma r_m^2(r_1^2 - r_2^2) - \frac{1}{4}\sigma(r_1^4 - r_2^4) \\
 &\quad - \kappa_1 \left(\left(\frac{r_2}{r_1} + \frac{r_1}{r_2} \right) \sin \phi_{12} + \frac{r_3}{r_1} \sin \phi_{13} + \frac{r_3}{r_2} \sin(\phi_{12} - \phi_{13}) \right) \\
 &\quad + \kappa_2 \left(\left(\frac{r_2}{r_1} - \frac{r_1}{r_2} \right) \cos \phi_{12} + \frac{r_3}{r_1} \cos \phi_{13} - \frac{r_3}{r_2} \cos(\phi_{12} - \phi_{13}) \right) \\
 \dot{\phi}_{13} &= \frac{1}{2}\sigma r_m^2(r_1^2 - r_3^2) - \frac{1}{4}\sigma(r_1^4 - r_3^4) \\
 &\quad - \kappa_1 \left(\frac{r_2}{r_1} \sin \phi_{12} + \left(\frac{r_3}{r_1} + \frac{r_1}{r_3} \right) \sin \phi_{13} + \frac{r_2}{r_3} \sin(\phi_{13} - \phi_{12}) \right) \\
 &\quad + \kappa_2 \left(\frac{r_2}{r_1} \cos \phi_{12} + \left(\frac{r_3}{r_1} - \frac{r_1}{r_3} \right) \cos \phi_{13} - \frac{r_2}{r_3} \cos(\phi_{13} - \phi_{12}) \right) \\
 \dot{u} &= \eta \left(a - \frac{1}{3}(r_1^2 + r_2^2 + r_3^2) \right).
 \end{aligned} \right\} \quad (6.6)$$

Note in this system ϕ_{23} was eliminated using the symmetry $\phi_{23} = \theta_2 - \theta_3 = \theta_2 - \theta_1 + \theta_1 - \theta_3 = \phi_{13} - \phi_{12}$. Figure 6.3 shows the bifurcation diagram of ϕ_{12} against u . The stable inphase solutions at the beginning and stable antiphase solutions at the end of the burst can be seen. Note the Andronov-Hopf bifurcation point (HB) on the antiphase solution curve generates stable periodic (SP) orbit which in reality can not be viewed in the simulation as the system ‘sticks’ to this stable inphase solution branch even after passing an inphase bifurcation point (u_{in}) and thus the stable periodic branch is not observed. One interesting feature of this bifurcation is the two additional branches labeled C1 and C2. These imply the other possible solutions of the system which include two spike oscillations are synchronized while the third one is not synchronized with them. Note both C1 and C2 are unstable and symmetric. Figure 6.5 depicts the phase-space dynamics of one of these branches and note the dynamics will be similar for other branch due to symmetry. The insets

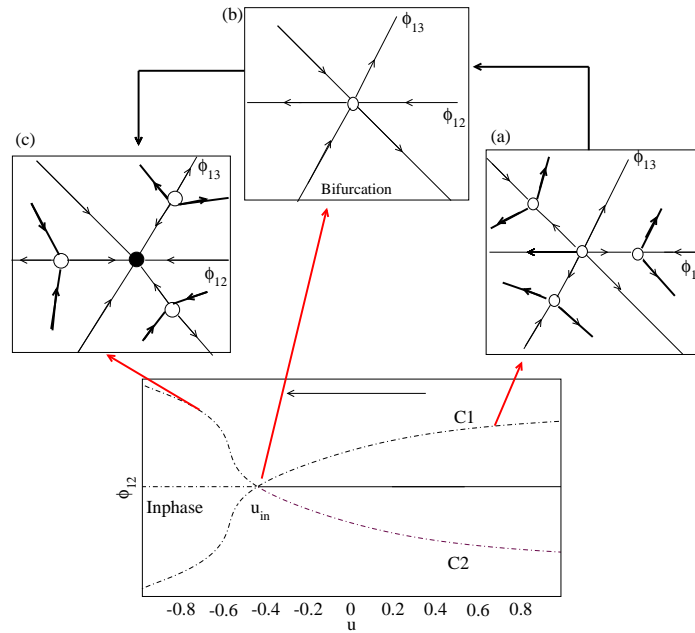


Figure 6.4: The phase-space dynamics in the $\phi_{12}\phi_{13}$ -space of branches C1 and C2 of bifurcation diagram 6.3. The (un)filled circles indicate (un)stable nodes in the phase-space (after [6]).

(a)–(c) illustrates the phase-space diagram as the system transverses bifurcation point. It is clear that these unstable branches are amenable to continuation as there are stable directions exist when $\phi_{12} \neq 0$ and $\phi_{13} \neq 0$. An interesting global bifurcation scenerio is shown in the figure 6.5. One dynamically invariant triangle is shown and at the bifurcation point there is a connection in the lattice between adjacent inphase solutions. The local behaviour near an inphase solution (one of the vertices) is shown in figure 6.5. We can clearly observe in the right triangle the emergence of the periodic orbit created by the global connection [6]).

It is difficult to do a complete stability analysis for synchrony dynamics for three-Bautin burster system. Nevertheless, a simple analysis may be done based on the reduced model (6.6). We present a outline of calculating the bifurcation point, particularly the inphase bifurcation point in the spirit of Chapter 5 where similar calculation was conducted in details for two Bautin bursters. In order to

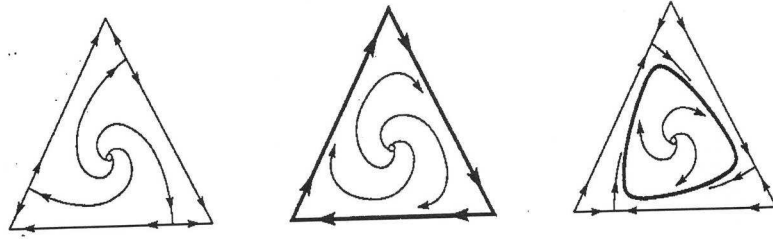


Figure 6.5: Global bifurcation of the three-bautin burster system. One dynamically invariant triangle is shown. The local behaviour near inphase solution (one of the vertices) is shown in figure 6.3. The middle triangle shows the dynamics at the bifurcation point (figure 6.3(b)) and the right triangle shows the emergent periodic orbit via global connection [6].

do the analysis, we firstly consider the following changes in the radial coordinates:

$$\left. \begin{aligned} r_1 &= r_l + \frac{2}{3}(r_{12} + r_{13}) \\ r_2 &= r_l - \frac{2}{3}(2r_{12} - r_{13}) \\ r_3 &= r_l + \frac{2}{3}(r_{12} - 2r_{13}) \end{aligned} \right\} \quad (6.7)$$

here, $r_l = \frac{r_1+r_2+r_3}{3}$, $r_{12} = \frac{r_1-r_2}{2}$, and $r_{13} = \frac{r_1-r_3}{2}$. Now, incorporating the change in coordinates (6.7) together with changed phase variables (6.5) we may obtain a system of burst-synchronized constrained system. The system may be written in the following functional form

$$\left. \begin{aligned} \dot{r}_l &= f_1(r_l, r_{12}, r_{13}, \phi_{12}, \phi_{13}) \\ \dot{r}_{12} &= f_2(r_l, r_{12}, r_{13}, \phi_{12}, \phi_{13}) \\ \dot{r}_{13} &= f_3(r_l, r_{12}, r_{13}, \phi_{12}, \phi_{13}) \\ \dot{\phi}_{12} &= f_4(r_l, r_{12}, r_{13}, \phi_{12}, \phi_{13}) \\ \dot{\phi}_{13} &= f_5(r_l, r_{12}, r_{13}, \phi_{12}, \phi_{13}) \\ \dot{u} &= \eta g(r_l, r_{12}, r_{13}, \phi_{12}, \phi_{13}). \end{aligned} \right\} \quad (6.8)$$

Here, f_k and g are the vector fields. Now in order to investigate the fast dynamics of the system we consider η as a singular perturbation parameter so that $u = \text{constant}$ in the dynamics and the dynamics is only governed by the fast spiking activity. For, $r_{12} = 0$ and $r_{13} = 0$, we write $r_l = r$ as the stable nontrivial solution of (6.8) in

appropriate subspace given by (4.7) corresponding to bursting behaviour. In this analysis we only consider the inphase solution which implies $r_{12} = r_{13} = \phi_{12} = \phi_{13} = 0$ and $r_l = r$, where $r > 0$ is a solution of (4.8). As for the Jacobian for the fast subsystem we consider the following block

$$J = \begin{pmatrix} \frac{\partial f_2}{\partial r_{12}} & \frac{\partial f_2}{\partial r_{13}} & \frac{\partial f_2}{\partial \phi_{12}} & \frac{\partial f_2}{\partial \phi_{13}} \\ \frac{\partial f_3}{\partial r_{12}} & \frac{\partial f_3}{\partial r_{13}} & \frac{\partial f_3}{\partial \phi_{12}} & \frac{\partial f_3}{\partial \phi_{13}} \\ \frac{\partial f_4}{\partial r_{12}} & \frac{\partial f_4}{\partial r_{13}} & \frac{\partial f_4}{\partial \phi_{12}} & \frac{\partial f_4}{\partial \phi_{13}} \\ \frac{\partial f_5}{\partial r_{12}} & \frac{\partial f_5}{\partial r_{13}} & \frac{\partial f_5}{\partial \phi_{12}} & \frac{\partial f_5}{\partial \phi_{13}} \end{pmatrix}. \quad (6.9)$$

Thus, the Jacobian at the inphase solution is block diagonal with one single real eigenvalue and a block (6.9):

$$J_{in} = \begin{pmatrix} 2u + 12r^2 - 10r^4 - 2\kappa_1 & 0 & 3\kappa_2 r & 0 \\ 0 & 2u + 12r^2 - 10r^4 - 2\kappa_1 & 0 & 3\kappa_2 r \\ 2\sigma r_m^2 - 2\sigma r^3 - \frac{6\kappa_2}{r} & 0 & -3\kappa_1 & 0 \\ 0 & 2\sigma r_m^2 - 2\sigma r^3 - \frac{6\kappa_2}{r} & 0 & -3\kappa_1 \end{pmatrix}. \quad (6.10)$$

The real eigenvalues can assumed negative because of the solution of (4.7). Note stability of this fast subsystem may be investigated by determining the determinant of (6.10) and bifurcation information can be found by equating the determinant with zero. The determinant of (6.10) is

$$\det(J_{in}) = 36 \left(-\kappa_1 u - (6\kappa_1 + \kappa_2 \sigma r_m^2) r^2 + (5\kappa_1 + \kappa_2 \sigma) r^4 + \kappa_1^2 + 3\kappa_2^2 \right)^2. \quad (6.11)$$

Together with (4.8), $\det(J_{in}) = 0$ or

$$-\kappa_1 u - (6\kappa_1 + \kappa_2 \sigma r_m^2) r^2 + (5\kappa_1 + \kappa_2 \sigma) r^4 + \kappa_1^2 + 3\kappa_2^2 = 0. \quad (6.12)$$

may give bifurcation value for amplitude or r_{in} and corresponding bifurcation value for slow variable or u_{in} (Figure 6.3) with appropriate approximation similar to Section 4.1. We present analytical expressions for r_{in} and u_{in} for a special case $\kappa_1 = 0$. Solving (6.12) with $\kappa_1 = 0$ gives

$$r_{in} = r_m \left(1 - \frac{3\kappa_2}{2\sigma r_m^4} \right) + O(\kappa_2^2). \quad (6.13)$$

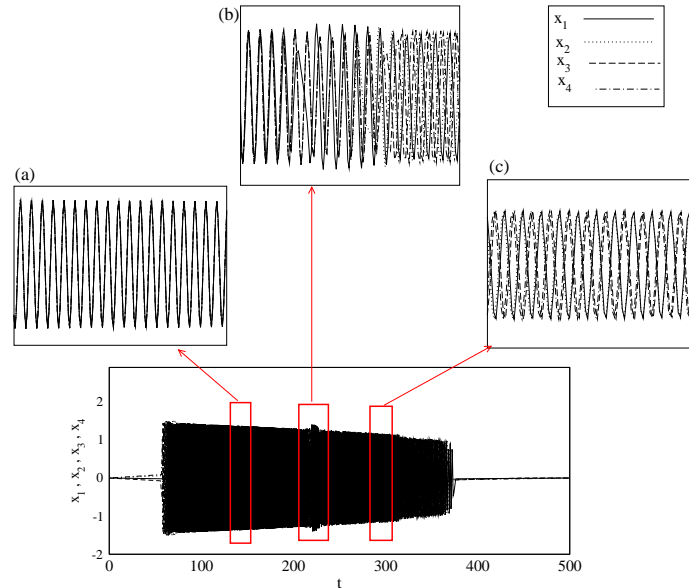


Figure 6.6: Within-burst synchrony changes for four-coupled Bautin elliptic burster system. The governing system for the simulation is same as Figures 6.1 and 6.2. The parameters of the simulation: $\kappa_1 = 0.001$, $\kappa_2 = 0.2$, $\sigma = 5$, $\eta = 0.005$, $r_m = 1.35$, $\omega = 0.0001$. Noise of amplitude of order 10^{-5} was added to all fast subsystems. Bottom panel shows the activities, x_j , of the four bursters; the four bursters are burst synchronized. The insets (a)-(c) show different blown-up sections of the spiking patterns inside the synchronized bursts. It is clear the spikes start off inphase (a) then change in region (b) to an asynchronous pattern (c).

Because r depends on u via (4.8), the corresponding bifurcation points for inphase oscillations can be derived from (4.18) and (4.8) for the special case $\kappa_1 = 0$ as

$$u_{in} = \frac{1}{2}r_m^2(r_m^2 - 4) + \frac{3\kappa_2}{\sigma r_m^2}(2 - r_m^2) + O(\kappa_2^2), \quad (6.14)$$

Note that a more general analysis of these bifurcation points for non-zero κ_1 and κ_2 can be undertaken by examining roots of (6.12).

6.3 Four-coupled Bautin elliptic burster system

In this section we investigate within burst synchrony changes numerically for a system comprised with four Bautin bursters. The governing system is similar to (3.12) with non-isochronous condition (6.1) for $j = 1, 2, 3, 4$. Figure 6.6 illustrates

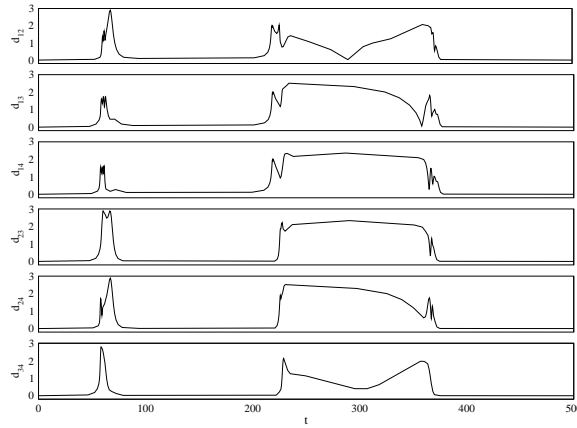


Figure 6.7: The timeseries of d_{ij} (6.3) for four-coupled elliptic burster system. The d_{ij} 's correspond to the single snap of the synchronized burst of the four cells shown in Figure 6.6. Here the spikes start off inphase (zero d_{ij} 's) but changes to asynchronous patterns with each other. Note the bumps are irregular in the profile (nonzero d_{ij} 's) which indicate some drift of asynchronous patterns between the spikes of two bursters.

the result of simulation for four-coupled Bautin burster system. The bottom panel shows a selected burst pattern where activities of the four bursters are superimposed like previous similar illustrations; the pattern repeats with bursts. The parameters are $\kappa_1 = 0.001$, $\kappa_2 = 0.2$, $\sigma = 5$, $\eta = 0.005$, $r_m = 1.35$, $\omega = 0.0001$ and noise of amplitude of order 10^{-5} was added to the fast subsystems of each burster. The simulation was done with XPPAUT [33] with Runge-Kutta integrator. The different synchrony patterns involving the fast oscillation within the burst can be seen in the blown up sections of the bursts from (a) to (c). Panel (a) shows the synchrony pattern at the beginning of the burst, (b) shows the transition and (c) shows the changed synchrony pattern. It is clear that the spikes are inphase to begin with but changes to asynchronous patterns towards the end. Note in the asynchronous patterns the spikes are not antiphase to each other, rather more complicated locked patterns emerge. Figure 6.7 shows d_{ij} 's of the oscillations corresponding to the burst in Figure 6.6. The inphase synchrony is obvious, but there are irregular bumps of nonzero d_{ij} 's implying irregular synchrony patterns between the spikes. In the higher dimensional system as this, presumably, within-burst synchrony changes may involve complicated synchrony behaviour including

regular, quasiperiodic or irregular spike synchronization depending on the system parameters and initial condition.

Chapter 7

Delay induced within-burst synchrony changes

We showed in Chapters 2 and 5 that systems of coupled Bautin burster can demonstrate within-burst synchrony changes in more biological type coupling like gap-junction and synaptic. Note in all cases the coupling strength involves a real part κ_1 and an imaginary part κ_2 ; biologically the role of the imaginary part of the coupling κ_2 is not clear. In order to get closer to more biologically realistic coupling we investigate a system of bursters mutually coupled with a fixed delay and we look for the similar burst and spike synchrony dynamics. This is biologically more relevant in the sense that propagation delay in neuronal systems is unavoidable and arises from various spatial, temporal and chemical properties. For references of delay in neuronal systems we refer to [10, 125, 126, 17, 18, 14, 15, 97, 43, 44, 19], where effects of delay have been studied for coupled neuronal systems and their dynamical properties. These studies particularly focus on the intrinsic dynamics and synchronization of the interacting tonic spiking cells with delayed coupling.

The aim of this chapter is to present a mutually delay-coupled Bautin burster system and establish within-burst synchrony changes for a simple system containing two bursters. Later we study a pair of coupled conductance-based model of elliptic burster and find similar behaviour.

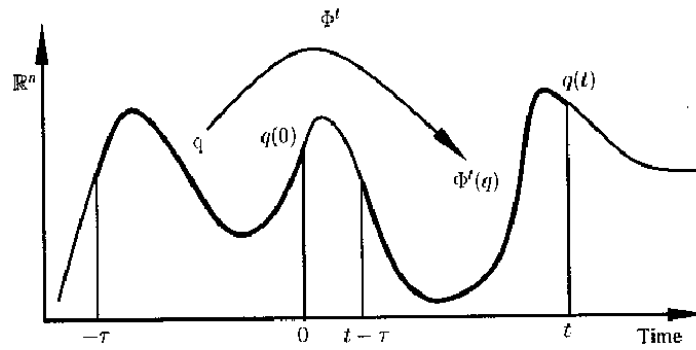


Figure 7.1: Sketch of the time evolution of a trajectory in phase space for delay differential equation (from [36]).

7.1 Basics of delay differential equations

It would be useful to recall some basic facts of delay differential equations (DDEs) before we study a coupled Bautin elliptic burster system involving delayed coupling. Generally, if the state of dynamical systems is known at a certain time t , then the future evolution is uniquely determined, i.e., the future course of evolution of a dynamical system depends on the initial conditions and dynamics can be described by differential equations. The initial condition is a point in the phase space of the system. However, the situation is different for systems with delay. In general form, a system with fixed delay can be written as

$$\frac{dx(t)}{dt} = F(x(t), x(t - \tau), p), \quad (7.1)$$

where $x \in \mathbb{R}^n$, the n -dimensional phase space, $p \in \mathbb{R}^m$, the parameter space, the function $F : \mathbb{R}^n \times \mathbb{R}^n \times \mathbb{R}^m \rightarrow \mathbb{R}^n$ is differentiable, $\tau \in \mathbb{R}$ is a single fixed delay. In this case unlike ordinary differential equation, the initial condition consists of a function segment on the interval $[t - \tau, t]$, which implies a system described by a DDE like (7.1) the time evolution in phase space does not only depend on the state at time t but also on the state at time $t - \tau$ in the past. We refer to [28, 46, 110] for a good exposition of DDEs and their mathematical properties. The phase space of ordinary differential equation are finite-dimensional, for example, system (6.2) for three-coupled Bautin burster has nine-dimensional phase space. But the

phase space of the DDEs is infinite-dimensional space continuous \mathcal{C} of the interval $[-\tau, 0]$ and a point $q \in \mathcal{C}$ is a function $q : [-\tau, 0] \rightarrow \mathbb{R}^n$. The right hand side of (7.1) defines the time evolution of the system uniquely and gives rise to an time evolution operator $\phi^t : \mathcal{C} \in \mathcal{C} \rightarrow \mathcal{C}$ which maps a function $q(t)$ at time t onto function $q(t + t')$ at the later time $t + t'$. This evolution is sketched in Figure 7.1.

A steady state for DDEs is point for which $q_0(t) = x_0$ for all time $t \in [-\tau, 0]$, where $x_0 \in \mathbb{R}^n$ for some fixed values $p' \in \mathbb{R}^m$ of the parameters, so that $F(q_0, q_0, p') = 0$ and $\phi^t(q_0) = q_0$ for all $t > 0$. The stability of q_0 can be determined by computing the root of the ‘characteristic equation’ which obtained by linearizing (7.1) around the steady state point q_0 :

$$DF(q_0, p')q = A_1(q_0, p')q(t) + A_2(q_0, p')q(t - \tau). \quad (7.2)$$

This generalized Jacobian of the DDE consists of two matrices.

$$\left. \begin{aligned} A_1(q_0, p') &= \left(\frac{\partial F(x(t), x(t - \tau), p)}{\partial x(t)} \right)_{(x_0, x_0, p')} \\ A_2(q_0, p') &= \left(\frac{\partial F(x(t), x(t - \tau), p)}{\partial x(t - \tau)} \right)_{(x_0, x_0, p')} \end{aligned} \right\} \quad (7.3)$$

Finally, the stability of the steady state of DDE (7.1) is given by roots of the characteristic equation $\det(\Delta(q_0, p', \lambda))$ with Δ is the $n \times n$ matrix

$$\Delta(q_0, p', \lambda) = \lambda I - A_1(q_0, p') - A_2(q_0, p')e^{-\lambda\tau}, \quad (7.4)$$

where I is the identity matrix. Obviously, the characteristic equation $\det(\Delta(q_0, p', \lambda))$ is of transcendental nature and therefore has infinitely many eigenvalues. However, they are discrete and there are typically only a finite number of unstable eigenvalues with $Re[\lambda] > 0$ [28]. For steady states the stability changes when these eigenvalues cross the imaginary axis in the complex plane. Consequently, there are two bifurcation situations can be noted: a saddle-node (fold) bifurcation where a single real eigenvalue goes through zero, and Andronov-Hopf bifurcation where a pair of complex conjugate eigenvalues move through the imaginary axis. Moreover, in projection onto the phase space \mathbb{R}^n a periodic orbit Γ of the DDE (7.1) is closed curve $q(t) = q(t + T)$, where $T > 0$ is the period of the orbit and Γ is such that

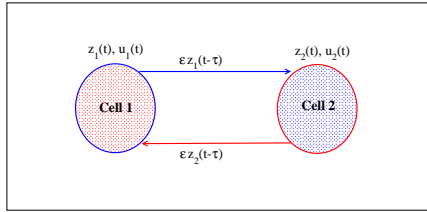


Figure 7.2: Cartoon of two mutually delay-coupled burster cells.

$\phi^T(q) = q$ for all $q \in \Gamma$. The stability of a periodic orbit Γ is given by its Floquet multipliers. There are three different bifurcation relating to the stability changes of periodic orbits [28]: a saddle-node of limit cycle bifurcation, where a single real Floquet multiplier goes through $+1$, a period doubling bifurcation, where a single Floquet multiplier goes through -1 , and a torus (Neimark-Sacker) bifurcation where a pair of complex conjugate Floquet multipliers goes through the unit circle.

Generally, the bifurcation analyses of DDEs like (7.1) involves solving transcendental equations, the respective conditions for steady states and periodic solutions must be solved along with the respective bifurcation condition. Numerical packages such as XPPAUT [33] can simulate DDEs like (7.1), but to follow branches of equilibria and periodic solutions of DDEs as parameters changed, the numerical continuation package DDE-BIFTOOL [32] is needed. DDE-BIFTOOL can compute stability information along solution branches and locate bifurcations.

In this chapter we only use XPPAUT in order to study a system of mutually delay-coupled Bautin burster with the aim of exploring numerically within-burst synchrony change behaviour in such systems.

7.2 Mutually delay-coupled Bautin bursters

We present a model of coupled Bautin elliptic bursters with a fixed delay in the coupling. The general form for n -burster system may be written as

$$\left. \begin{aligned} \dot{z}_j &= u_j z_j + 2z_j |z_j|^2 - z_j |z_j|^4 + bz_j |z_j|^6 + i\Omega_j z_j + \varepsilon \sum_{k=1}^n c_{jk} z_k(t - \tau) \\ \dot{u}_j &= \eta(a - |z_j|^2). \end{aligned} \right\} \quad (7.5)$$

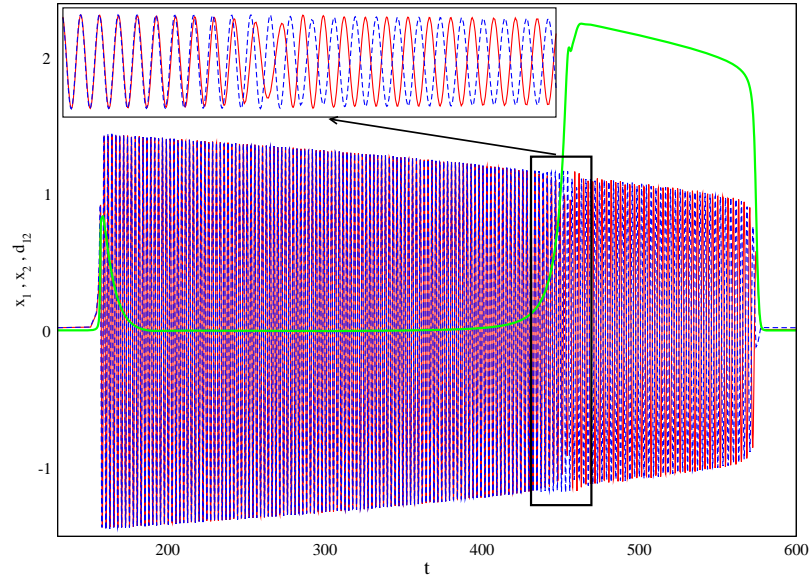


Figure 7.3: Within burst synchrony changes in the system of two mutually delay-coupled system governed by (7.5) and (7.6) for $j = 1, 2$. The parameters are $\varepsilon = 0.05$, $\omega = 0.001$, $\sigma = 3$, $\tau = 2$, $r_m = 1.35$ and $\eta = 0.004$. Low amplitude noise of order 10^{-6} is added to the fast subsystem of each system.

Here, $\tau \in \mathbb{R}$ is the fixed delay and $\varepsilon \in \mathbb{R}$ represents the coupling strength. Here we study a simple direct coupling case and $j = 1, \dots, n$. c_{jk} represents the connectivity matrix and in our study we consider all-to-all coupling, so $c_{jk} = 1$ and also we exclude any self-coupling, so $c_{jj} = 0$. A sketch of the system for two mutually delay-coupled bursters is shown in the figure 7.2. Note that interacting cells elicit a response into the other cell after delay characterized by τ . and also in (7.5) the coupling coefficient is real and so more realistic biologically. In the following we present simulation results of the system (7.5) for two mutually delay-coupled Bautin burster by considering different functions for (Ω) .

7.2.1 Within-burst synchrony changes via delay coupling

We summarize the simulation results for two-coupled Bautin burster governed by system (7.5) with Ω for each burster given by

$$\Omega = \omega + \frac{1}{2}\sigma r_m^2 |z|^2 - \frac{1}{4}\sigma |z|^4. \quad (7.6)$$

This implies that the fast spiking dynamics undergo a frequency transition characterized by r_m . Figure 7.3 summarizes the key observation. Here one burst pattern for each burster is shown superimposed and plotted for x_1 and x_2 of (7.5), where $z_j = x_j + iy_j$. The corresponding d_{12} pattern is also shown. Within-burst synchrony changes can be observed very clearly. The inset shows a blown-up section around the transition region indicated by the box. The pattern clearly shows that the spikes are inphase (flat $d_{12} = 0$) at the beginning of the burst and changes to antiphase (bumpy $d_{12} \neq 0$) towards the end of the burst period. This pattern is repeated in all bursts. The parameters in this simulation are $\varepsilon = 0.05$, $\omega = 0.001$, $\sigma = 3$, $\tau = 2$, $r_m = 1.35$ and $\eta = 0.004$. Moreover, low amplitude noise was added to the fast subsystem of each cell. This simulation shows the presence of within-burst synchrony changes behaviour in the coupled Bautin system with delay as found in ‘instantaneous’ coupling dynamics (Figures 3.9 and 3.10) where coupling coefficient has a complex part.

7.2.2 Within-burst cascade of synchrony changes via delay coupling

In this section we extend our study of mutually delay-coupled Bautin burster system to more complex Ω . We consider a transcendental form for Ω given by

$$\Omega = \omega + \sigma \sin(k|z|^2). \quad (7.7)$$

So, with (7.7) the system (7.5) incorporates multiple frequency transitions in the fast spiking dynamics. The simulation result has been summarized in Figure 7.4 for two different k . The figures show superimposed one burst (x_1 and x_2) pattern of the coupled bursters and the synchrony changes are demonstrated by corresponding d_{12} . In (a) the spikes are inphase implied by flat or zero d_{12} and this changes to antiphase implied by non-zero d_{12} . In (b) we observe cascades of spike synchrony changes. Clearly, the spikes are antiphase to begin with and changes to inphase and then again to antiphase for a higher value of k . Clearly this behaviour agrees with the observations in Chapter 5 for instantaneous coupling with complex coupling

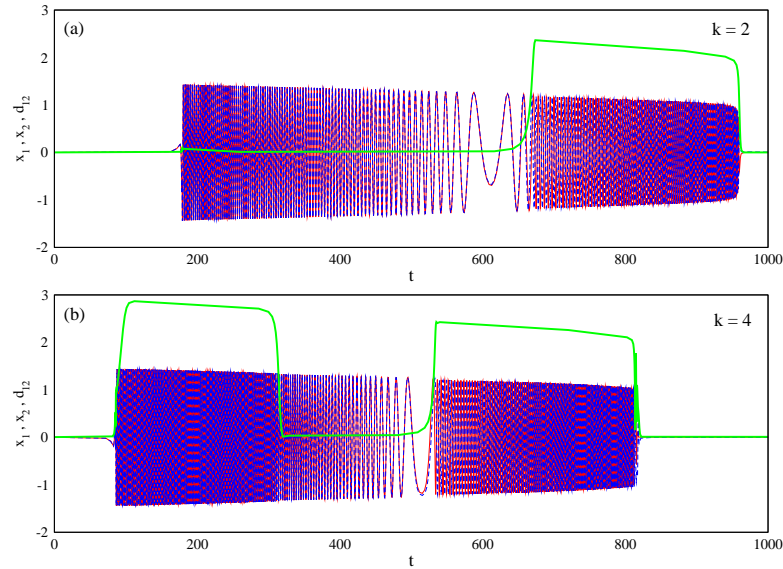


Figure 7.4: Within burst cascades of synchrony changes in the system of two mutually delay-coupled system governed by (7.5) and (7.7) with (a) $k = 2$ and (b) $k = 4$. The other parameters are $\varepsilon = 0.05$, $\omega = 0.001$, $\sigma = 3$, $\tau = 1$, and $\eta = 0.002$. Low amplitude noise of order 10^{-6} is added to the fast subsystems of the bursters.

coefficients.

7.3 Conductance-based bursting model

Given the existence of spontaneous within-burst synchrony changes in the model of coupled Bautin elliptic burster with delay coupling, we in this section explore similar behaviour in conductance-based model with biological coupling scheme in presence of delay. The model we study is a Morris-Lecar neuronal model [73] with an additional slow variable; the model has a calcium and potassium current. In addition, there are leak current and potassium-gated calcium current present in the system. In the bursting version of the model calcium current is considered as a slow varying current. The dynamics of the model is governed by the following dynamical system

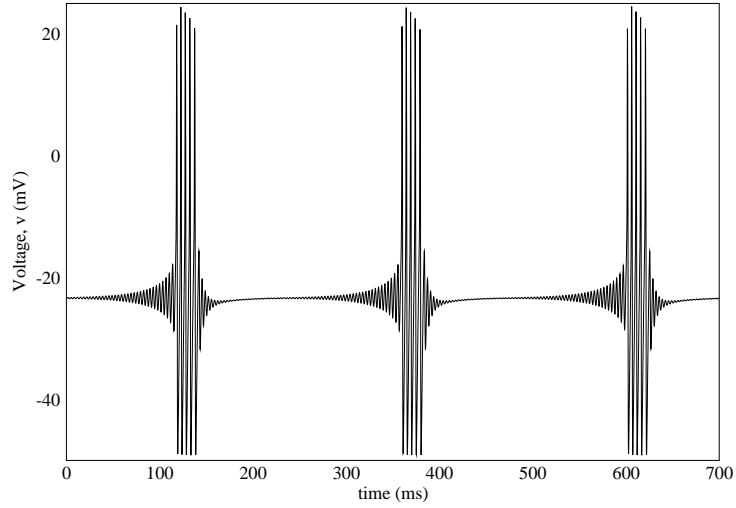


Figure 7.5: Elliptic bursting pattern generated by the system 7.8, 7.9. The parameters are $g_{ca} = 4.4$, $g_k = 8$, $g_l = 2$, $v_k = -84$, $v_l = -60$, $v_{ca} = 120$, $I = 120$, $g_{kca} = 0.75$, $\Phi = 1.2$, $\varepsilon = 0.04$, and $\mu = 0.016667$.

$$\left. \begin{aligned} \dot{v} &= -(g_{ca}m_{\infty}(v)(v - v_{ca}) + g_k w(v - v_k) \\ &\quad + g_l(v - v_l) + g_{kca}z(y)(v - v_k)) + I \\ \dot{w} &= \Phi(w_{\infty}(v) - w)/\tau(v) \\ \dot{y} &= \varepsilon(-\mu g_{ca}m_{\infty}(v)(v - v_{ca}) - y). \end{aligned} \right\} \quad (7.8)$$

The kinetics of the system are described by the following functions

$$\left. \begin{aligned} m_{\infty}(v) &= 0.5(1 + \tanh((v + 1.2)/18)) \\ w_{\infty}(v) &= 0.5(1 + \tanh((v - 2)/30)) \\ z(y) &= y/(1 + y) \\ \tau(v) &= \cosh((v - 2)/60). \end{aligned} \right\} \quad (7.9)$$

Here, (v, w) constitutes the fast subsystem and the y is the slow variable. Biologically v represents the action potential given in mV; w and y are the gating variables. As to the parameters of the system: g_{ca} , g_k , g_l and g_{kca} are conductances of calcium, potassium, leak and potassium-gated calcium currents, respectively; v_{ca} , v_k , v_l and v_{kca} are the reverse calcium, potassium, leak and potassium-gated calcium reverse potentials, respectively; I is the input current; Φ and μ are other parameters. The slowness of the gating variable y is characterized by small ε . Fig-

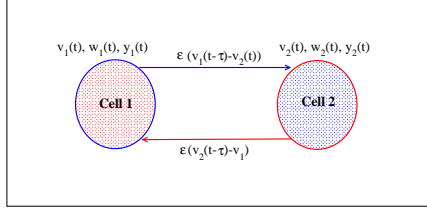


Figure 7.6: Cartoon of two mutually delay-coupled bursters of the conductance-based system.

Figure 7.5 demonstrates the time series of action potential of the system (7.8) with kinetics (7.9). The parameters in this simulation are $g_{ca} = 4.4$, $g_k = 8$, $g_l = 2$, $v_k = -84$, $v_l = -60$, $v_{ca} = 120$, $I = 120$, $g_{kca} = 0.75$, $\Phi = 1.2$, $\varepsilon = 0.04$, and $\mu = 0.016667$. This figure shows elliptic bursting patterns. Note burst patterns have spikes in the active phase whose amplitude change along on burst period and the passive phase has low amplitude subthreshold activity. By reducing the time scale ratio ε of fast activity to slow activity the length of the burst consequently the number of spikes in the burst can be increased and vice versa.

7.3.1 Mutually delay-coupled conductance-based bursting model

We present a system of coupled elliptic burst generating conductance-based neurons each of which is governed by the model (7.8) and (7.9). We consider a gap-junction coupling between the interacting system via the voltage variable. Additionally, we incorporate a delay in the coupling so that a response is elicited in a receiving neuron after a certain delay quantified by $\tau \in \mathbb{R}$. The full conductance-based mathematical model for n -burster system is the following

$$\left. \begin{aligned}
 \dot{v}_j &= -(g_{ca}m_\infty(v_j)(v_j - v_{ca}) + g_k w(v_j - v_k) + g_l(v_j - v_l) \\
 &\quad + g_{kca}z(y)(v_j - v_k)) + I + \kappa \sum_{k \neq j} c_{jk}(v_k(t - \tau) - v_j) \\
 \dot{w}_j &= \Phi(w_\infty(v_j) - w_j) / \tau(v_j) \\
 \dot{y}_j &= \varepsilon(-\mu g_{ca}m_\infty(v_j)(v_j - v_{ca}) - y_j)
 \end{aligned} \right\} \quad (7.10)$$

and the corresponding kinetics are

$$\left. \begin{aligned} m_{\infty}(v_j) &= 0.5 (1 + \tanh((v_j + 1.2)/18)) \\ w_{\infty}(v_j) &= 0.5 (1 + \tanh((v_j - 2)/30)) \\ z(y_j) &= y_j/(1 + y_j) \\ \tau(v_j) &= \cosh((v_j - 2)/60). \end{aligned} \right\} \quad (7.11)$$

Here, $j, k = 1, \dots, n$ and $j \neq k$. We consider $c_{jk} = 1$ and exclude any self-coupling ($c_{jj} = 0$). Figure 7.6 shows a sketch of a pair of elliptic bursters governed by (7.10) and (7.11) with $n = 2$. Here, κ represents the coupling strength between the neurons and τ is the amount of delay in the coupling.

7.3.2 Within-burst synchrony changes in conductance-based model

Figure 7.7 shows a simulation of system (7.10) and (7.11) for a pair of mutually delay-coupled bursters. The simulation was conducted in the package XPPAUT [33] and the integration was done with Runge-Kutta integrators. As to the numerics the integration was done with a step size 0.01. All transients were removed by considering a long simulation. In the figure, it is clear that there is a spontaneous within-burst synchrony change in the fast dynamics of the system. The spikes in the burst from the two bursters are antiphase at the beginning but undergo a change to inphase (top panel of (a)). The activity patterns of action potentials, v_1 and v_2 , from two neurons are shown with distinguishing solid and dashed lines in the middle panel of (a), respectively. The corresponding time series of the slow variables, y_1 and y_2 , in the bottom panel of (a) show the bursts are fully synchronized. A random low amplitude noise of order 10^{-5} was added to the voltage variables of each neuron. (b) illustrates time series of d_{12} corresponding to the pattern shown in the top panel of Figure 7.7; here Euclidean metric d_{12} is defined as

$$d_{12} = \sqrt{(v_1 - v_2)^2 + (w_1 - w_2)^2 + (y_1 - y_2)^2}. \quad (7.12)$$

The spike synchrony patterns and change can easily be observed in this figure. The system parameters of the simulation are $g_{ca} = 4.4$, $g_k = 8$, $g_l = 2$, $v_k = -84$,

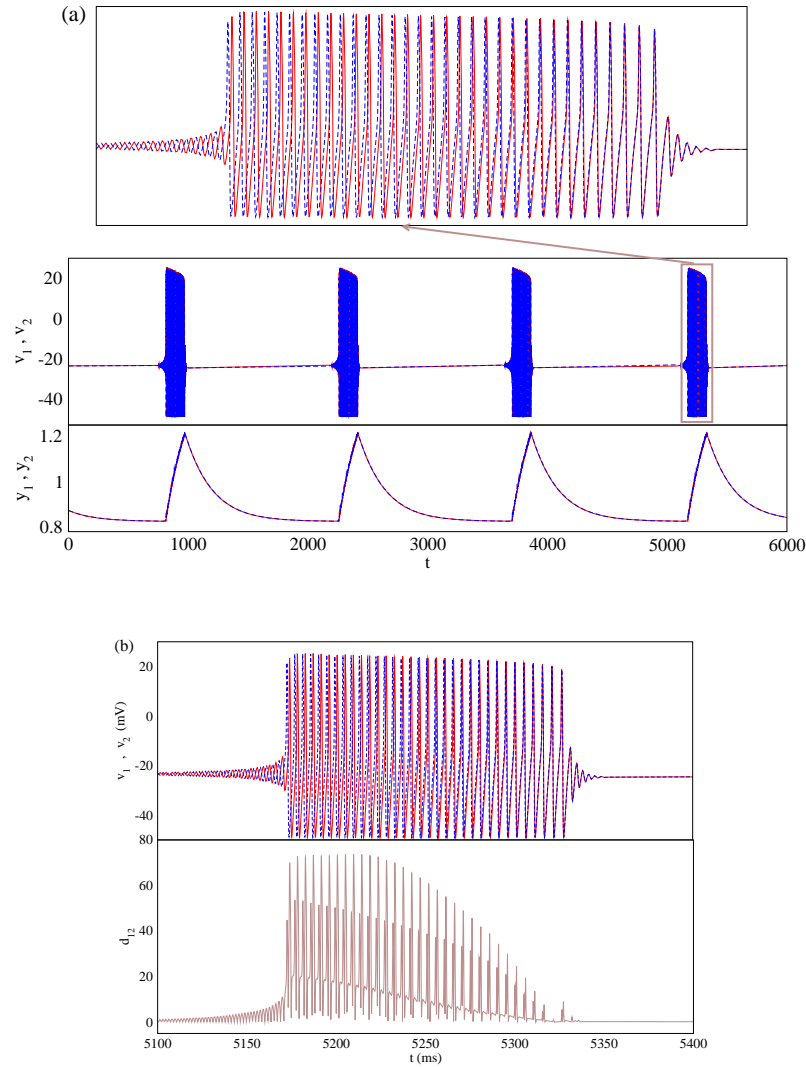


Figure 7.7: Within-burst synchrony changes in two coupled elliptic bursters governed by conductance-based system (7.10) and (7.11) for $n = 2$. In (a), the top panel shows a blown-up bursting activity patterns for two cells superimposed to show synchronization behaviour while the middle panel shows the section of superimposed bursting patterns generated by the two coupled bursters. The bottom panel shows time series of the corresponding slow variables. It is obvious that the bursters are burst synchronized while the spikes undergo within-burst synchrony changes – the spikes are antiphase at the beginning of the burst but change inphase towards the end. In (b), time series of d_{12} (7.12) corresponding to the synchronized burst shown in the top panel of (a) showing the synchrony change.

$v_l = -60$, $v_{ca} = 120$, $I = 120$, $g_{kca} = 0.75$, $\Phi = 1.2$, $\varepsilon = 0.002$ and $\mu = 0.016667$.

The coupling strength $\kappa = 0.01$ and the delay is $\tau = 1$.

7.4 Discussion

Our study confirms the presence of spontaneous within-burst synchrony changes induced by delay in both the reduced model of Bautin elliptic burster and the conductance-based Morris-Lecar elliptic bursting neuronal model with one additional slow variable. We observe a critical dependence of within-burst synchrony changes on the delay: within-burst synchrony changes were only observed for small delay, more precisely smaller than the interspike difference, longer delay causes disappearance of within-burst synchrony changes and eventually causes burst asynchronization. We did not observe within-burst synchrony changes for inhibitory coupling, i.e., when $\kappa < 0$. Also note in case of mutually delay-coupled conductance-based system (Figure 7.7) the antiphase and inphase patterns are more vivid in the subthreshold oscillation while the transition in the active phase appears to take place gradually over a number of oscillations indicating a bifurcation delay. We would like to add that in further simulation the conductance-based elliptic bursters we observed transients synchrony patterns demonstrating within-burst cascades of synchrony changes and more irregular spike synchrony behaviour with varying coupling strength. As relevant to this study we would like to refer [9] where the authors reported the observation of delay induced ‘phase flipping’ from zero (inphase) to π (antiphase) in the time-delay-coupled oscillators and they showed this ‘phase-flip’ bifurcation is accompanied by a discontinuous change in the frequency of the synchronized oscillator. In their study the authors studied an Andronov-Hopf normal form model for limit cycle oscillator.

We have not identified the bifurcations along the simulation summarized in Figure 7.7, this analysis is beyond the scope of investigation of the thesis. We have mentioned earlier the mutually delay-coupled systems have infinite-dimensional phase space which renders the analyses of the system very demanding, but a bifurcation analysis of the DDE systems as (7.5) and (7.10) may be done with the

suitable numerical package DDE-BIFTOOL [32]. We hope to pursue further investigation of the bifurcation of the fast subsystem of the mutually delay-coupled systems studied above in order to understand within-burst synchrony changes in such systems and their peculiarities.

To conclude the discussion we would like to note that the mutually-delayed coupling considered in the system (7.5) is equivalent to the complex coupling (e.g. system 3.6) studied earlier in the thesis. A periodic orbit for a complex system that is of the form

$$p(t) = r_0 e^{it\omega}, \quad (7.13)$$

the delay $p(t - \tau)$ and the complex multiple $p(t)e^{-i\tau\omega}$ are clearly equal. This means there is a qualitative similarity to coupling with a complex coefficient $(\kappa_1 + i\kappa_2)p(t)$ and to delay coupling with a real coefficient $Kp(t - \tau)$, namely if we take $Ke^{-i\tau\omega} = \cos \omega - i \sin \omega = \kappa_1 + i\kappa_2$. So, the delay coupling considered in this chapter is in fact equivalent to multiplication by a complex term. However, note that the phase shift depends on the period of the signal, so this argument may not hold for large variation of the delay and eventually the phase shift.

Chapter 8

Within-burst period doubling

In this chapter we briefly investigate within-burst synchrony changes in a mathematical model of an idealized nerve membrane model generating elliptic bursting which was formulated by FitzHugh and Rinzel in 1976 and studied extensively in [38, 90, 61, 53, 56, 61, 59, 89]. Here we study a pair of coupled FitzHugh-Rinzel (FHR) bursters and report appearance of spontaneous within-burst synchrony change which involves a period doubling bifurcation in contrast to bifurcations in observed in Chapters 3–7. In addition to numerical results we present a bifurcation analysis of the fast subsystem to explain this bifurcation.

8.1 FitzHugh-Rinzel elliptic burster model

The evolution of the FitzHugh-Rinzel (FHR) model is governed by the differential equations

$$\left. \begin{aligned} \dot{v} &= v - \frac{v^3}{3} - w + y + I, \\ \dot{w} &= \delta(a + v - bw), \\ \dot{y} &= \mu(c - v - dy). \end{aligned} \right\} \quad (8.1)$$

Here $v \in \mathbb{R}$ and $w \in \mathbb{R}$ constitute the fast subsystem and $y \in \mathbb{R}$ constitutes the slow subsystem. The system (8.1) has two-dimensional fast subsystem and one-dimensional slow subsystem. Here, I , a , b , c , d , δ , and μ are the parameters of the system. The bursting occurs for $\mu \ll 1$. Figure 8.1 shows the bursting activity of

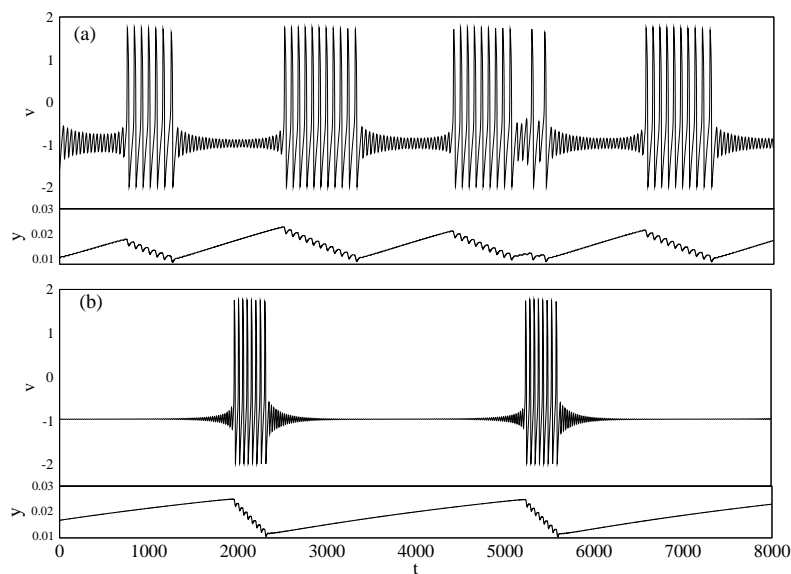


Figure 8.1: Bursting pattern generated by the FHR model (8.1). The parameters for the simulation are $I = 0.3125$, $a = 0.7$, $b = 0.8$, $d = 1$, $\delta = 0.08$, $\mu = 0.0001$, and in (a) $c = -0.775$ and (b) $c = -0.9$. The corresponding slow variable, y , is shown at the bottom of each panel.

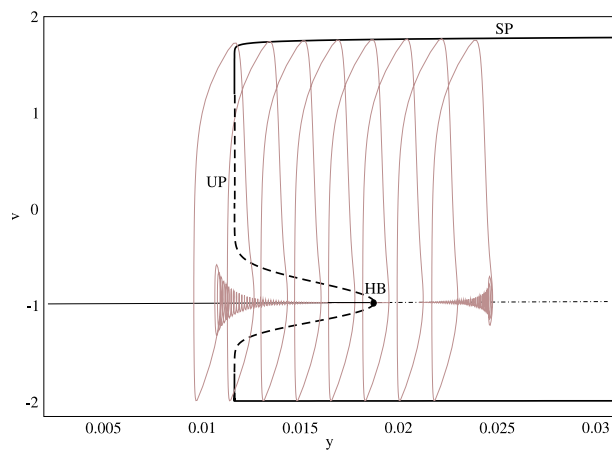


Figure 8.2: Bifurcation diagram of the FHR system (8.1). The periodic trajectory is superimposed to show the dynamics of the system as the slow variable, y , varies. The parameters are $I = 0.3125$, $a = 0.7$, $b = 0.8$, $c = -0.9$, $d = 1$, $\delta = 0.08$, and $\mu = 0.0001$.

the model (8.1) for $c = -0.775$ (a) and $c = -0.9$ (b); the other parameters in the simulation are $I = 0.3125$, $a = 0.7$, $b = 0.8$, $d = 1$, $\delta = 0.08$, and $\mu = 0.0001$. The panel (a) demonstrates one important feature of the FitzHugh-Rinzel burster is that the attraction to the unique equilibrium is relatively weak. So, the dynamics of the model yields apparent irregularity of bursting. Rinzel pointed out that this may be due to premature reentry into the active phase or even slow passage effect. Panel (b) demonstrates regular elliptic bursting patterns. In both simulations the elliptic bursting possess subthreshold oscillations in addition to large amplitude active phase. It has been pointed out in [82] that the elliptic bursting in FHR has subthreshold oscillations and large amplitude oscillations in active phase with two different frequencies, and their significance in information transfer is discussed.

Figure 8.2 is the bifurcation diagram revealing the main characteristics of elliptic bursting oscillations generated by (8.1). This figure depicts the two-dimensional projection of the corresponding attractor in the phase space together with a bifurcation diagram obtained according to the slow-fast decomposition method (Section 1.3). By virtue of the slow-fast decomposition method the fast changing variable v of the system is extracted using the slow changing variable y as a bifurcation parameter. The bifurcation analysis was carried out in XPPAUT [33]. It can be observed that the transition to repetitive spiking occurs via a subcritical Andronov-Hopf bifurcation (HB) and the transition to the quiescent state occurs via a fold limit cycle bifurcation; the characteristic bifurcation structure of elliptic bursting oscillations as discussed in Section 2.1. The stable and unstable steady state solutions of the system are shown with thin solid and dash-dotted line, respectively; the stable periodic (SP) and unstable periodic (UP) solutions are shown by bold solid and dashed line, respectively. In the following we present a coupled system of FHR bursters and explore the within-burst synchrony changes in a pair of such bursters.

8.2 Coupled FitzHugh-Rinzel System

We consider n -coupled FHR bursters as following

$$\left. \begin{aligned} \dot{v}_j &= v_j - \frac{v_j^3}{3} - w_j + y_j + I + \sum_{k \neq j} c_{jk}(\kappa_1 v_k + \kappa_2 w_k), \\ \dot{w}_j &= \delta(a + v_j - bw_j), \\ \dot{y}_j &= \mu(c - v_j - dy_j). \end{aligned} \right\} \quad (8.2)$$

Here $j, k = 1, 2, \dots, n$; c_{jk} is the connectivity matrix. In our study we consider $c_{jk} = 1$ and $c_{jj} = 0$; $\kappa_1, \kappa_2 \in \mathbb{R}$ are the coupling strengths. Note we consider a linear direct coupling in the voltage variable v_j of the fast subsystem which also involves coupling of the second fast variable to v_j . Burst and spike synchronization properties of coupled FHR bursters have been studied in [61], and in the following we use a pair of FHR bursters governed by the system (8.2) to explore within burst synchrony changes for a burst-synchronized constrained condition.

8.2.1 Within-burst bifurcation in two coupled FHR bursters

We study a pair of coupled FHR burster governed by the system (8.2) with $n = 2$. Figure 8.3 shows the simulation of such system. The simulation was carried out in XPPAUT with Runge-Kutta integrator. The parameters are The parameters are $I = 0.3125$, $a = 0.7$, $b = 0.8$, $c = -0.775$, $d = 1$, $\delta = 0.08$, $\kappa_1 = 0.001$, $\kappa_2 = 0.2$ and $\mu = 0.00002$. A low amplitude noise of order 10^{-7} is added to the components of the fast subsystem. This simulation clearly illustrates the presence of spontaneous within-burst synchrony changes in the coupled FHR system. This is further depicted in the time series of d_{12} where

$$d_{12} = \sqrt{(v_1 - v_2)^2 + (w_1 - w_2)^2 + (y_1 - y_2)^2}. \quad (8.3)$$

It can be observed that the spikes are inphase to begin with in the synchronized bursts generated by the system, but get asynchronized via a period doubling bifurcation, this is different from the bifurcation leading to spike synchrony changes observed in the previously studied systems in this thesis. This period doubling is

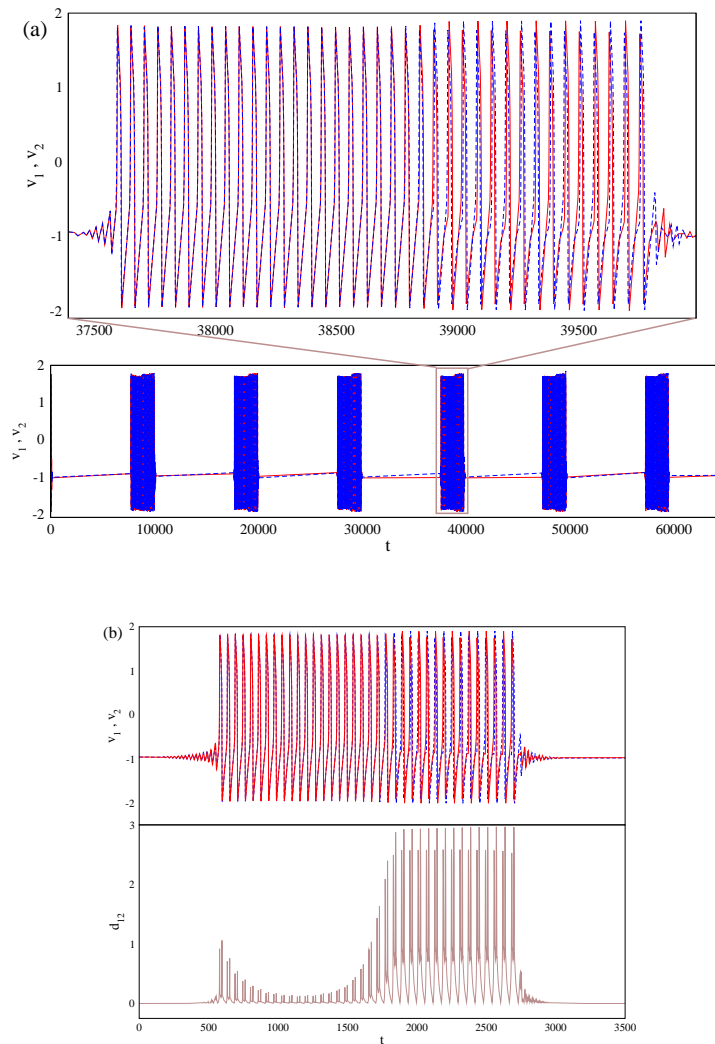


Figure 8.3: Within-burst synchrony change in a pair of FHR burster governed by (8.2) with $n = 2$. In (a), the bottom panel shows the bursting activity pattern from both FHR neurons and the top shows the details of the fast spiking within a single burst activity from both cells. The bursters generate synchronized bursts but the spikes are inphase at the beginning and then get asynchronized via a period doubling bifurcation. (b) shows the timeseries of d_{12} corresponding to the burst in the top panel of (a). The parameters are $I = 0.3125$, $a = 0.7$, $b = 0.8$, $c = -0.775$, $d = 1$, $\delta = 0.08$, $\kappa_1 = 0.001$, $\kappa_2 = 0.2$ and $\mu = 0.00002$. A low amplitude noise of order 10^{-7} is added to the components of the fast subsystem.

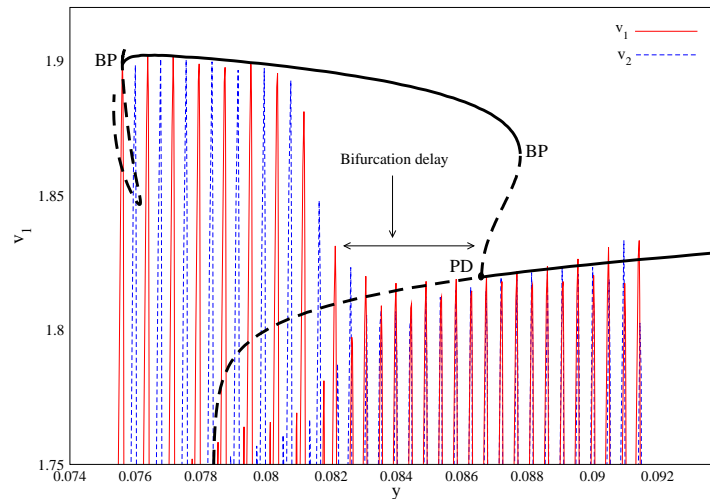


Figure 8.4: Bifurcation diagram of the fast subsystem obtained by continuation of periodic branch of v_1 for the burst-synchronized constraint $y_1 = y_2 = y$. The parameters are same the as in Figure 8.3. Here only the upper or maxima of the periodic branch is shown. The stable periodic solutions are shown by solid line while the unstable solutions are shown by dashed line. Note the diagram for periodic branch of v_2 will be same because of symmetry. The corresponding periodic trajectories of fast variables v_1 (thin solid line) and v_2 (thin dashed line) of the full system (8.2) are superimposed to show the spike synchrony change, with $y = \frac{y_1 + y_2}{2}$. Here the synchrony change occurs via a period doubling bifurcation (PD). Other bifurcation points are shown by BP. Note the bifurcation delay in the dynamics indicated by the arrow.

observed from the alternating spikes in the asynchronous part of the burst. Another interesting feature of this within-burst synchrony changes is the amplitude changes as occur after the within-burst bifurcation. It can be observed that the amplitude of the active phase of the burst gets a little larger following the period doubling bifurcation resulting in asynchronous spikes within the synchronized bursts.

8.2.2 Bifurcation analysis of the fast subsystem of two coupled FHR burster

A bifurcation analysis of the fast subsystem of (8.2) with $n = 2$ may be done by considering a burst-synchronized constrained model. By virtue of this reduction

approach we may consider $y_1 = y_2 = y$, so that the system is subject to one slow forcing. Considering μ as a singular perturbation parameter the fast dynamics can be investigated as discussed in Section 1.3. Figure 8.4 is obtained by following this method. This figure depicts a bifurcation diagram obtained by continuing the periodic branch of v_1 . The bifurcation analysis was carried out in XPPAUT. Here only the maxima of the period is shown along with the projection of corresponding periodic trajectory of both v_1 and v_2 obtained from the system (8.2) for $n = 2$ and considering $y = \frac{y_1 + y_2}{2}$. The parameters of this result are same as in Figure 8.3.

It is obvious that the periodic branch undergoes a period doubling bifurcation that results in the observed synchrony changes. The burst for the coupled system goes on for a range of y going from about 0.092 to 0.075 and inphase tonic spiking loses stability at about 0.0866 via a period doubling bifurcation, shown as PD. This diagram shows the amplitude variation as observed in the simulation in Figure 8.3. Note there are two other bifurcation points (BP) along the branches. One interesting feature observed is the delayed bifurcation in this system shown by arrow. The synchrony changes appear to take place later than the theoretical value. Note at the end of the burst we observe further bifurcation (left BP) and the dynamics gives way to more complicated scenario which is presumably due to the fast timescales in the systems.

This study confirms the existence of within-burst synchrony change brought forth by a different bifurcation mechanism in the case of coupled FHR elliptic bursters. Note that the observed period doubling bifurcation feature was not present in the more idealized Bautin elliptic burster studied in Chapters 3–7.

Chapter 9

Synchrony properties of the Hindmarsh-Rose neurons

In this chapter we study the burst synchrony properties of a mathematical bursting model known as Hindmarsh-Rose (HMR) model. In Chapter 3 we saw the rhythm generator of the leech heart interneuron can show interesting burst synchrony patterns where neurons from one side fire inphase burst while neurons from either side fire antiphase bursts; this generates rhythmic activity at about 0.1 Hz that paces leech heart neurons which in turn drives the heart beat. This pattern has been a subject of mathematical investigation by many authors recently, particularly we refer to [99] where a three-cell network of conductance-based model was studied to capture and understand such leech heart interneuron burst synchrony pattern. In this chapter we pursue a more mathematical interest in the rhythmicity involving burst synchronization generated by a network of three-HMR burster coupled with a cubic nonlinear coupling. The system demonstrates spontaneous cluster burst synchrony patterns where two cells fire inphase bursts while the third remains antiphase; we refer to this behaviour as ‘burst synchrony cluster’. We also observe switching between available cluster states depending on the input parameter of the system. We also demonstrate an example of emergence of more complex spontaneous burst synchrony cluster in network of high-dimensional HMR system.

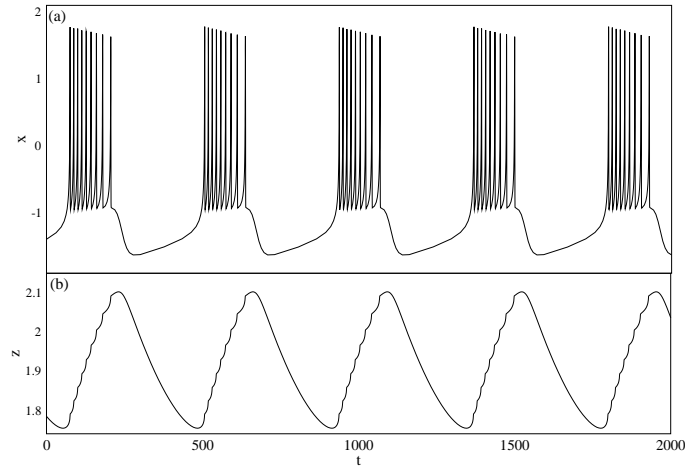


Figure 9.1: The bursting pattern generated by Hindmarsh-Rose system (9.1). The burst patterns are shown in (a) and the corresponding slow variable z is in (b). The parameters are $a = 1$, $b = 3$, $c = 1$, $d = 5$, $I = 2$, $x_0 = -1.6$, $r = 0.001$ and $s = 4$.

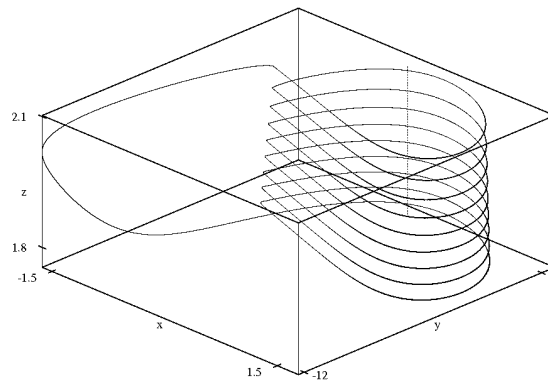


Figure 9.2: The 3D phase space structure of Hindmarsh-Rose system (9.1) in the bursting region. Details are as in Figure 9.1.

9.1 The Hindmarsh-Rose model

The Hindmarsh-Rose neuronal bursting model [50, 48, 49, 100] is given by differential equations:

$$\begin{aligned}
 \dot{x} &= y - ax^3 + bx^2 - z + I \\
 \dot{y} &= c - dx^2 - y \\
 \dot{z} &= r(s(x - x_0) - z)
 \end{aligned} \tag{9.1}$$

Here the notations for the state variables (x, y, z) and other parameters are used as in [50]. Evidently the Hindmarsh-Rose system (9.1) generates slow-fast oscillations; the first two equations govern spiking while the third equation with a slow time scale r accounts for the bursting and adaptation. The value of r is usually assumed very small ($r \ll 1$) in order to separate the fast xy -subsystem from the slow z -subsystem. The other parameters of the system are interpreted as following: I is the input current injected into the cell, the qualitative aspects of the system are governed by the parameter b , such as bursting or spiking can be induced by changing it. x_0 is the resting potential of the system and s tunes the adaptation of the system so that the small s (values around one) yields fast spiking behaviour. In case of bursting, decreasing time scale r can result in increasing number of spikes per burst. Figure 9.1 demonstrates the bursting pattern generated by the Hindmarsh-Rose system (9.1); panel (a) shows the square-wave bursting patterns and panel (b) shows the timeseries of the corresponding slow variable z . A 3-dimensional phase space realization for the Hindmarsh-Rose bursters is shown in Figure 9.2.

The small time scale parameter r allows the usual adiabatic approach to studying the fast subsystem with the slow variable as a parameter. Figure 9.3 is the bifurcation diagram of the system (9.1) obtained by applying slow-fast decomposition method (Section 1.3). The stable and unstable steady states are indicated by SSS (thin solid) and USS (dash-dotted) lines, respectively; SP indicates the stable periodic solutions: the upper branch is the maxima and the lower branch the minima of the solutions. The corresponding two-dimensional ‘hedgehog’ trajectory of the bursting solution is superimposed to show its position in the phase space and the solid arrows around it shows the direction of the evolution of the trajectory in the phase space. This bifurcation diagram is obtained with XPPAUT [33]. Note the onset of the burst occurs via a ‘fold’ bifurcation (indicated by ‘F’) and the offset of the burst occurs via a homoclinic (‘H’) bifurcation. One interesting feature is the existence of bifurcation delay in both onset and offset of the burst and they are indicated by broken arrows. Because of the homoclinic bifurcation at the offset

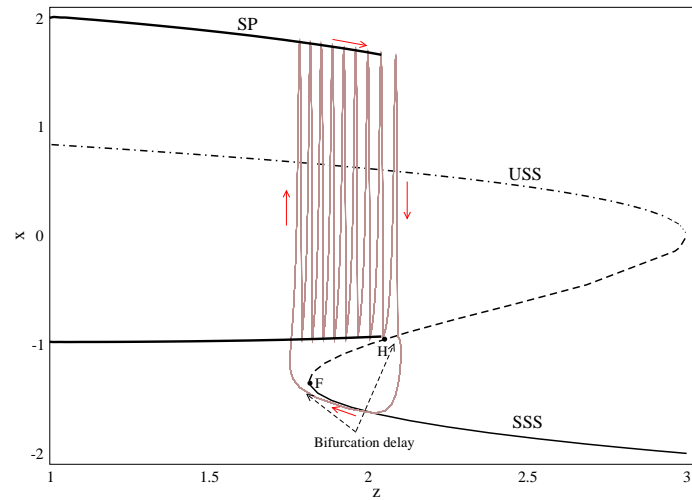


Figure 9.3: The bifurcation diagram of the Hindmarsh-Rose system (9.1). The bursting trajectory is superimposed on the bifurcation diagram to show the bursting solutions in the phase space. The stable steady state (SSS) solutions are shown with thin solid line while unstable steady state (USS) solutions are shown by dash-dotted line. SP indicates the stable periodic branch of the solution. The solid arrow shows the direction of the bursting trajectory in the phase space. Note the bifurcation delay at the onset and offset of the burst indicated by the broken arrows. F and H indicate the ‘fold’ and homoclinic bifurcations, respectively.

of the burst where the system changes from spiking to quiescent state, the period of the spikes at the end of the burst get infinite which is reflected in the increased interspike spacing in the spikes towards the end of the burst (see Figure 9.1(a)).

9.2 Coupling Hindmarsh-Rose bursters

The general form for n -Hindmarsh-Rose cell with voltage-dependent coupling may be written as

$$\begin{aligned}\dot{x}_j &= y_j - ax_j^3 + bx_j^2 - z_j + I + G_k(x_1, x_2, \dots, x_n) \\ \dot{y}_j &= c - dx_j^2 - y_j \\ \dot{z}_j &= r(s(x_j - x_0) - z_j)\end{aligned}\tag{9.2}$$

where $G_k(x_1, \dots, x_n)$ represents the dimensionless current flowing into the j th cell when all voltages are as specified. In neural systems it is reasonable to look at pairwise coupling only, where the current is a sum of the currents for each connection, in which case we have

$$\begin{aligned}\dot{x}_j &= y_j - ax_j^3 + bx_j^2 - z_j + I + \sum_{k=1}^n h(x_j, x_k) \\ \dot{y}_j &= c - dx_j^2 - y_j \\ \dot{z}_j &= r(s(x_j - x_0) - z_j).\end{aligned}\tag{9.3}$$

In this study we consider an arbitrary polynomial coupling function $h(x_j, x_k)$ difference of the action potential which is given as

$$h(x_j, x_k) = \sum_{p=1}^m c_{jk} \kappa_p (x_k - x_j)^p\tag{9.4}$$

with the coefficients κ_p representing the coupling strength of order p where $p = 1, \dots, m$; c_{jk} is the connectivity matrix. The coupling given by Equation (9.4) may be considered as an approximation of the nonlinear synaptic coupling and the lowest order with $p = 1$ reduces it to linear diffusive electric coupling. In this study we consider $c_{jk} = 1$ and $c_{jj} = 0$ implying all-to-all coupling and no self-coupling, respectively, and we truncate the coupling polynomial up to cubic

terms, i.e., $m = 3$; in this chapter we only study the system with cubic polynomial coupling function. Additionally as regards to the coupling strength we consider $\kappa_1 = \kappa_2 = \dots = \kappa$ for simplicity.

9.3 Burst synchrony clusters in 3-coupled HMR burster

In this section we present results of simulation of a coupled system consisting of mutually inhibitory three HMR neurons ($n = 3$) governed by the equations (9.3) and (9.4). All the coupling coefficients are same given by $\kappa_p = \kappa$ where $p = 1, \dots, m$. Figure 9.4 summarizes the simulation results for the study in the form of array diagrams. In the arrays the intensity of the voltage variables x_1 , x_2 and x_3 have been encoded in colour spectrum. The far right red part of the spectrum indicates the higher values for the voltage variables, consequently the red lines in the array imply the burst activity while the yellow part of the array implies the quiescent activity of the burst where the voltage variables have relatively lower values. The vertical line of the array shows the time with increasing downward and the three bursters shown along the horizontal line which should equally divide the horizontal line. These diagrams were obtained from the simulation of the coupled system in XPPAUT [33]. The diagrams were obtained from similar system but with different initial conditions. The parameters for both realizations are $a = 1$, $b = 3$, $c = 1$, $d = 5$, $x_0 = -1.6$, $r = 0.001$ and $s = 4$; for both the input parameter $I = 3.0$ and the coupling strength $\kappa = -0.001$. It can be observed that the bursters start of inphase and then separate into two burst synchrony clusters: (top) (2, 1) cluster state where the first two cells fire synchronous bursts while the third burst gets antiphase, (bottom) (1, 2) cluster state where the first cell fires antiphase bursts to the second and third cells and this is symmetric to the result shown in top. We observe from extensive simulation that this spontaneous burst synchrony cluster are harder to obtain in the system with linear coupling. Additionally, excitatory coupling or $\kappa > 0$ results in inphase bursts.

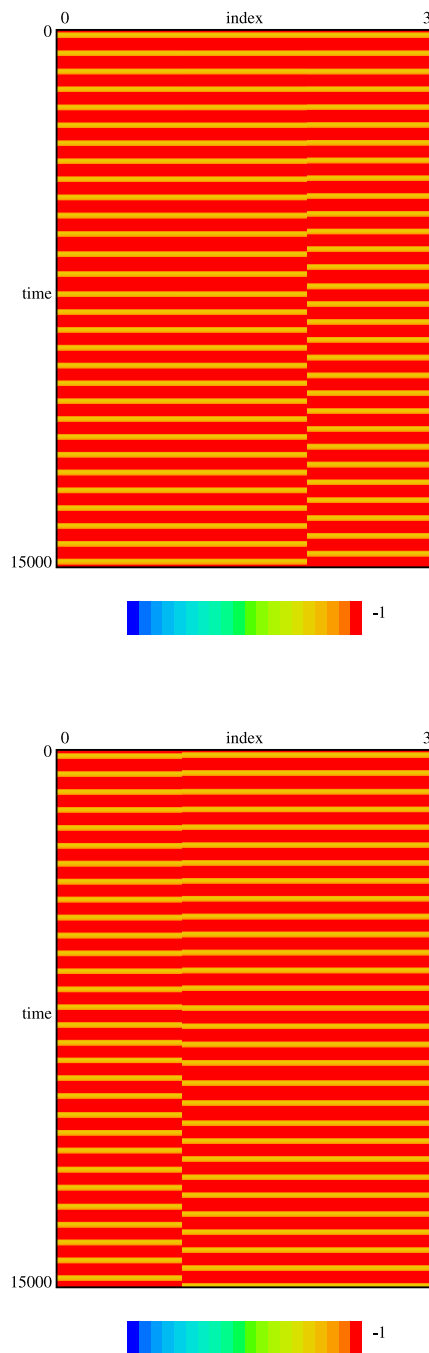


Figure 9.4: Array diagrams demonstrating (2,1) (top) and (1,2) (bottom) burst synchrony cluster states governed by the Hindmarsh-Rose system (9.3) and (9.4) for two different initial conditions with $m = 3$ and $n = 3$, $I = 3.0$ and $\kappa_p = \kappa = -0.001$ where $p = 1, \dots, m$. The initial conditions for three cells: (top) $(0.1, 0, 0)$, $(0.15, 0, 0)$, $(0.2, 0, 0)$ and (bottom) $(-0.1, 0, 0)$, $(0.15, 0, 0)$, $(0.2, 0, 0)$. See text for details.

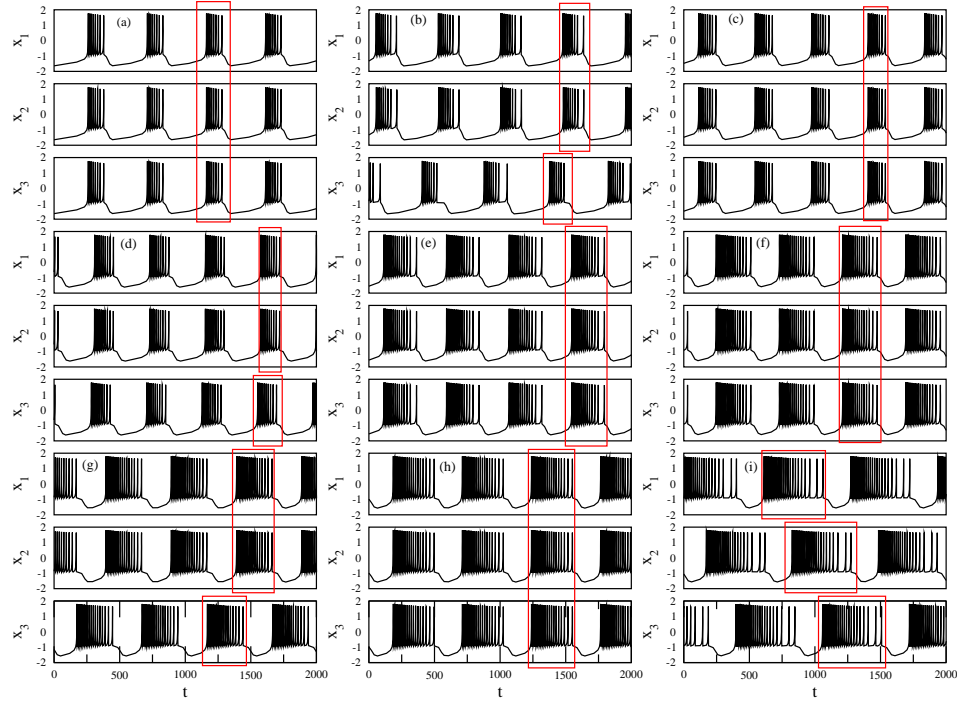


Figure 9.5: Changing of the burst synchrony cluster states with input for three-HMR neurons governed by the system (9.3) and (9.4) with $n = 3$. The initial conditions in all cases are $(0.1, 0, 0)$, $(0.15, 0, 0)$ and $(0.2, 0, 0)$. The input current I has been increased from (a)-(i), keeping the range of the input in the bursting regime: (a) $I = 1.8$, (b) $I = 1.9$, (c) $I = 2.0$, (d) $I = 2.2$, (e) $I = 2.7$, (f) $I = 2.9$, (g) $I = 3.0$, (h) $I = 3.1$, and (i) $I = 3.2$.

Figure 9.5 shows the changing of burst synchrony cluster states for three HMR neurons governed by the system (9.3) and (9.4) with $n = 3$ depending on input I . For all cases the initial conditions are same; the system parameters are same and they are as in Figure 9.1 for each cell and the coupling strength $\kappa = -0.001$. The input current has been increased from (a) to (i). The burst activity pattern from each cell is shown with the voltage variables x_1 , x_2 and x_3 . It is clear that the burst synchrony cluster changes as the input current is changed. The boxes enclose the bursts which are synchronized. In panel (a) the bursts from the cell are synchronized for $I = 1.8$ while the bursts arrange into a (2, 1) cluster for $I = 1.9$ shown in panel (b); in panel (i) we observe the bursts get desynchronized for $I = 3.2$ and evolve as rotating waves. One interesting feature is that the spike number in the bursts increases with input I .

One interesting features of the spontaneous burst synchrony clusters is that the spikes within the synchronized bursts are not necessarily inphase. Figure 9.6 shows the spike synchrony patterns for four different input for three-HMR burster system. The system and details are as in Figure 9.5. All the realizations have same initial conditions: $(0.1, 0, 0)$, $(0.15, 0, 0)$ and $(0.2, 0, 0)$. The system is subjected to different input currents from (a) to (d). In panel (a) the cells fire bursts and arrange in a (2, 1) burst synchrony cluster. But a rather careful observation shows that the spikes are not synchronized (see the boxes). The other panels show burst synchrony clusters with full synchronized spikes.

9.4 Example of burst cluster in larger network of Hindmarsh-Rose bursters and discussion

In this section we explore the burst synchrony cluster for larger system of coupled HMR burster. We consider mutually inhibitory coupled eight-HMR neurons governed by the system (9.3) and (9.4) with $n = 8$. Figure 9.7 shows the result of the simulation in array diagram. The red part of the spectrum implies the higher values of action potential or voltage variables, so the red strips represent the burst

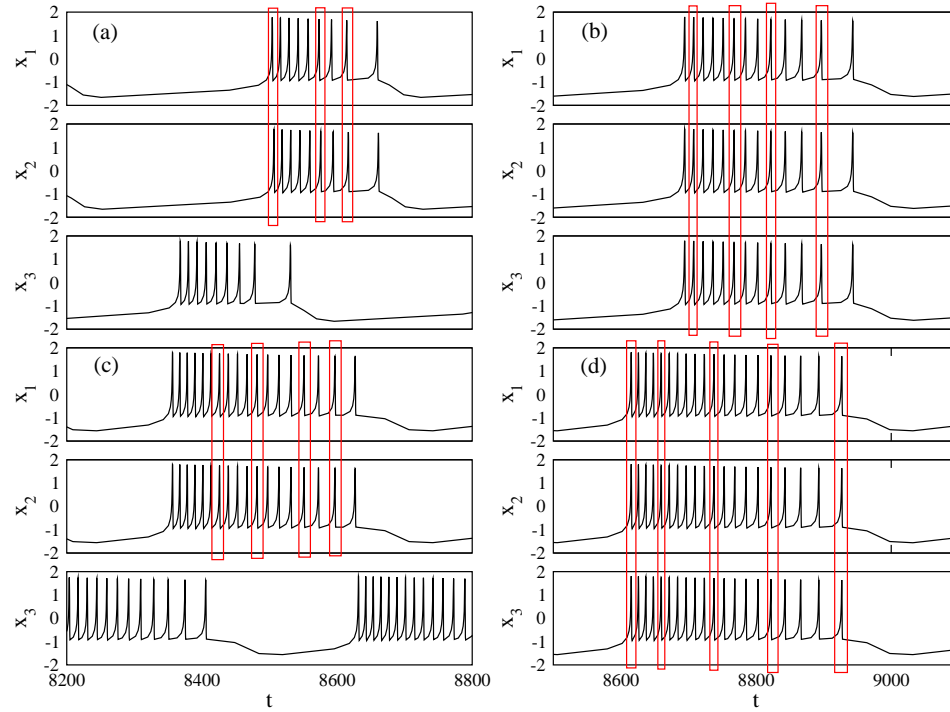


Figure 9.6: Spike synchrony properties in burst synchrony clusters of the three-coupled HMR system (9.3) and (9.4) with $n = 3$ with different input current I : (a) $I = 1.9$, (b) $I = 2.5$, (c) $I = 3.0$, (d) $I = 3.1$. The small boxes enclose spikes from synchronized bursts to signify spike synchrony patterns. Note in (a) the spikes are not exactly synchronized as in the other cases illustrated in (b), (c), and (d). (a) and (c) show (2, 1) burst synchrony cluster while full burst synchrony pattern can be seen in (b) and (d).

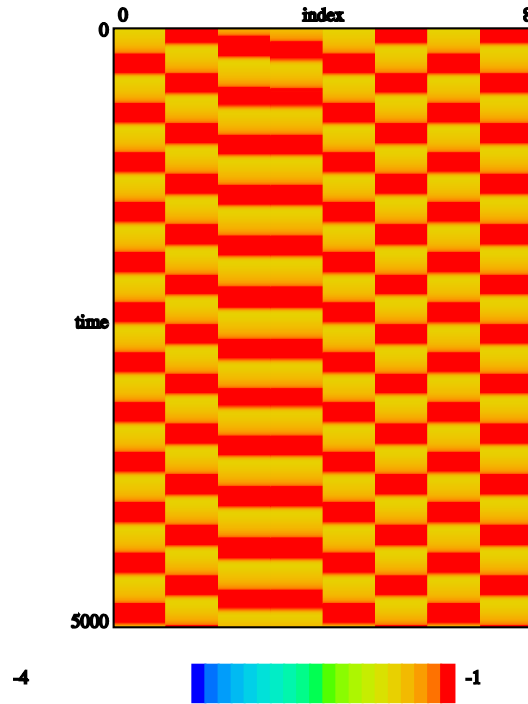


Figure 9.7: The array diagram showing spontaneous burst synchrony cluster in eight-HMR burster system. See text for details.

active phase while the yellow strips represent the quiescent phase. The horizontal axis of the array diagram represents time which increases downwards and the vertical axis is segmented in eight parts each representing a cell. The parameters of the simulation are $a = 1$, $b = 3$, $c = 1$, $d = 5$, $I = 3$, $x_0 = -1.6$, $r = 0.001$ and $s = 4$; the coupling coefficient $\kappa_p = \kappa = -0.001$ where $p = 1, \dots, 8$. In this case all transients have been removed by running the system for a long time. It is clear from the diagram that the system yields burst synchrony clusters similar to smaller system demonstrated in Figure 9.4. It is obvious that starting from left the first, fifth and seventh cells form one burst synchrony cluster, second, sixth and eighth cells form another burst synchrony cluster, while third and fourth cell form the third burst synchrony cluster.

This study confirms the burst synchrony cluster behaviour in the coupled Hindmarsh-Rose bursting neurons. This study was carried out over a small number of parameter values and we expect to see wide variety of other behaviour [99]. Note this burst synchrony cluster emerges in the system with mutually inhibitory coupling;

excitatory coupling results in inphase burst synchrony behaviour. Additionally, it is relatively easy to find burst synchrony clustering for the chosen nonlinear coupling scheme. Burst synchrony clusters are harder to achieve in systems with linear coupling. This spontaneous burst synchrony clustering in the network of HMR bursters suggests further investigations in the area of pattern generation in the biological systems will be of interest (such as leech heart interneurons [74, 80]).

Chapter 10

Conclusion

Finally we present a summary of the key results of the thesis, discuss some biological implications of the findings and present a potential outlook to future research.

10.1 Summary of thesis

We study the spike synchrony dynamics of coupled elliptic bursters and find that repeated within-burst synchrony changes are possible even for a simple normal form model, as long as terms that break isochronicity of the normal form are included. We observe that within-burst synchrony changes are stable and robust to changes in parameters. However, for identical bursters these within-burst changes are robust, and therefore easy to observe in the presence of noise. Moreover, figure 4.9 shows that increasing noise reduces the slow passage effect of both bifurcation points, i.e., the onset of bursting and the within-burst synchrony changes. We study a linear direct coupling scheme as well as demonstrating the presence of within-burst synchrony changes in an approximation of gap-junction and synaptic coupling

By reduction to fast-slow dynamics for the constrained burst-synchronized constrained model we analyze the appearance of the within-burst synchrony change for two oscillators, and the influence of various system parameters. In particular we find that a turning point in the instantaneous frequency Ω can be associated with the observed within-burst synchrony changes, analogous to bifurcations observed

in systems of coupled weakly dissipative oscillators [5]. Moreover, we can find the approximate location of the transition between stable inphase and antiphase oscillations from bifurcation analysis of a reduced system.

We extend our investigation to a system with three and four coupled Bautin bursters and find within-burst synchrony changes in these systems. Particularly, in the three-Bautin burster system the synchrony change occurs via a Andronov-Hopf bifurcation and in Figure 6.3 we present the solution trajectories. A rather more complicated synchrony change scenario is found in the numerical analysis for the four-Bautin burster system. We also observe within-burst cascade of synchrony changes attributed to multiple frequency transitions. A bifurcation analysis of such system reveals the similar bifurcation structure underlying the observed cascades of synchrony changes.

We explore numerically a mutually-delay coupled Bautin burster system with a constant delay and find spontaneous within-burst synchrony changes depending on the delay. We also explore an example of conductance-based Morris-Lecar bursting model with mutually delay coupling and find presence of within-burst synchrony changes.

Spontaneous within-burst synchrony change is also observed in coupled FitzHugh-Rinzel elliptic bursting model. We study a pair of FHR neurons with linear coupling. A numerical analysis shows the synchrony change occurs via a period doubling in contrast to other observed bifurcations in the within-burst synchrony changes reported earlier in the thesis. A path continuation of the period of a periodic orbit of a corresponding burst-synchronized constrained model demonstrates the period doubling leading to within-burst synchrony changes in this case.

Finally, we observe emergence of spontaneous burst synchrony clusters in the coupled Hindmarsh-Rose bursting system with cubic coupling. Simulation for the three-HMR burster system shows that the bursting neurons organize into separate burst synchrony clusters. We observe similar burst synchrony dynamics in the network of larger HMR bursting neurons. We study a variational system about the clustered solution for three-HMR system to approximate the largest Lyapunov

exponent of the synchrony states and this offers some qualitative insights into the stability of the burst synchrony cluster.

10.2 Biological implication

For larger populations of oscillators we expect there can be not just transitions between inphase and antiphase during bursts, but also spontaneous changes in clustering, leading to robust but sensitive phase dynamics [7, 88] and we believe this study gives some insight into the range of synchrony dynamics of coupled bursters in general. In particular, Section 4.2 shows that direct coupling is not necessary for within-burst synchrony changes. Better understanding of spike synchronization in more general coupled burster networks may lead to better understanding of potentially important new mechanisms for information processing and transmission by coupled neuronal bursters. This is discussed for example in [31, 54] where it is suggested that information transmission may occur via resonance between burst frequency and subthreshold oscillations.

Biologically, one functional significance of generating bursting as opposed to a single spike is that bursts are needed to increase the reliability of communication between neurons. It is understood that bursts with specific resonant interspike frequencies are more likely to cause a postsynaptic cell to fire [66]. This frequency preference between the interacting neurons in communication suggests that the same burst could resonate for some synapses or cells and not resonate for some others, depending on their natural resonance frequencies. In other words, the transmission of signals from pre to postsynaptic cell is most effective when the presynaptic cell fires a burst of action potentials with a specific resonant interspike frequency. By using bursts with different interspike frequencies, the presynaptic cell can selectively affect some postsynaptic targets, but not others. Such selective communication can be achieved on the time scale of tens of milliseconds without involving long term synaptic modification [31, 54]. The biological examples of selective communication between neurons based on the resonant frequency has been found in the recordings from rat somatosensory cortex [70]. It has been

shown in [75, 45] that a pair of neurons with similar resonant frequency, input from one burst elicits response in the other. Thus, changing the within burst or interspike frequency, a presynaptic cell can selectively affect some post synaptic cell but not others [31, 54].

Although bursts are usually considered as stereotypical spike train with constant frequency throughout the burst period, in reality the exact interspike frequency can vary within a burst. It depends on the presynaptic neuron and on the action of neuromodulators. In the conductance-based neuronal models, the instantaneous interspike frequency has been found generally to depend on the amplitude of oscillation [31, 54]. It is found in Hodgkin-Huxley model that greater the amplitude, the greater the interval between two successive maxima of oscillation, i.e., the interspike distance decreases. In such case, the optimal input to elicit response to such neuron is a burst of action potentials with adapting frequency or particularly a burst which accommodates decreasing frequency to resonate with the target neuron. Simulations of biological synaptic models in [75] have confirmed similar phenomenon: adapting rather than purely periodic bursts with constant spikes are optimal for neuronal communication. Given this effect about neuronal information transduction and communication between the bursting neurons in the biological system depending on the resonance between input and target frequencies, and also on the adaptive interspike frequency in the bursts, Bautin elliptic bursting model with non-isochronous behaviour reflect this scenario of adaptive interspike frequency. So, the burst synchronization and within-burst synchrony behaviour may be very significant in understanding the information contents and processing in the network of bursting neurons.

10.3 Future research

We extended our investigation of a pair of coupled Bautin elliptic bursters to three and four coupled Bautin elliptic bursters in Chapter 6 to explore within-burst synchrony changes, yet mathematical analysis to determine the bifurcation points was carried out only in case of the spike synchrony change from inphase to an-

tipphase in Section 6.2. We would like to analyze the case when the within-burst spike synchrony changes from antiphase to inphase as shown in Figure 6.2. Another interesting thing would be to look into is the withinburst synchrony changes via supercritical bifurcation unlike the cases (Figures 4.2, 5.4, 6.3, 8.4) where all observed changes with different models in this thesis are subcritical .

In our study we only focus on the elliptic bursting systems, but there are evidences that within-burst synchrony changes may well be present in other types of bursters (see for example Figure 3.6). Also the parabolic bursters presumably may show rich within-burst synchrony changes as the frequency of the fast spikes vary in these system (see Section 1.4). Moreover, the examples we studied in this thesis are all symmetric systems, and we would like to extend our investigation to asymmetric systems.

Although we found within-burst synchrony changes numerically in the mutually delay-coupled systems in Chapter 7, we could not carry out a bifurcation analysis because this would require tool like DDE-BIFTOOL [32] . In the near future we would like to employ this tool to carry out bifurcation analysis of this governing mutually-delay coupled DDE's. Moreover, we would like to explore more both numerically and analytically the phenomenon of spontaneous burst synchrony clusters in the example of Hindmarsh-Rose bursting neurons.

We would like to further explore the minimal model proposed by Izhikevich [55, 56] to look for within-burst synchrony change behaviour. The benefit in this model is its simplicity in implementation and analysis. The model is given as

$$\left. \begin{aligned} \dot{v} &= I + v^2 - u && \text{if } v \geq 1, \text{ then} \\ \dot{u} &= a(bv - u) && v \leftarrow c, u \leftarrow u + d \end{aligned} \right\} \quad (10.1)$$

This system has only four dimensionless parameters and depending on the values of a and b , it can be an integrator or a resonator burster [56]. This model is also suitable in large-scale networks neurons [57]. We hope finding within-burst synchrony change in this model will give way to more analytical treatment and applications in larger network system.

Bibliography

- [1] J. C. Alexander and D. Cai. On the dynamics of bursting systems. *J. Math. Bio.*, 29:405–823, 1991.
- [2] B. Amini, J. W. Clark Jr., and C. C. Canavier. Calcium dynamics underlying pacemaker-like and burst firing oscillations in midbrain dopaminergic neurons: A computational study. *The Journal of Neurophysiology*, 82(5):2249–2261, 1999.
- [3] V. I. Arnold. *Geometrical Methods in the Theory of Ordinary Differential Equations*. Dynamical Systems V. Bifurcation Theory and Catastrophe Theory. Grundlehren Math. Wiss., 250, Springer, 1983.
- [4] V. I. Arnold, V. S. Afrajmovich, Yu. S. Il'yashenko, and L. P. Shilnikov. *Bifurcation Theory*. Dynamical Systems V. Bifurcation Theory and Catastrophe Theory. Springer-Verlag, New York, 1994.
- [5] P. Ashwin and G. Dangelmayr. Reduced dynamics and symmetric solutions for globally coupled weakly dissipative oscillators. *Dyn. Syst.*, 20(3):333–367, 2005.
- [6] P. Ashwin, G. P. King, and J. W. Swift. Three identical oscillators with symmetric coupling. *nonlinearity*, 3:585–603, 1990.
- [7] Peter Ashwin and Jon Borresen. Encoding via conjugate symmetries of slow oscillations for globally coupled oscillators. *Phys. Rev. E (3)*, 70(2):026203, 8, 2004.

- [8] I. Atwater, C. M. Dawson, A. Scott, G. Eddlestone, and E. Rojas. The nature of the oscillatory behaviour in electrical activity for pancreatic beta-cell. *Horm. Metab. Res. Suppl.*, 10:100–107, 1980.
- [9] P. Awadhesh, K. Jrgen, D. S. Kumar, and R. Ramakrishna. Phase-flip bifurcation induced by time delay. *Physical review. E*, 74(3):035204(1–4), 2006.
- [10] P. Baldi and A. F. Atiya. How delay affect neural dynamics and learning. *IEEE Trans. Neural Networks*, 5(4):612–621, 1994.
- [11] R. Bertram, M. J. Butte, T. Kiemel, and A. Sherman. Topological and phenomenological classification of bursting oscillations. *Bull. Math. Biol.*, 57:413–439, 1995.
- [12] R. M. Borisyuk and A. B. Kirillov. Bifurcation analysis of a neural network model. *Biological Cybernetics*, 66:319–325, 1992.
- [13] T. G. Brown. The intrinsic factors in the act of progression in the mammal. *Proceedings of Royal Society London B*, 84:308–319, 1911.
- [14] N. Buric, I. Grozdanovic, and N. Vasovic. Type I vs type II excitable systems with delayed coupling. *Chaos Solitons Fractals*, 23:1221–1233, 2005.
- [15] N. Buric and D. Todorovic. Dynamics of fitzhugh-nagumo excitable systems with delayed coupling. *Phys. Rev. E*, 67(066222), 2003.
- [16] R. J. Butera, J. Rinzel, and J. C. Smith. Models of respiratory rhythm generation in the pre-botzinger complex.I. bursting pacemaker neurons. *Journal of Neurophysiology*, 82:382–397, 1999.
- [17] J. Blair. Stability in a model of a delayed neural network. *Journal of Dynamics and Differential Equations*, 5:607–623, 1993.
- [18] J. Blair, S.A. Campbell, and P. van den Driessche. Frustration, stability and delay-induced oscillations in a neural network model. *SIAM J. Appl. Math.*, 56:245–255, 1996.

- [19] S. A. Campbell, R. Edwards, and P. van den Driessche. Delayed coupling between two neural network loops. *SIAM J. Appl. Math.*, 65(1):316–335, 2004.
- [20] T. R. Chay. Effect of extracellular calcium on electrical bursting and intracellular and luminal calcium oscillations in insulin secreting pancreatic beta-cells. *Biophys. J.*, 73:1673–1688, 1997.
- [21] T. R. Chay and J. Keizer. Minimal model for membrane oscillations in the pancreatic beta-cell. *Biophys. J.*, 42:181–190, 1983.
- [22] B. W. Connors and M. J. Gutnick. Intrinsic firing patterns of diverse neocortical neurons. *Trends in Neuroscience*, 13:99–104, 1990.
- [23] S. Coombes and P. C. Bressloff. *Bursting: the genesis of rhythm in the nervous system*. World Scientific Publishing Co. Pte. Ltd., Hackensack, NJ, 2005.
- [24] G. de Vries. Multiple bifurcations in a polynomial model of bursting oscillations. *J. Nonlin. Sci.*, 8:281–316, 1998.
- [25] A. Destexhe, A. Babloyantz, and T. J. Sejnowski. Ionic mechanisms for intrinsic slow oscillations in thalamic relay neurons. *Biophys. J.*, 65:1538–1552, 1993.
- [26] A. Destexhe, D. Contreras, T. J. Sejnowski, and M. Steriade. A model of spindle rhythmicity in the isolated thalamic reticular nucleus. *Journal of Neurophysiology*, 72:803–818, 1994.
- [27] A. Destexhe, D. A. McCormick, and T. J. Sejnowski. A model for 8-10 hz spindling in interconnected thalamic relay and reticularis neurons. *Biophys. J.*, 65:2473–2477, 1993.
- [28] O. Diekmann, S. A. van Gils, S. M. V. Lunel, and H. O. Walther. *Delay Equations: Functional-, Complex-, and Nonlinear Analysis*, volume 110 of *Applied Mathematical Sciences*. Springer-Verlag, New York, 1995.

- [29] B. Doiron, C. Laing, A. Longtin, and L. Maler. Ghostbursting: A novel neuronal burst mechanism. *Journal of Computational Neuroscience*, 12:5–25, 2002.
- [30] Jonathan D. Drover and Bard Ermentrout. Nonlinear coupling near a degenerate Hopf (Bautin) bifurcation. *SIAM J. Appl. Math.*, 63(5):1627–1647 (electronic), 2003.
- [31] E. C. Walcott E. M. Izhikevich, N. S. Desai and F. C. Hoppensteadt. Bursts as a unit of neural information: selective communication via resonance. *Trends in Neuroscience*, 26:161–167, 2003.
- [32] K. Engelborghs, T. Luzyanina, and D. Roose. Numerical bifurcation analysis of delay differential equations using dde-biftool. *ACM Transactions on Mathematical Software*, 28(1):1–21, 2002.
- [33] Bard Ermentrout. *Simulating, Analyzing, and Animating Dynamical Systems: A Guide to XPPAUT for Researchers and Students*. SIAM, 2002.
- [34] G. B. Ermentrout and N. Kopell. Parabolic bursting in an excitable system coupled with a slow oscillation. *SIAM J. Appl. Math.*, 46(2):233–253, 1986.
- [35] G. B. Ermentrout and N. Kopell. Subcellular oscillations and bursting. *Math. Biosci.*, 78:265–291, 1996.
- [36] H. Erzgraber. *Dynamics of delay-coupled semiconductor laser systems*. Amsterdam: Vrije Universiteit. Vrije Universiteit, Amsterdam, 2006.
- [37] N. Fenichel. Persistence and smoothness of invariant manifolds for flows. *Indiana Univ. Math. J.*, 21:193–226, 1971.
- [38] R. FitzHugh. Impulses and physiological states in models of nerve membrane. *Biophysical Journal*, 1:445–466, 1961.
- [39] W. T. Frazier, E. R. Kandel, J. Kuppermann, R. Waziri, and R. E. Coggeshall. Morphological and functional properties of identified neurons in the

- abdominal ganglion of *aplysia californica*. *J. Neurophysiol.*, 30:1288–1351, 1967.
- [40] M. Golubitsky, K. Josic, and T. J. Kaper. *An Unfolding Theory Approach to Bursting in Fast-Slow Systems*. Global Analysis of Dynamical Systems. Taylor and Francis, 2001.
- [41] Martin Golubitsky, Krešimir Josić, and LieJune Shiau. Bursting in coupled cell systems. In *Bursting*, pages 201–221. World Sci. Publ., Hackensack, NJ, 2005.
- [42] J. Guckenheimer and P. Holmes. *Nonlinear Oscillations, Dynamical Systems, and Bifurcations of Vector Fields*, volume 42 of *Applied Mathematical Sciences*. Springer-Verlag, New York, 3rd edition, 1997.
- [43] S. Guo and L. Huang. Hopf bifurcating periodic orbits in a ring of neurons with delays. *Phy. D*, 183:19–44, 2003.
- [44] S. Guo and L. Huang. Nonlinear waves in a ring of neurons with delay. *IMA J. Appl. Math.*, 71:496–518, 2006.
- [45] A. Gupta, Y Wang, and H Markram. Organizing principles for a diversity of gabaergic interneurons and synapses in the neocortex. *Science.*, 287:273–278, 2000.
- [46] J. K. Hale and S. M. Verduyn Lunel. *Introduction to Functional Differential Equations*, volume 99 of *Applied Mathematical Sciences*. Springer-Verlag, New York, 1993.
- [47] H. G. Heinzel. Gastric mill activity in the lobster. I. spontaneous modes of chewing. *Journal of Neurophysiology*, 59(2):528–550, 1988.
- [48] J. L. Hindmarsh and R. M. Rose. A model of the nerve impulse using two first-order differential equations. *Nature*, 296:162–164, 1982.

- [49] J. L. Hindmarsh and R. M. Rose. A model of neuronal bursting using three coupled first-order differential equations. *Proc. Roy. Soc. Lon.*, B 221:87–102, 1984.
- [50] Jim Hindmarsh and Philip Cornelius. The development of the Hindmarsh-Rose model for bursting. In *Bursting*, pages 3–18. World Sci. Publ., Hackensack, NJ, 2005.
- [51] Frank C. Hoppensteadt and Eugene M. Izhikevich. *Weakly connected neural networks*, volume 126 of *Applied Mathematical Sciences*. Springer-Verlag, New York, 1997.
- [52] E. M. Izhikevich. Phase equations for relaxation oscillators. *SIAM Journal on Applied Mathematics*, 60(5):1789–1804, 2000.
- [53] E. M. Izhikevich. Subcritical elliptic bursting of bautin type. *SIAM Journal on Applied Mathematics*, 60(2):503–535, 2000.
- [54] E. M. Izhikevich. Resonance and selective communication via bursts in neurons having subthreshold oscillations. *BioSystems*, 67:95–102, 2002.
- [55] E. M. Izhikevich. Simple model for spiking neurons. *IEEE Transactions on Neural Networks*, 14:1569–1572, 2003.
- [56] E. M. Izhikevich. *Dynamical Systems in Neuroscience: The Geometry of Excitability and Bursting*. MIT Press, Cambridge, Massachusetts, 2007.
- [57] E. M. Izhikevich and G. M. Edelman. Large-scale model of mammalian thalamocortical systems. *PNAS*, 105:3593–3598, 2008.
- [58] E. M. Izhikevich and F. Hoppensteadt. Classification of bursting mappings. *International Journal of Bifurcation and Chaos*, 14(11):3847–3854, 2004.
- [59] Eugene M. Izhikevich. Neural excitability, spiking and bursting. *Internat. J. Bifur. Chaos Appl. Sci. Engrg.*, 10(6):1171–1266, 2000.

- [60] Eugene M. Izhikevich. Neural excitability, spiking and bursting. *Internat. J. Bifur. Chaos Appl. Sci. Engrg.*, 10(6):1171–1266, 2000.
- [61] Eugene M. Izhikevich. Synchronization of elliptic bursters. *SIAM Rev.*, 43(2):315–344 (electronic), 2001. Revised reprint of “Subcritical elliptic bursting of Bautin type” [SIAM J. Appl. Math. **60** (2000), no. 2, 503–535; MR1740257 (2000m:92004)].
- [62] H. S. Jezzini, A. A. V. Hill, P. Kuzyk, and R. L. Calabrese. Detailed model of intersegmental coordination in the timing network of the leech heartbeat central pattern generator. *J. Neurophysiol*, 91:958–977, 2004.
- [63] D. Junge and C. L. Stevens. Cyclic variation of potassium conductance in the burst generating neurone in aplysia. *J. Physiol.*, 235:155–181, 1973.
- [64] S. W. Kuffler and J. G. Nicholls. *From Neuron to Brain*. Sinauer Associates, Inc., Sunderland, Massachusetts, 1976.
- [65] Yuri A. Kuznetsov. *Elements of applied bifurcation theory*, volume 112 of *Applied Mathematical Sciences*. Springer-Verlag, New York, third edition, 2004.
- [66] John Lisman. Bursts as a unit of neural information: making unreliable synapses reliable. *Trends in Neuroscience*, 20:38–43, 1997.
- [67] E. Marder and D. Bucher. Central pattern generators and the control of rhythmic movements. *Current Biology*, 11:986–996, 2001.
- [68] E. Marder and R. L. Calabrese. Principles of rhythmic motor pattern production. *Physiological Reviews*, 76:687–717, 1996.
- [69] H. Markram, M. Toledo-Rodriguez, Y. Wang, A Gupta, G. Silberberg, and C. Wu. Interneurons of the neocortical inhibitory system. *Nature Review Neuroscience*, 5:793–807, 2004.

- [70] H. Markram, Y Wang, and M Tsodyks. Differential signaling via the same axon of neocortical pyramidal neurons. *Proc. Natl. Acad. Sci. U.S.A.*, 95:5323–5328, 1998.
- [71] P. A. Mathieu and F. A. Roberge. Characteristics of pacemaker oscillations in aplysia neurons. *Can. J. Physiol. Pharmacol.*, 49:787–795, 1971.
- [72] D. A. McCormick and H. C. Pape. Properties of a hyperpolarization-activated cation current and its role in rhythmic oscillation in thalamic relay neurons. *Journal of Physiology*, 431:291–318, 1990.
- [73] C. Morris and H. Lecar. Voltage oscillations in the barnacle giant muscle fiber. *Biophysical Journal*, 35:193–213, 1981.
- [74] F. Nadim, O. H. Olsen, E. DeSchutter, and R. L. Calabrese. Modeling the leech heartbeat elemental oscillator: I. interactions of intrinsic and synaptic currents. *J. Computational Neuroscience*, 2:215–235, 1995.
- [75] T. Natschlger and W. Maass. Computing the optimally fitted spike train for a synapse. *Neural Computation*, 13:2477–2494, 2001.
- [76] C.A. Del Negro, Chie-Fang Hsiao, S.H. Chandler, and A. Garfinkel. Evidence for a novel mechanism in rodent trigeminal neurons. *BioPhysical Journal*, 75:174–182, 1998.
- [77] A. I. Neishtadt. Prolongation of the loss of stability in the case of dynamic bifurcations. I. *Differential Equations*, 23(12):1385–1390, 1987.
- [78] A. I. Neishtadt. Prolongation of the loss of stability in the case of dynamic bifurcations. II. *Differential Equations*, 24(2):171–176, 1988.
- [79] L. G. Nowak, R. Azouz, M. V. Sanchez-Vives, C. M. Gray, and D. A. McCormick. Electrophysiological classes of cat primary visual cortical neurons in vivo as revealed by quantitative analyses. *Journal of Neurophysiology*, 89:1541–1566, 2003.

- [80] O. H. Olsen, F. Nadim, and R. L. Calabrese. Modeling the leech heartbeat elemental oscillator: II. exploring the parameter space. *J. Computational Neuroscience*, 2:237–257, 1995.
- [81] C. M. Pedroarena, I. E. Pose, J. Yamuy, M. H. Chase, and F. R. Morales. Oscillatory membrane potential activity in the soma of a primary afferent neuron. *Neurophysiology*, 82:1465–1476, 1999.
- [82] M. Perc and M. Marhl. Amplification of information transfer in excitable systems that reside in a steady state near a bifurcation point to complex oscillatory behavior. *Phys Rev E*, 71:026229(1–7), 2005.
- [83] M. Pernarowski. Fast subsystem bifurcations in a slowly varied lienard system exhibiting bursting. *SIAM Journal on Applied Mathematics*, 54:814–832, 1994.
- [84] R. E. Plant. The effects of calcium⁺⁺ on bursting neurons. *Biophys. J.*, 21:217–237, 1978.
- [85] R. E. Plant. Bifurcation and resonance in a model for bursting nerve cells. *J. Math. Biol.*, 11:15–32, 1981.
- [86] R. E. Plant and M. Kim. On the mechanism underlying bursting in the aplysia abdominal ganglion r15. *cell. Math. Biosci.*, 26:357–375, 1975.
- [87] R. E. Plant and M. Kim. Mathematical description of a bursting pacemaker neuron by a modification of the hodgkin-huxley equations. *Biophys. J.*, 16:227–244, 1976.
- [88] M. I. Rabinovich, P. Varona, A. I. Selverston, and H. D. I. Abarbanel. Dynamical principles in neuroscience. *Reviews of Modern Physics*, 78(4):1213–1265, 2006.
- [89] J. Rinzel. *Ordinary and Partial Differential Equations*. Lecture Notes in Mathematics. Springer, Berlin, 1985.

- [90] J. Rinzel. A formal classification of bursting mechanisms in excitable systems. In *Mathematical topics in population biology, morphogenesis and neurosciences (Kyoto, 1985)*, volume 71 of *Lecture Notes in Biomath.*, pages 267–281. Springer, Berlin, 1987.
- [91] J. Rinzel and G. B. Ermentrout. *Analysis of neural excitability and oscillations*. Methods in Neuronal Modelling: From Ions to Networks. The MIT Press, Cambridge, MA, second edition, 1998.
- [92] John Rinzel and Young Seek Lee. Dissection of a model for neuronal parabolic bursting. *Journal of Mathematical Biology*, 25:653–675, 1987.
- [93] J. E. Rubin and D. Terman. Geometric singular perturbation analysis of neuronal dynamics. *Handbook of Dynamical Systems, FNorth-Holland*, pages 93–146, 2000.
- [94] M. E. Rush and J. Rinzel. Analysis of bursting in a thalamic neuron model. *Biol. Cybern.*, 71:281–291, 1994.
- [95] J Rinzel S. M. Baer, T. Erneux. The slow passage through a Hopf bifurcation: delay, memory effects and resonance. *SIAM J. Appl. Math.*, 49:55–71, 1989.
- [96] Jürgen Schwarz, Gerhard Dangelmayr, Andreas Stevens, and Kurt Bräuer. Burst and spike synchronization of coupled neural oscillators. *Dyn. Syst.*, 16(2):125–156, 2001.
- [97] L. P. Shayer and S. A. Campbell. Stability, bifurcation and multistability in a system of two coupled neurons with multiple time delays. *SIAM J. Appl. Math.*, 61(2):673–700, 2000.
- [98] Arthur Sherman. Anti-phase, asymmetric and aperiodic oscillations in excitable cells-I. coupled bursters. *Bulletin of Mathematical Biology*, 56(5):811–835, 1994.

- [99] A. L. Shilnikov, R. Gordon, and I.V. Belykh. Polyrhythmic synchronization in bursting network motifs. *J. Chaos*, pages 18, 037120, DOI: 10.1063/1.2959850, 2008.
- [100] A. L. Shilnikov and M. L. Kolomiets. Methods of the qualitative theory for the hindmarsh-rose model: a case study. tutorial. *J. Bifurcations and Chaos*, 18 (8):1–27, 2008.
- [101] M. A. Shishkova. Investigation of a system of differential equations with a small parameter in highest derivatives. *English transl. Sov. Math., Dokl.*, 14:483–487, 1973.
- [102] F. K. Skinner, N. Kopell, and E. Marder. Mechanisms for oscillation and frequency control in reciprocal inhibitory model neural networks. *Journal of Computational Neuroscience*, 1:69–87, 1994.
- [103] Donald R. Smith. *Singular-perturbation theory : An introduction with applications*, volume 12 of *Interdisciplinary Applied Mathematics*. Cambridge University Press, United States of America, first edition, 1985.
- [104] P. Smolen, D. Terman, and J. Rinzel. Properties of a bursting model with two slow inhibitory variables. *SIAM J. Appl. Math.*, 53:861–892, 1993.
- [105] D. Somers and N. Kopel. Rapid synchronization through fast threshold modulation. *Biol. Cybern.*, 68:393–407, 1993.
- [106] D. Somers and N. Kopel. Waves and synchrony in networks of oscillators or relaxation and non-relaxation type. *Physica D*, 89:169–183, 1995.
- [107] C. Soto-Trevino, N. Kopell, and D. Watson. Parabolic bursting revisited. *J. Math. Biol.*, 35:114–128, 1996.
- [108] I. M. Stanford, R. D. Traub, and J. G. R. Jefferys. Limbic gamma rhythms. II. synaptic and intrinsic mechanisms underlying spike doublets in oscillating subicular neurons. *The Journal of Neurophysiology*, 80(1):162–171, 1998.

- [109] P. G. S. Stein, S. Grillner, A. I. Selverston, and D. G. Stuart. *Neurons, Networks, and Behaviour*. Cambridge, MA: MIT Press, 1997.
- [110] G. Stépán. *Retarded Dynamical Systems: Stability and Characteristic Functions*, volume 210. Pitman Research Notes in Mathematics. Longman, Essex, England, 1989.
- [111] M. Steriade. *Neuronal Substrates of Sleep and Epilepsy*. Cambridge University press, Cambridge, 2003.
- [112] F. Strumwasser. The cellular basis of behavior in aplysia. *J. Psychiatr. Res.*, 8:237–257, 1971.
- [113] H. Su, G. Alroy, ED. Kirson, and Y. Yaari. Extracellular calcium modulates persistent sodium current-dependent burst-firing in hippocampal pyramidal neurons. *Journal of Neuroscience*, 21:4173–4183, 2001.
- [114] J. Su. Persistent unstable periodic motions, I. *J. Math. Anal. Appl.*, 198:796–825, 1996.
- [115] J. Su. Persistent unstable periodic motions, II. *J. Math. Anal. Appl.*, 199:88–119, 1996.
- [116] Jianzhong Su, Jonathan Rubin, and David Terman. Effects of noise on elliptic bursters. *Nonlinearity*, 17(1):133–157, 2004.
- [117] I. Timofeev, F. Grenier, M. Bazhenov, T. J. Sejnowski, and M. Steriade. Origin of slow cortical oscillations in deafferented cortical slabs. *Cerebral Cortex*, 10:1185–1199, 2000.
- [118] R. D. Traub, R. K. Wong, R. Miles, and H. Michelson. A model of a ca3 hippocampal pyramidal neuron incorporating voltage-clamp data on intrinsic conductances. *Journal of Neurophysiology*, 66(2):635–650, 1991.
- [119] X. J. Wang. Genesis of bursting oscillations in the hindmarsh-rose model and homoclinicity to a chaotic saddle. *Physica D*, 62:263–274, 1993.

- [120] X. J. Wang. Ionic basis for intrinsic 40 hz neuronal oscillations. *NeuroReport*, 5:221–224, 1993.
- [121] X. J. Wang. Fast burst firing and short-term synaptic plasticity: a model of neocortical chattering neurons. *Neuroscience*, 89:347–362, 1999.
- [122] X. J. Wang and J. Rinzel. Alternating and synchronous rhythms in reciprocally inhibitory model neurons. *Neural Computation*, 4:84–97, 1992.
- [123] M. D. Womack and K. Khodakhah. Active contribution of dendrites to the tonic and trimodal patterns of activity in cerebellar purkinje neurons. *Journal of Neuroscience*, 22(24):10603–10621, 2002.
- [124] H. Y. Wu and S. M. Baer. Analysis of an excitable dendritic spine with an activity-dependent stem conductance. *J. Math. Biol.*, 36:569–592, 1998.
- [125] J. Wu, T. Faria, and Y. S. Huang. Synchronization and stable phase-locking in a network of neurons with memory. *Math. Comput. Modelling*, 30(1-2):117–138, 1999.
- [126] Y. Yuan and S. A. Campbell. Stability and synchronization of a ring of identical cells with delay coupling. *J. Dynam. Differential Equations*, 16(1):709–744, 2004.